

# Energy Minimization and Thermal Fluctuation in Artificial Magnetic Penrose Ice



Dong Shi

School of Physics and Astronomy

University of Leeds

A thesis submitted for the degree of

*Doctor of Philosophy*

February 2016

---

---

The candidate confirms that the work submitted is his own, except where work which has formed part of jointly-authored publications has been included. The contribution of the candidate and the other authors to this work has been explicitly indicated below. The candidate confirms that appropriate credit has been given within the thesis where reference has been made to the work of others.

This copy has been supplied on the understanding that it is copyright material and that no quotation from the thesis may be published without proper acknowledgement.

The right of Dong Shi to be identified as Author of this work has been asserted by him in accordance with the Copyright, Designs and Patents Act 2016.

©2015 The University of Leeds and Dong Shi

## Acknowledgements

Firstly, I would give my thanks to my supervisor, Prof. Christopher Marrows, who gave me this opportunity to study in Leeds and also for his support and encouragement throughout four years. Big thanks are also given to Dr. Gavin Burnell, who provided numerous great ideas. I also thank my previous supervisor Prof. Peter Olmsted for his useful discussion and support on the theory part of my work. Thanks also to all the other academic in this group, Dr. Oscar Céspedes, Prof. Bryan Hickey and Dr. Thomas Moore. Their humour and knowledge make this group fantastic. Besides, I would like thank those who have given me assistance on the lab work, especially to Dr. Mannan Ali and Dr. Simon Connell. Thanks to Dr. Aaron Stein for making the samples. I am also grateful to Dr. Robin Richardson and Dr. Thana Sutthibutpong who showed me how to use python code with great patience.

Thanks to Dr. Jason Morgan, who tutored me with great patience about various apparatus but also had to endure my poor Chinese English accent. I'm grateful to Dr Rowan Temple, who not only spend a lot of time on physics discussion, but also organized numerous entertainment events. Thanks to everyone in the condensed matter group to make me spend the most happy four years of my life. I also want to thanks my friends in Leeds who organised all sort of sports event which keep me fit and had lots of fun.

Finally, I will give thanks to my wonderful family for their support and encouragement, particularly for my father who introduced physics to me and also for my mother and brother. I haven't spent Chinese New Year with them for four years, I owe a big apology to them.



## Abstract

This thesis addresses the behaviour of the artificial magnetic Penrose tiling pattern in three different states: the as-fabricated state, the ac demagnetised state and the thermally annealed state. The artificial magnetic Penrose tiling comprises magnetic nano-elements, which are termed “islands”, forming a Penrose tiling patterned from a 2-D film. The main focus is the energy minimisation effect of these three protocols and the effect of frustration on the thermal fluctuation processes. The experimental investigations were conducted via magnetic force microscopy.

A well-defined ground state for the Penrose pattern was theoretically predicted based on consideration of the nearest neighbour dipolar interaction. In this predicted ground state, a twofold degenerate rigid framework that spans the system is interspersed with islands for which the moment direction is not defined, since both directions are energetically degenerate. The experimental samples were then characterised in terms of the population of the rhombuses which are the basic units of the Penrose tiling. The predicted long-range order in the system-spanning framework was not found from any states in the experiments.

Further to this, a correlation function was defined for this pattern and evaluated for the three different states. The correlation length extracted from the correlation function indicates that the thermally annealed state has longer range order than other two states, and this conclusion is corroborated by the domain size measurement from colour mapping of domains (the configuration of arrays are mapped by different colours depending on whether the configuration is the as or different to the ground state). The moments of the nano-elements are

found to be only locally correlated in the thermally annealed samples, which was believed to be due to the blocking temperature distribution emerging during the thermal annealing process. However, this hypothesis failed to explain an anomaly in the vertex energy distributions from the thermally annealed samples. One certain type of vertex was found to be stuck in a high energy state rather than the lowest energy state after the thermal annealing. Based on the blocking temperature estimation and magneto-static energy calculation, the energy distribution of each vertex at the blocking temperature was found to follow the Boltzmann distribution multiplied by a degeneracy factor. This result agrees with the vertex energy distribution extracted from the experiments at room temperature. This agreement shows that the energy minimization of the Penrose tiling is restricted by the ratio of vertex energy and the blocking temperature, giving a guide for future investigations.

# Contents

<b>1</b>	<b>Introduction</b>	<b>1</b>
1.1	Frustration . . . . .	1
1.2	Outline of the thesis . . . . .	4
<b>2</b>	<b>Literature review</b>	<b>6</b>
2.1	Spin ice . . . . .	6
2.1.1	Introduction . . . . .	6
2.1.2	Magnetic monopole . . . . .	9
2.2	Artificial spin ice . . . . .	12
2.2.1	Introduction . . . . .	12
2.2.2	Square pattern and kagome pattern . . . . .	14
2.2.3	Accessing the ground state . . . . .	17
2.2.4	Thermal behaviour in artificial spin ice . . . . .	26
2.3	Penrose pattern . . . . .	30
2.3.1	Introduction to the quasi-periodic pattern . . . . .	30
2.3.2	How to generate a Penrose pattern . . . . .	32
2.3.3	Study on quasicrystal materials . . . . .	33
2.4	Summary . . . . .	35
<b>3</b>	<b>Methods</b>	<b>37</b>
3.1	Electron Beam Lithography . . . . .	37
3.2	AFM/MFM . . . . .	38
3.2.1	MFM . . . . .	41
3.3	Interpretation of microscopy data . . . . .	42
3.3.1	Interpretation of AFM/MFM image . . . . .	42

3.3.2	Dipolar energy calculation and net magnetisation calculation	44
3.3.3	Net magnetisation calculation . . . . .	46
3.3.4	Order parameter calculation . . . . .	46
3.4	The AC demagnetisation and thermal annealing detail . . . . .	48
3.4.1	The detail of AC demagnetisation . . . . .	48
3.4.2	The detail of thermal annealing . . . . .	48
<b>4</b>	<b>Ground state of the Penrose tiling</b>	<b>50</b>
4.1	Introduction . . . . .	50
4.2	Ground state of the Penrose tiling . . . . .	52
4.2.1	Vertex energy configuration . . . . .	52
4.2.2	Ground state of two decagons . . . . .	54
4.2.3	The ground state of the whole pattern and its character . .	56
<b>5</b>	<b>Statistical results of rhombus, and colour maps</b>	<b>62</b>
5.1	Introduction . . . . .	62
5.2	Different Rhombus configuration distribution . . . . .	63
5.2.1	Different types of rhombus configurations and correspond- ing populations in each state . . . . .	63
5.2.2	Colour mapped MFM images analysis . . . . .	65
5.2.3	Conclusion . . . . .	68
<b>6</b>	<b>Domain size estimate</b>	<b>70</b>
6.1	Introduction . . . . .	70
6.2	Skeleton-part correlation function . . . . .	71
6.3	Domain in Penrose tiling pattern . . . . .	74
6.4	Summary . . . . .	77
<b>7</b>	<b>Thermal fluctuation studies of Penrose tilings</b>	<b>78</b>
7.1	Introduction . . . . .	78
7.2	Temperature driven dynamics of Penrose tiling . . . . .	80
7.2.1	The energy distribution of each vertex in different states .	81
7.3	Summary . . . . .	93

<b>8 Summary and future work</b>	<b>94</b>
8.1 Summary . . . . .	94
8.2 Future work . . . . .	96
<b>A How to generate 2-D Penrose tiling</b>	<b>97</b>
A.1 1-D quasiperiodic pattern . . . . .	98
A.2 Penrose tiling . . . . .	98
<b>B All possible vertex configurations and their corresponding energies</b>	<b>102</b>
B.1 Appendix B . . . . .	102
<b>C Some selected AFM, MFM and SEM images</b>	<b>107</b>
C.1 Appendix C . . . . .	107
<b>References</b>	<b>126</b>

## Abbreviations

AFM	Atomic Force Microscopy
EBL	Electron Beam Lithography
GS	Ground state
L-TEM	Lorenz Transmission Electron Microscopy
MFM	Magnetic Force Microscopy
PEEM	Photoemission Electron Microscopy
XMCD	X-ray Magnetic Circular Dichroism
SQUID	Superconducting Quantum Interference Device
FMR	Ferromagnetic Resonance
RPM	Rotation Per Minute
STM	Scanning Tunnelling Microscopy
SEM	Scanning Electron Microscopy
$E$	Energy
$k_B$	Boltzmann's constant
$k_B T$	Thermal energy
$\mu_0$	Free space magnetic permeability
$\mu_B$	Bohr magneton
Py	Permalloy
$R$	Molar constant

# List of Figures

1.1 Frustration in triangle motif. . . . .	2
1.2 Ground state of magnets from site disorder to frustration. . . . .	3
2.1 Pyrochlore structure and ice rule. . . . .	7
2.2 Specific heat measurement data for $\text{Dy}_2\text{Ti}_2\text{O}_7$ . . . . .	9
2.3 Experimental neutron diffraction data and numerical simulation for a spin ice material. . . . .	10
2.4 Dumbbell model mapping from dipole and monopole interaction .	11
2.5 The AFM and MFM image of square pattern. . . . .	12
2.6 The TEM image of kagome pattern. . . . .	14
2.7 The ground state of square pattern of artificial spin ice. . . . .	16
2.8 kagome artificial spin ice . . . . .	17
2.9 Three demagnetize protocol . . . . .	18
2.10 Field step-size dependent of residual moment . . . . .	19
2.11 Control of short-range magnetic correlation via field step size and lattice constant. . . . .	20
2.12 Step size dependence of total magnetostatic energy for three dif- ferent island pairs. . . . .	22
2.13 The specific vertex energy of demagnetised lattice compared to calculated type II vertex energy and purely random tiling energy	24
2.14 The effective temperature of square array . . . . .	25
2.15 Thermal fluctuation in square pattern and correspond defect fre- quency . . . . .	27
2.16 Remanent magnetization of artificial spin ice as a function of tem- perature . . . . .	28

## LIST OF FIGURES

---

2.17	The thermally annealed square pattern and kagome pattern in charge ordered map . . . . .	29
2.18	Penrose tiling and matching rule . . . . .	32
2.19	Monte Carlo simulation and experiment model on the Penrose tiling	34
2.20	SEM image of wire networked Penrose tiling . . . . .	36
3.1	EBL process . . . . .	39
3.2	The principle of AFM . . . . .	40
3.3	AFM, MFM, SEM and digital image of Penrose tiling pattern. . .	43
3.4	Island shape in Penrose tiling sample . . . . .	44
3.5	The seven different type of vertex in Penrose tiling are shown here	45
3.6	All possible configurations and corresponding energies for type I vertex . . . . .	46
4.1	The charge ordered state of the kagome pattern . . . . .	51
4.2	Low energy configuration of seven types vertex in Penrose tiling pattern . . . . .	53
4.3	Decagon construction of Penrose tiling . . . . .	55
4.4	Type A decagon ground state construction process. . . . .	58
4.5	Type B decagon GS construction . . . . .	59
4.6	Two decagons meet together . . . . .	60
4.7	Ground state of whole pattern . . . . .	61
5.1	The population of rhombus moments configurations in different states . . . . .	64
5.2	Coloured magnetic configuration . . . . .	65
5.3	A MFM image of a sample in a state prepared by thermal annealing	66
5.4	Coloured MFM image from the sample after thermal annealing. .	67
6.1	Magnitude of correlation as a function of lattice spacing for annealed square artificial spin ice . . . . .	72
6.2	Correlation between different states and the ground state . . . . .	73
6.3	Colour mapping of two magnetic configurations . . . . .	75
6.4	The average domain size from samples in different states as a function of lattice spacing . . . . .	76



## LIST OF FIGURES

---

7.1	Vertex energy level occupations I . . . . .	82
7.2	Vertex energy level occupations II . . . . .	83
7.3	The difference between the lowest and second lowest vertex energy configuration populations for seven vertices when samples are in the thermally annealed state . . . . .	84
7.4	Type VII vertex configuration transit . . . . .	86
7.5	Magnetisation data for a permalloy film on $\text{Si}_3\text{N}_4$ . . . . .	88
7.6	The inter-island interaction barrier estimation in type VII vertex . . . . .	89
7.7	Blocking temperature equation solution and energy population of type VII vertex . . . . .	91
7.8	The energy population distribution of type I and type III vertex . . . . .	92
A.1	2-D projection method . . . . .	99
A.2	Icosahedral space . . . . .	100
A.3	Tiling generated by different value of $\gamma$ . . . . .	101
B.1	All possible configurations, and corresponding energies, of a type I vertex. . . . .	102
B.2	All possible configurations, and corresponding energies, of a type II vertex. . . . .	103
B.3	All possible configurations, and corresponding energies, of a type III vertex. . . . .	103
B.4	All possible configurations, and corresponding energies, of a type IV vertex. . . . .	104
B.5	All possible configurations, and corresponding energies, of a type V vertex. . . . .	104
B.6	All possible configurations, and corresponding energies, of a type VI vertex. . . . .	105
B.7	All possible configurations, and corresponding energies, of a type VII vertex. . . . .	106
C.1	The AFM image of pattern when the sample was in the as grown state. . . . .	108

## LIST OF FIGURES

---

C.2	The MFM image of the pattern when the sample was in the as grown state. . . . .	109
C.3	The AFM image of the pattern when the sample was in the ac demagnetised state. . . . .	110
C.4	The MFM image of the pattern when the sample was in the ac demagnetised state. . . . .	111
C.5	The AFM image of the pattern when the sample has been thermally annealed. . . . .	112
C.6	The MFM image of the pattern when the sample has been thermally annealed. . . . .	113
C.7	The SEM image of a pattern when the sample was in the as grown state. . . . .	114

# List of Tables

3.1	MESP - Magnetic Etched Silicon Probe - Specifications . . . . .	41
3.2	The number of possible configuration and energy level for each type of vertex in the Penrose tiling. . . . .	45

# Chapter 1

## Introduction

### 1.1 Frustration

Sometimes, frustration can make life interesting, especially for physicists. The study of frustration is an interesting and important aspect in physics. Frustration is the inability to simultaneously satisfy competing interactions in a system. This leads to the failure to have a unique ground state, and instead there are many degenerate low energy states. We can then say that the system shows frustration. Different forms of frustration have been realised when people studied different materials. For example, a spin glass as a random and magnetic system has been studied for decades. It is believed that the frustration accounted for most features of this type of material. A well studied spin glass material is the alloy CuMn, in which the Mn ion is randomly diluted in the non-magnetic Cu [1]. The indirect exchange interaction between the magnetic moments of the Mn ions is mediated via the conduction electrons in Cu. The interaction is of the RKKY type, which means that the sign of interaction oscillates depending on the distance between Mn ions, i.e. the interaction can be ferromagnetic or antiferromagnetic. This means that it takes random values and signs for the randomly distributed moments. The net result is that such a system does not possess a well defined ground state, but instead a large number of possible ground states. It also leads to a “cooperative freezing transition”. This is not a phase transition which would lead the system into a magnetic ordered state, as no long-range order is found [2].

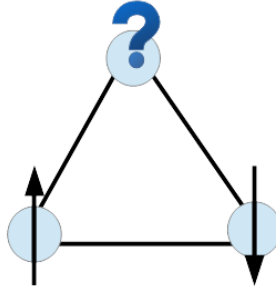


Figure 1.1: Frustration in an antiferromagnetic triangle motif: all the spins prefer to be antiparallel in this system. When the direction of two of the spins are fixed, the remaining spin is in a dilemma, where it cannot satisfy both the interactions with its neighbouring spins, i.e. frustration is present.

Conversely, in some materials, frustration arises because of geometrical constraints. An often-used example is an antiferromagnetic motif with an odd number of spins in a loop, the simplest example of which is a triangle. As shown in figure 1.1, the Ising spins prefer to be antiparallel to their neighbours. If two spins are placed antiparallel, the remaining one cannot satisfy both of the interactions with its neighbouring spins at the same time. In this case, the system is said to have geometrical frustration. As a result, there are six energy-degenerate ground states for this system. These multiple ground states enhance fluctuation, while suppressing the order of the system. It also leads to finite ground state entropy. A example of this geometrical frustration in a 3-D material is spin ice, e.g.  $\text{Ho}_2\text{Ti}_2\text{O}_7$  and  $\text{Dy}_2\text{Ti}_2\text{O}_7$ . These systems have a pyrochlore structure, which is a network of corner sharing tetrahedra in which the rare earth ions Ho or Dy sit in the corners [3; 4; 5]. Due to strong crystal fields, the moments of these ions are confined to point along a certain axis. Therefore the spins are Ising doublets, and can only point inwards or outwards from the tetrahedra. The dominant interaction is the dipolar interaction between these large magnetic moments. It is long range, but it can be understood using an effective nearest neighbour ferromagnetic exchange interaction model [6]. This ferromagnetic interaction is frustrated by the crystal geometry and leads to the ground state of the spins in a tetrahedron following the so called “two-in two-out” rule, which means that two of the spins point in-

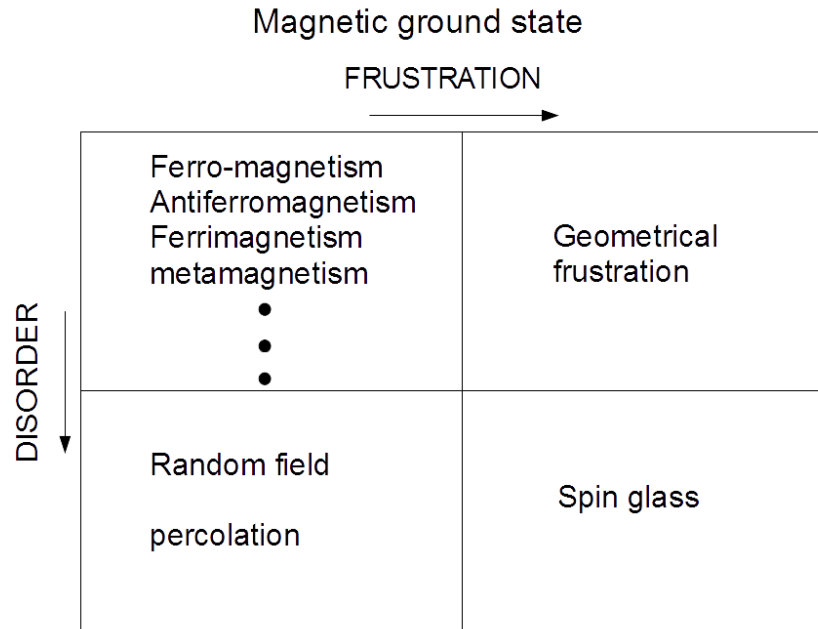


Figure 1.2: Ground state of magnets from site disorder to frustration. The chart is after A.P. Ramirez [7].

wards and two point outwards. The ground state of a single tetrahedron is highly degenerate and has six equal configurations. Owing to frustration, there is no ordering transition at any temperature. More details on spin ice will be given in Chapter 2.

Based on the knowledge of frustration and disorder, magnetic materials can be coarsely classified (see figure 1.2). However, there are other systems whose structure is neither ordered nor disordered, but shows a kind of quasi-order. One such structure is the Penrose tiling, which lacks periodicity but still possesses long range order [8]. The corresponding material is the quasicrystal. When this type of material was found to possess magnetic properties, people expected that some exotic magnetic long range order may exist. The magnetic quasicrystal compounds, therefore, attracted intensive interest [8; 9; 10]. However, after decades of study, only short range magnetic order has been found in rare earth based quasicrystals [11; 12; 13]. The spin order in magnetic quasicrystals remains elusive.

In recent years, a prominent programme has been developed in which the physics of geometrical frustration is explored via a model system known as artificial spin ice [14; 15; 16; 17]. Such systems consist of nano-fabricated magnetic elements. Each element is designed to be an elongated island. Due to the shape anisotropy, each element has Ising-like moment, which prefers to point along the elongated direction. The advantage of this system is that it not only allows flexibility in the design of the desired arrays, but also it is possible to be probed at room temperature via nano-scale imaging tools. An example of such work is the 2-D artificial square pattern, in which a frustrated interaction is designed analogous to those found in 3-D spin ice [14].

So far, large portions of this work focussed on special patterns, which were designed to investigate the analogous physics to bulk spin ice. Following short-range correlation, artificial magnetic charge propagation was found, similar to the bulk spin ice material [14; 15; 16; 18; 19]. These results give credence to the idea of exploring the frustration in the magnetic quasi-periodic system using similarly constructed artificial analogues. Based on this idea, in this project a 2-D artificial Penrose tiling pattern was designed and several energy minimisation protocols were conducted. The thermal annealing has been confirmed as the most effective protocol, which significantly minimises the total energy of arrays. It has been shown that further energy minimisation is possible from the investigation of thermal fluctuations.

## 1.2 Outline of the thesis

The aim of this thesis is to present the main efforts on energy minimisation. A well-defined ground state of a Penrose tiling and the construction process will be presented. Several statistical analyses were conducted on different states and the results are addressed. Furthermore, the energy distribution of different types of vertex in the thermally annealed state is displayed and the distributions are found follow the Boltzmann law. The results are confirmed by numerical simulation.

Chapter 2 will give a brief overview of spin ice and artificial spin ice, as well as quasicrystal materials. The experimental protocols implemented on the square and kagome patterns in the literature will be described in more detail. Chapter

3 will illustrate the methods and techniques used in this thesis to fabricate and characterise the samples. A correlation function will also be introduced in this chapter.

A well defined ground state of Penrose tiling will be illustrated in Chapter 4. Each procedure of the ground state construction process will be demonstrated.

In Chapter 5, some statistical results in terms of experimental rhombuses population will be shown. Apart from these results, a colour map method that help to visualise the magnetic order of sample is also introduced. A correlation function is introduced in Chapter 6 which is different from the one used on other patterns. The corresponding results will be listed as well.

In Chapter 7, the energy distribution of each type vertex will be listed. The blocking temperature estimation will be given, based on which the numerical simulation of energy distribution will be shown.

In Chapter 8, an overview of the results and a discussion of future work and further interesting directions will be given.



# Chapter 2

## Literature review

### 2.1 Spin ice

#### 2.1.1 Introduction

Water ice is an interesting condensed matter system. It has been found to have residual entropy at zero temperature [20], which seemingly violates the third law of thermodynamics. In 1935, Pauling pointed out that this non-zero entropy originated from the configurational proton disorder. Based on this theory, the residual entropy of water ice was estimated as 0.81 Cal/deg.mol [21], which is very close to the experimental value of  $0.82 \pm 0.05$  Cal/deg.mol [20].

It is known that the oxygen and hydrogen ions in water ice obey the so-called “ice-rule” [22], which requires that two of the protons are close to and two protons are further away from each oxygen ion in order to minimize the energy (see figure 2.1(a)). The whole ice system can be described as a lattice of corner-sharing tetrahedra, in which each oxygen ion sits at the center of each tetrahedron and interacts with other oxygen ions via protons that are close to the four vertices of the tetrahedron (see figure 2.1(b)). Pauling showed that due to the “ice rule”, the protons do not build long-range order, but rather generate a multiply-degenerate ground state. In other words, the system has residual entropy.

As each tetrahedron provides six-fold degeneracy, when following the “ice rule”, the number of degeneracies diverge exponentially with the size of the system. According to Pauling’s calculations, this degeneracy gives water the residual

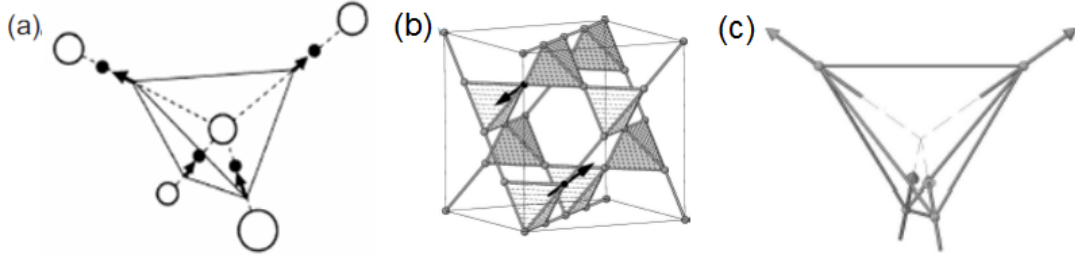


Figure 2.1: (a) Water ice: the white spheres are oxygen ions and the black dots are hydrogen ions. (b) The pyrochlore lattice (c) Spin ice: the macroscopic ground state is two spins pointing inwards and two spins pointing outwards. (a) after Bramwell et al. [3], (b) and (c) after Fenell et al. [23].

entropy per mole  $S = \left(\frac{R}{2}\right) \ln 3/2 = 0.81$  Cal/deg.mol, which is in agreement with the experiment [24].

In 1956 [25], Anderson investigated an antiferromagnetic pyrochlore Ising model, which showed that the system possessed similar structure to water ice by replacing the  $H^+$  ion vectors with spins. Therefore, the magnetic ordering in this system has similar problems to water ice ordering due to the geometrical frustration and is characterized by residual entropy. In 1997 [3], this type of magnetic structure was experimentally discovered in the rare earth compound  $\text{Ho}_2\text{Ti}_2\text{O}_7$ . The cation  $\text{Ho}^{3+}$  sits on the pyrochlore lattice of corner-sharing tetrahedra. A strongly anisotropic crystallographic environment forces the magnetic moments to point along the  $\langle 111 \rangle$  axes.

The Curie-Weiss temperature deduced from high temperature susceptibility measurements is 1.9 K. It shows that the coupling between  $\text{Ho}^+$  ions should be  $\sim 1$  K. However, other experiments found no evidence of a magnetic transition when the temperature was lowered as far down as a few mK [3]. Similar behaviour has been observed in another rare earth compound,  $\text{Dy}_2\text{Ti}_2\text{O}_7$ . The susceptibility curve does not show a sharp cusp as expected from spin glass material at low temperature [26]. Besides, the material for the experiment was identified as having few structural defects [27]. All the evidence points to the fact that this spin disorder is not caused by either a spin glass state or structural defects, but represents a new kind of frozen spin state.

Harris [3] proposed a simple model of nearest neighbour ferromagnetic interactions. It shows that in a system with a cubic pyrochlore lattice, the ferromagnetic exchange coupling is highly frustrated by the lattice geometry, while the antiferromagnetic exchange coupling is not. The development of ferromagnetic order is, therefore, frustrated. The system obeys similar “ice rules” when constructing low energy states as those for water ice. Therefore, the system possesses residual entropy, like water ice.

This scenario was strongly supported by a remarkable experiment [28]. In the work of Ramirez et al., the residual entropy of  $\text{Dy}_2\text{Ti}_2\text{O}_7$  at low temperature, as deduced from specific heat data, is in agreement with Pauling’s estimation for water ice.

It was suggested, however, that the nearest neighbour exchange interaction is antiferromagnetic rather than ferromagnetic [29], which should result in a phase transition at low temperature. This is, however, difficult to reconcile with the specific heat measurement. As shown in figure 2.2 the specific heat measurement indicated that no phase transition occurs in  $\text{Dy}_2\text{Ti}_2\text{O}_7$  across a wide range of temperatures. When the temperature is above  $T_{\text{peak}} \sim 1.24$  K, the system is in the paramagnetic regime and is weakly correlated. Single tetrahedra do not obey the “ice rules”. As the temperature approaches  $T_{\text{peak}}$ , the ice rule is progressively fulfilled. The Schottky anomaly-like peak arises in the specific heat curve. However, this Schottky anomaly is not a sharp peak or cusp, as might be associated with a phase transition. This controversy was solved later by the development of another model, which takes the dipolar interaction into account. This model is called the “dipolar ice model” [4].

Normally, the dipolar interaction is treated as a perturbation because its magnitude is too small when compared with the exchange interaction, but the rare earth ions in spin ice materials have large magnetic moments, and consequently the magnetic dipolar-dipolar interaction is expected at least to be of the same order as the exchange interaction. This hypothesis was confirmed by neutron diffraction data and Monte-Carlo simulation based on the “dipolar ice model” [4] (see figure 2.3). The spin ice is better described by the dipolar spin ice model, which incorporates both the long-range dipolar interaction and weak antiferromagnetic nearest neighbour exchange interactions. The ground states for both

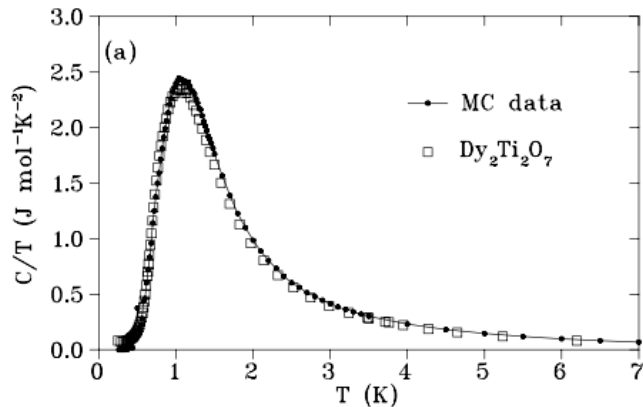


Figure 2.2: Specific heat measurement data for  $\text{Dy}_2\text{Ti}_2\text{O}_7$ : There is a smooth broad maximum for the specific heat curve, which is known as a Schottky anomaly. This does not indicate that a phase transition occurs. After Ramirez et al. [28]

models are approximately equivalent when the temperature is close to zero [30]. Due to the large energy barrier between the ground and the first excited state (around 100 K), as well as the slow relaxation time, the ground state is still far from being accessed experimentally.

### 2.1.2 Magnetic monopole

Based on the “dipolar spin ice” model, one of most exciting developments so far has been the prediction of magnetic monopoles [6]. The magnetic monopole arises because violations of the “ice rule” can occur. A simple defect consists of a tetrahedron with three spins pointing in and one spin pointing out or vice versa due to a single flip spin. The centre of the tetrahedron forms a source or sink for flux, and therefore, it can be deemed to behave as a monopole.

A monopole and anti-monopole pair will arise with a spin flip as the first excitation over the ice rule state and this gives three in-one out and three out-one in spin configuration (see figure 2.4). A dumbbell picture is used here to describe the situation. A dumbbell is obtained by replacing a spin by a pair of opposite magnetic charges (see figure 2.4 c and d). Therefore, a pair of monopoles

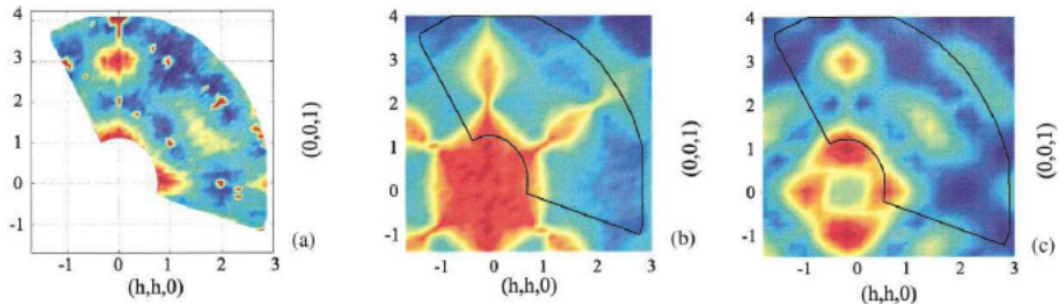


Figure 2.3: (a) Experimental neutron scattering pattern of  $\text{Ho}_2\text{Ti}_2\text{O}_7$  in reciprocal space at 50 mK. (b) Simulation of the reciprocal structure based on a spin ice model in which only ferromagnetic exchange coupling is considered. (c) The calculated neutron scattered intensity takes into account both dipolar interactions and weak nearest neighbour exchange coupling (antiferromagnetic). It captures the main detail of the experimental data more precisely than the nearest neighbour spin ice model. After Bramwell et al. [4]

can be separated by flipping a chain of adjacent dumbbells. During this flipping process, the magnetic charge of tetrahedra along the trace will return to overall charge neutrality since the ice rule is restored. It takes finite energy to separate the monopole pair, therefore, these monopoles are deconfined, as shown in figure 2.4 [6]. It is worth pointing out here that the monopole scenario does not violate Maxwell's equations. In fact, electromagnetic theory allows for such an excitation to occur.  $\nabla \cdot \mathbf{B} = 0$  implies that  $\nabla \cdot \mathbf{M} = -\nabla \cdot \mathbf{H}$ , which corresponds to the divergence of magnetic field  $\mathbf{H}$ . This gives rise to the magnetic monopole in  $\mathbf{H}$ . This monopole scenario has been confirmed by several experimental papers [31; 32; 33; 34].

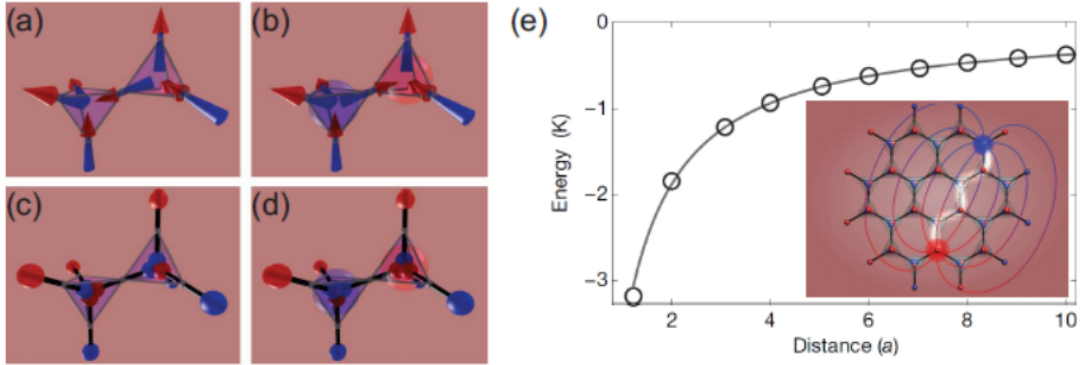


Figure 2.4: (a) The ground state of spin ice in two adjacent tetrahedra. Both tetrahedra follow the two spin pointing in and two spin pointing out ice rule. (b) The excited state of a pair of neighbouring tetrahedra is generated by flipping one spin from the ice-rule state. This gives rise to a monopole and anti-monopole pair with opposite signs of magnetic charge represented by red and blue spheres. (c) and (d) are the dumbbell model descriptions of (a) and (b) respectively. Each spin is represented by a dumbbell consisting of two magnetic charges. Therefore, in the ice-rule state, the net magnetic charge is zero at every vertex, while in the excited state two quasi-particles with opposite magnetic charge form. (e) Inset: the monopole and anti-monopole pair separate after flipping a chain of spins: only the two ends violate the ice rule. The curve is a magnetic Coulomb interaction (solid line) calculated based on  $-\mu_0 q_m^2 / 4\pi r$  compared with the numerical evaluation of monopole interaction energy (circle) in dipole spin ice as a function of monopole separation. After Castelnovo et al.[6]

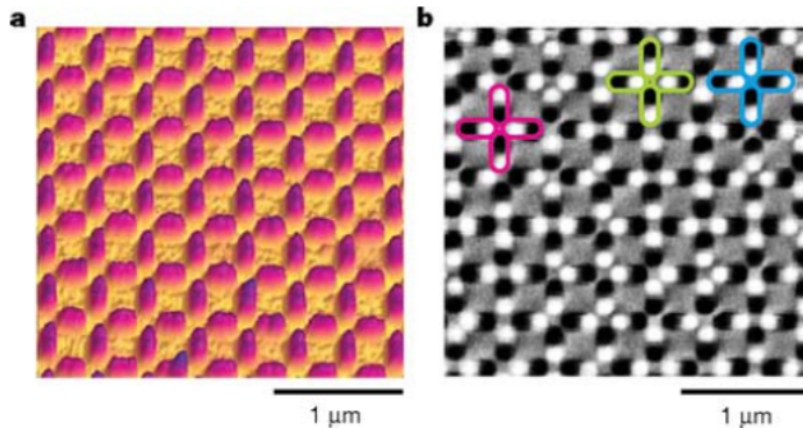


Figure 2.5: (a) AFM image of typical permalloy array with a lattice constant at 400 nm. (b) Magnetic force microscopy image of the same pattern. Each island consists of black and white dots, which correspond to the north and south pole respectively. The outline vertices are type 1 (pink), type 2 (blue) and type 3 (yellow). After Wang et al. [14]

## 2.2 Artificial spin ice

### 2.2.1 Introduction

Geometrical frustrations exist not just in atomic scale systems, but also in nano-scale artificial systems. For the latter, the structure is easier to design and probe via nano-scale microscopy tools. The artificial spin ice is such a system. It consists of 2-D magnetic interacting nano-islands made of permalloy. This material has little crystalline anisotropy and the shape anisotropy confines the magnetization of each nano particle along its elongated direction. Therefore each particle can be deemed to behave as an Ising-like macro-spin. Compared to real spin ice, the system has the advantage of being accessible at room temperature and has tunable inter-element interaction. The artificial spin ice system has drawn intensive interest lately. The main focus has ranged from energy minimization [15; 35; 36] to pattern design [14; 16; 37; 38], accessing well-defined statistic states [17; 39], field driven dynamics [40; 41] and so on.

The system consists of elongated magnetic islands at the nano-scale: a typical element is designed to be hundreds of nanometres in length and tens of nanometres in width. Numerical models [42] and simulations [18] have shown that this size of islands is sufficiently small to act as single domain, but big enough to maintain stable magnetic moment at room temperature. More precisely, the thermal energy for overcoming the kinetic barrier is up to  $10^5$  K. Therefore, the island is thermally stable at room temperature. The fabrication of islands with this size needs electron beam lithography. The fabrication details are given in chapter 3, section 3.1.

In 2006, Tanaka and co-workers [43] built a permalloy wire-based honeycomb network providing an analogue from the nano-wire network to the Ising system on the kagome lattice. The system is designed to be connected in order to perform the magnetization reversal and magnetoresistance measurement. In this study, the link between the nano-array system with water ice and spin ice has already been addressed. The connection was developed by Wang et al. [44] on a square array consisting of disconnected islands and this group of authors coined the name “artificial spin ice”.

In addition, several other similar lattices have been realized, such as triangular, brickwork, and quasiperiodic patterns [37; 38; 45]. In principle, an artificial ice system can be formed from any interacting Ising component, and therefore, a wide class of artificial system is built from superconducting flux vertex array [46] and colloidal version of artificial spin ice in an optical trap [47].

For the purpose of this thesis, a new quasi-periodic pattern, based on a Penrose tiling is studied for the first time. It must be pointed out that Bhat et al. [45] did some pioneering work on magnetic reversal measurement for quasicrystal pattern. Nevertheless, the main character of quasi-periodicity of this pattern like the ground state, thermal dynamic behaviour has not been investigated. These important features will be illustrated later on.

Because the system is stable at room temperature, the topography and magnetic configuration of the pattern can be obtained via AFM (Atomic Force Microscopy) and MFM (Magnetic Force Microscopy). The details of these methods are given in Chapter 3, section 3.2. Other methodologies are also employed to explore additional properties of such systems. For instance, a large portion of



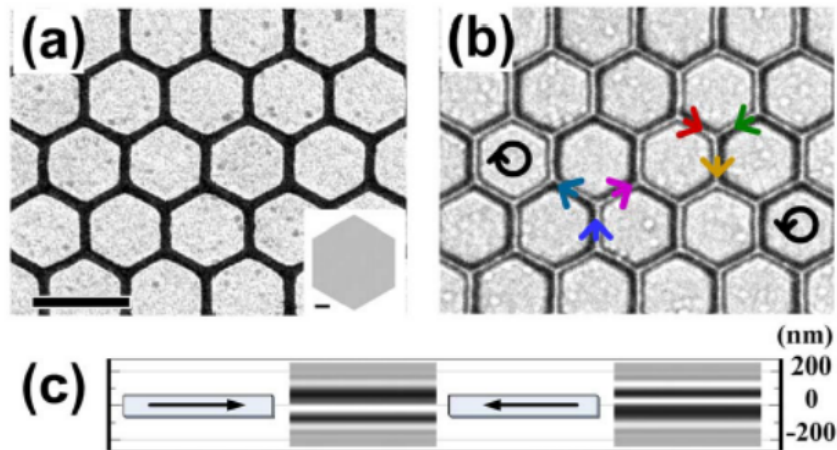


Figure 2.6: (a) A TEM image of kagome pattern. (b) Lorentz TEM image of the same pattern. (c) The simulation shows the moment direction based on the dark and bright edge. After Qi et al. [16]

the kagome pattern research was based on networked systems (see figure 2.6). In this case, MFM images fail to provide information about the magnetic alignment of the section part, which connects two junctions [16]. To solve this problem, Lorentz TEM (Transmission Electron Microscopy) is used to probe the local magnetic structure without ambiguity. The substrate needs to be transparent in order to allow the electron beam to go through. To observe the dynamic equilibrium of artificial ice system, some other techniques were employed, such as PEEM (Photoemission Electron Microscopy) with XMCD (X-ray Magnetic Circular Dichroism) which was used to determine the magnetization of individual elements. The system magnetic property also needs to be adjusted to fit the experiment condition [36; 48; 49; 50]. However, compared with AFM/MFM, the other apparatus mentioned above are much more expensive.

### 2.2.2 Square pattern and kagome pattern

In artificial spin ice systems, the symmetry of the 2-D is different from the 3-D spin ice. Four points in three dimensions may be equidistant, but this is impossible in

two dimensions. This causes two of the ice-rule states to have lower energy than the other four in two-dimensional system.

As shown in figure 2.7, the 16 possible configurations can be grouped into four types, labelled T1, T2, T3, T4 in the order of increasing magnetostatic energy for an isolated single vertex. The total energy for a single vertex is the sum of six pairwise interactions, including the first and second nearest neighbour pairs. Both favourable and unfavourable alignments for each type of pair are listed. type 3 and type 4 vertices have much higher energy than type 1 and type 2. Therefore, the low energy state of the pattern is dominated by the number of type 1 and type 2 vertices. T1 state is the lowest energy state, hence the ground state of square ice consists of type 1 vertices (see figure 2.7(a)). It follows a similar “two-in two-out” ice rule just as in real spin ice. However, in reality, in some experiments, the low energy state is made up of type 2 vertices rather than type 1 vertices [51]. This is because the energy difference of type 1 and type 2 vertices is too small, and therefore, a small magnetic field when coupled with the magnetic nano-element makes the type 1 vertex energetically unfavourable. Type 3 and 4 possess an excess of north or south, having normalized monopole moment. They present analogs of the fractionalized magnetic monopoles in real spin ice, but the difference is that these “magnetic monopoles” are not deconfined. The reason is that when separating a pair of “magnetic monopoles” in artificial spin ice, the vertex along the trace cannot revert to its initial state, hence costing extra energy.

The kagome pattern is a two dimensional array consisting of corner-shared triangular structures. The pyrochlore lattice in 3-D spin ice consists of alternating stacks of kagome layers and triangular layers when viewed along the  $\langle 111 \rangle$  direction. The magnetic monopole manipulation of spin ice when subjected to an external magnetic field along  $\langle 111 \rangle$  direction is mainly determined by the spin state in kagome layers. Being a very close analogue of this kagome ice state, with the added advantage of being directly accessible coupled with ease of construction, the kagome pattern in artificial spin ice is intensively exploited.

The kagome vertex possesses eight possible configurations that are split into two groups with different energies (see figure 2.8). All of the interactions across the vertex are equivalent, which leads to the corresponding “ice rule” of this

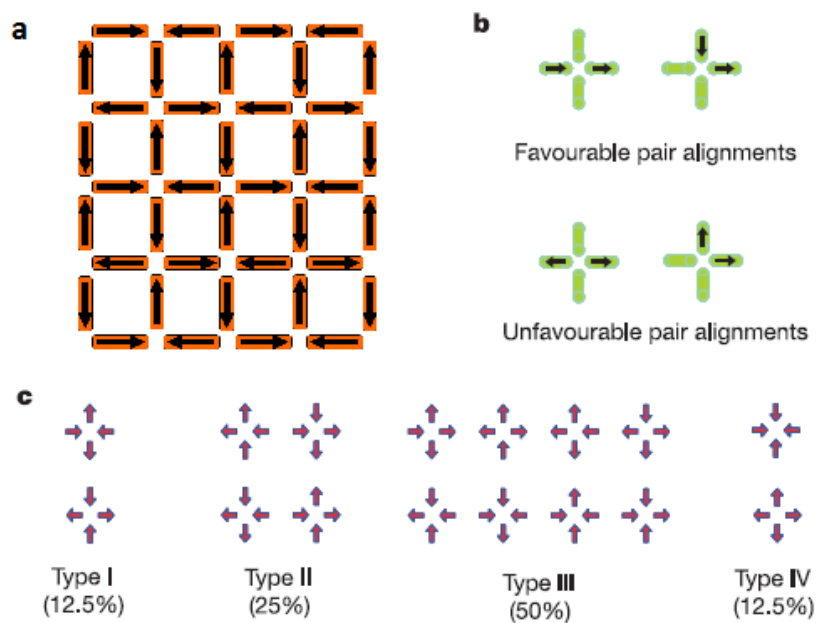


Figure 2.7: (a) The moment configuration is in one of the ground states. (b) Illustration of favourable and unfavourable dipolar interaction between pairs. (c) The 16 possible moment configurations for a single vertex, grouped into 4 different types. The percentage indicates the expected population when each element is randomly aligned. (b) and (c) is after Wang et al. [14]

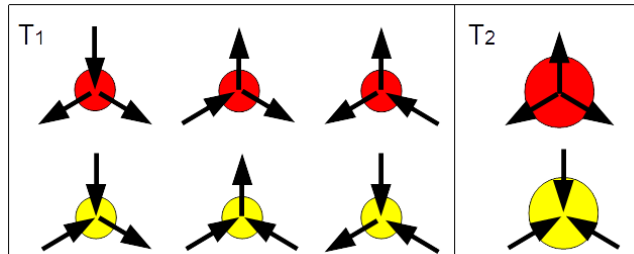


Figure 2.8: The eight possible moment configurations in a kagome lattice can be separated into two types. (a) Low energy type configuration, which follows the ice rule “two-in one-out” or “two-out one-in”. The coloured circles represents the normalized magnetic charge  $\pm 1$ . (b) High energy configuration possess normalized magnetic charge  $\pm 3$  (big coloured circle).

system to be modified into “two-in one-out” or “two-out one-in”. However, the “ice rule” in kagome patterns only works for nearest neighbour elements, and therefore cannot guarantee a long-range order. It has been predicted that the system undergoes two phase transitions on lowering the temperature, where the degeneracy of spin ice manifold is lifted by the long-range dipolar interaction [52; 53]. These thermodynamic phase transitions in kagome spin ice have been probed using low energy muon spectroscopy [54].

### 2.2.3 Accessing the ground state

#### Introduction

In such artificially designed systems, a prevalent point of focus is accessing the prescribed ground state via an “anneal” process [55; 56; 57; 58; 59]. For example, AC demagnetization was employed to form GS configurations in dipolar coupled nano-magnetic chains [60; 61]. In artificial spin ice systems, this methodology has been intensively used to generate low moment and low energy states [15; 44]. The demagnetization is described in the following section.

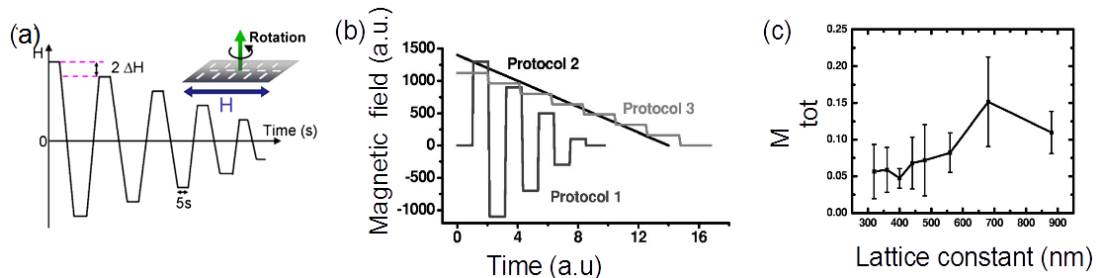


Figure 2.9: AC demagnetization protocols. (a) The sample is rotated along an axis that is out of plane. The external field is applied in plane with a square function profile. With each half period, the field decreases. After Ke et al. [15] (b) Schematic plot of three demagnetization protocols: protocol 1 is depicted in (a), protocol 2 presents a linear decrease in field without oscillation and protocol 3 has a step function profile without alternating field direction. (c) Residual magnetization as a function of lattice space, following protocol 1.

### AC demagnetisation

For a general AC demagnetization process, the sample is subjected to an external in plane magnetic field, which alternates in direction while also decreasing in magnitude. A series of demagnetization protocols were tested by Wang et al. [15; 18; 44] In order to do so, the sample was mounted on a rotating  $\sim 10$  Hz plate while subjected to an in-plane field, oscillating stepwise between opposite directions and decreasing magnitude. The plate rotation direction was out of plane (see figure 2.9(a)). The field starts above the coercive field  $\sim 700$  Oe (for the islands size of  $220 \text{ nm} \times 80 \text{ nm} \times 25 \text{ nm}$ ), which is nearly independent of the lattice constant. Then, the field holds each step for a few seconds and ramps at a rate of  $10 \text{ kOe/s}$ . The magnitude of the field is decreased by a step of  $10 \text{ Oe}$  every half period. Therefore, the whole process can be completed within minutes. A linear decrease protocol and a non oscillating step protocol were also tested, as illustrated in figure 2.9(b). These two protocols were reported to be less effective. It is worth pointing out that, as reported by another paper, the linear decrease protocol was proved to have the same effect as AC demagnetization protocol [62]. The demagnetized state of net moment  $M_{\text{tot}} \sim 0$ , as shown in figure 2.9(c), can

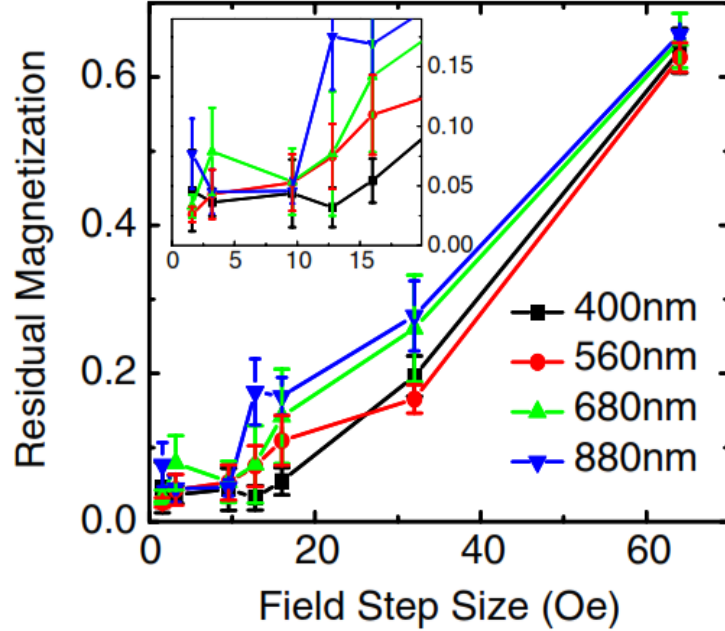


Figure 2.10: Field step-size dependent of residual moment. The state of effectively zero magnetization can be accessed when the step size is smaller than 12.8 Oe. The trends for four selected lattice constants are similar. The inset is a close-up view for low step size region. After Ke et al. [15]

be repeatedly accessed.

While the exact detailed process involved remaining unclear, several important results emerged from the initial work [15; 44]. It was shown that the external field for demagnetization works only in a narrow window around the coercive field. The residual moment is field step size and lattice constant dependent (see figure 2.10). When the step size is smaller than a specified value (12.8 Oe), the final state is effectively demagnetised. The net magnetic moment cannot uniquely specify the state. Therefore short-range magnetic correlations were employed to examine the low step region.

As shown in figure 2.11, further reducing the field step size makes the short-range correlation stronger. The net energy is further minimized as the field step size reduces (see figure 2.12). However, the ground state cannot be obtained

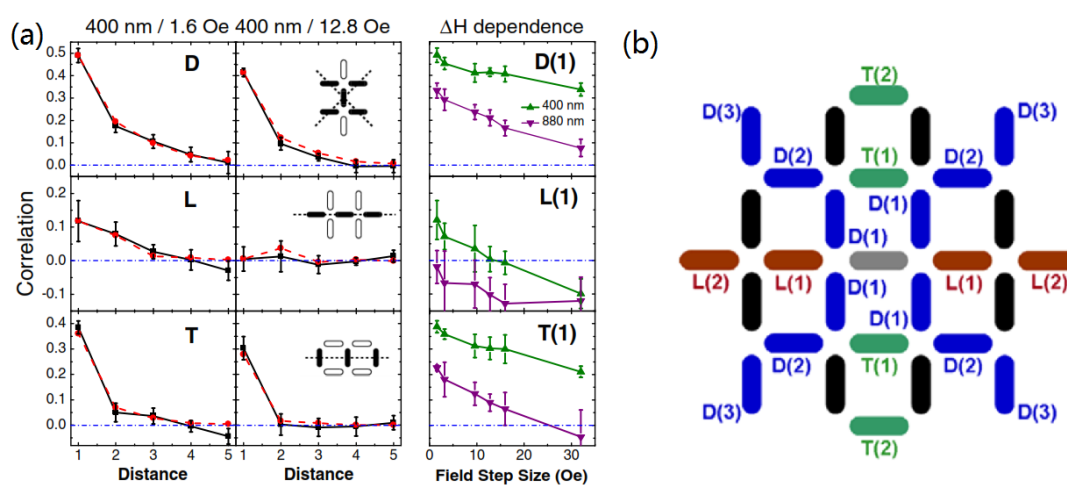


Figure 2.11: Control of short-range magnetic correlation via field step size and lattice constant. (a) Correlation for three different types of neighbour pairs as defined in (b), for 400 nm square lattice following AC demagnetization with  $\Delta H=12.8$  Oe and  $\Delta H=1.6$  Oe. The black curve is given by experiment, and the red curve is given by the Monte Carlo simulation. Correlations are stronger when the field step size becomes smaller. After Ke et al. [15]

via this method [15]. This is due to the geometry of the square pattern, which makes it impossible to transfer a type 2 vertex directly into a type 1 vertex, which requires a flip of two moments via type 3 configuration. The small step size field cannot overcome this barrier, while a large step size field will act to jam the high energy configuration. The demagnetization cannot anneal the system into its antiferromagnetic GS. The moment is in a static, disordered state, which is similar to the frozen state in spin ice. Nevertheless, these experiment results suggest a new model from which the population of local state can be predicted.

### Effective thermodynamics

Growing evidence shows [17; 39] that AC demagnetization can be treated as an effective thermal annealing process. This is not surprising, as both thermalization and AC demagnetization exert forces on each particle of the system, which can flip the moment of particle during the whole process. The difference is that the former is the result of local normally distributed thermal “kicks”, while the latter has a periodic directionality where all the moments experience the same applied field via dipolar interactions. Based on the result of Wang et al. [14], an equilibrium statistical mechanical formula is introduced by Nisoli et al. to describe the AC demagnetization process in terms of “effective thermodynamics” [17; 39]. An effective temperature is defined to understand the full statistical properties. This is not the first time effective temperature is used to analyze non-thermalization processes. It has been employed in vibro-fluidized granular systems [63] and powder mixture statistical studies [64]. Both of the processes are described as a Brownian motion behaviour. In the case of AC demagnetization, however, the process was described as more like stirring a box of sand rather than shaking it. Therefore, the description of the thermal-like process cannot be immediately employed on the demagnetization process.

The evidence initially comes from the statistical result: the expected value of dipolar energy of the square pattern after AC demagnetization closely tracks the  $T_2$  vertex energy (see figure 2.13). The average vertex energy of array in the AC demagnetized state can be written as  $\tilde{E} = \sum_i n_i E_i = E_2$ , where  $n_i$  denotes the fractional population of vertex types for  $i = 1$  to 4 and  $E_i$  are the vertex energies



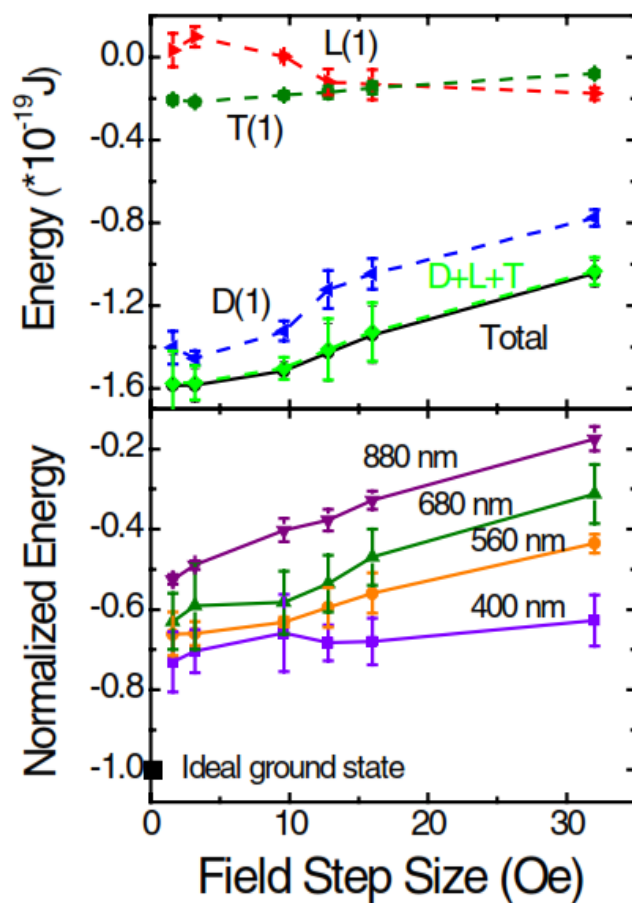


Figure 2.12: Top: Step size dependence of total magnetostatic energy for D(1), L(1), T(1) island pairs. The sum of the energies for these three pairs for 560 nm lattice spacing. Bottom: Normalized total energy for array with different lattice constants when demagnetized with different field step sizes. After Ke et al. [15]

respectively. The measured energy, as plotted in figure 2.13, fully tracks the calculated energy for the  $T_2$  vertex in each lattice constant pattern. The random average energy plotted in the inset of figure 2.13 implies that this relationship is from simple random average. In order to explain this phenomenon, the first approximation is a vertex-gas approximation where each vertex is treated as a single entity. As described in the 16 vertex model, each vertex can take one of four energy states  $E_i$  with degeneracy  $q_i$  equal to 2, 4, 8, and 2, respectively. As the prepared state before AC demagnetization is fully polarized along diagonal direction, all the vertices are initialized as type 2 vertices. When the external field is much higher than the coercive field, all the islands follow the external field. As the field magnitude gradually decreases, successive islands start to “fall-off” from the field, which subsequently carve out defect vertices from the background of type 2 vertices. As the field decreases further, these defects become arrested. The equilibrium fractional vertex population can therefore be calculated through maximizing the entropy  $S$  with respect to the number of configurations of vertices  $N_i$ . This can be written as  $S/Nk_B = (1/N) \ln \Omega = -\sum_i n_i \ln n_i/q_i$  with respect to  $n_i$ .  $\Omega$  is the total number of ways in which to arrange  $N$  vertices with  $N_i$  configurations of each vertex and is given by

$$\Omega = N! \prod_i \frac{q_i^{N_i}}{N_i!}. \quad (2.1)$$

It was found, however, that the predicted population based on this theory does not agreed very well with the observed population from the MFM image. This is not too surprising, as the demagnetization is a non-thermal process. A modified theory is given later in which the background “diagonal polarized state” population, as well as the defect vertex population, was taken into account. Now, the  $\Omega$  in equation 2.1 can be written as

$$\Omega = \frac{N!}{(N-D)!} \prod_i \frac{q_i^{N_i}}{N_i!}, \quad (2.2)$$

and entropy can be written as  $S/Nk_B = -[\rho \ln \rho + (1-\rho) \ln 1-\rho] + \rho\sigma$ . Maximizing the entropy under a vertex energy constraint  $\sum_i \nu_i E_i = E_2$  gives the canonical distribution of defects

$$\nu_i^* = \frac{q_i \exp(-\beta E_i)}{Z}. \quad (2.3)$$

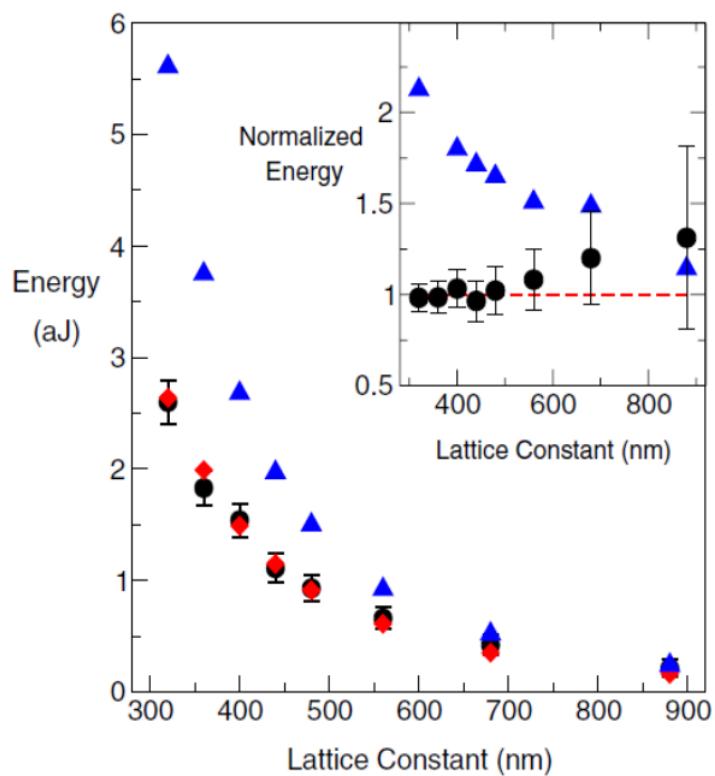


Figure 2.13: Calculated  $T_2$  vertex energy (red diamonds) compared with average vertex energy  $\tilde{E}$  (dots). These energies are very close to each other at each lattice spacing. The randomly aligned energy is also plotted (triangles) and has a different value, especially when the lattice spacing is small. The inset shows the specific energy and the randomly aligned energy, normalized to pure  $T_2$  vertex energy at each lattice constant (red line). After Nisoli et al. [17]

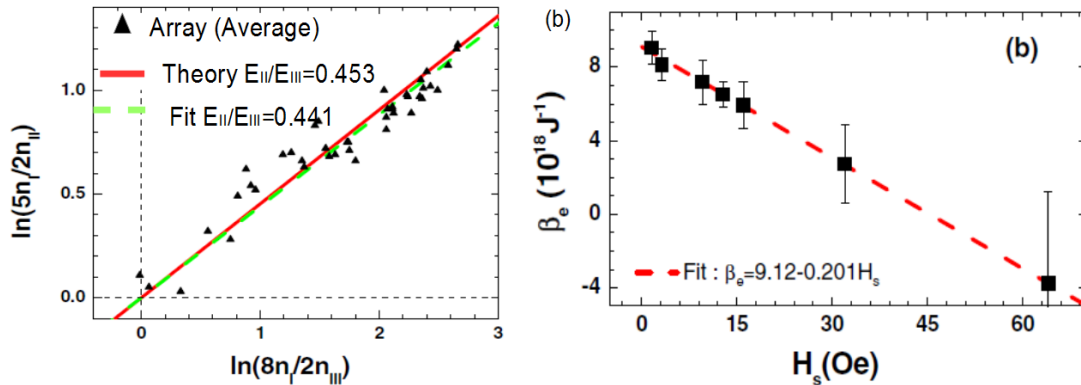


Figure 2.14: (a) The effective temperature of square array.  $n_I, n_{II}, n_{III}$  are relative population of type  $I, II, III$  vertices. The ratio given by theory roughly matches the ratio given from the linear fit from the experiment. (b) The effective temperature extracted from the experiment has a linear relationship with the step size of the demagnetization process. After Nisoli et al. [39]

$Z$  is the partition function over  $\nu_i^*$ , Equation 2.3 gives

$$\beta(E_j - E_i) = \ln \left( \frac{q_j \nu_i}{q_i \nu_j} \right). \quad (2.4)$$

As each vertex energy can be estimated by using the “dumbbell model” in which the islands are treated as a dumbbell of monopoles, the ratio between different populations of vertex types can be predicted from the equation 2.4. This value agrees well with the ratio of population of each type vertex read from MFM images (see figure 2.14(a)).

Further, equation 2.4 allows for an effective temperature  $T_{\text{eff}} = 1/k_B\beta$  of a state to be inferred from an MFM image by counting the vertex populations. Not surprisingly, Nisoli found that this effective temperature had a linear dependence with the step size of the AC demagnetization process figure 2.14(b), which indicates that this effective temperature description has basic physics akin to real temperature.

### 2.2.4 Thermal behaviour in artificial spin ice

The AC demagnetization protocol can reduce the total energy of the square artificial pattern: however, it is found that the ground state cannot be obtained via this method. Therefore, consideration is given to the true thermalisation process. As reported firstly by researchers at the University of Leeds [65], the ground state of a wide-range order in a square ice pattern was found from the as-grown pattern (see figure 2.15(a)). Over  $\sim 20$  lattice constants long-range order is observed from macroscopic images. The frequency of different types of elementary excitation in the background of the ground state were found follow the Boltzmann law (see figure 2.15(b)). Based on this fact, the authors of this paper [65] argued that the state observed is frozen-in residue of true thermodynamic processes that occurred during fabrication.

This is a reasonable conclusion, since when the sample is in the initial stage of fabrication, the thickness and thus the volume of elements was small enough so that the shape anisotropy energy of element  $E_A$ , ( $E_A = KV$ ,  $K$  is anisotropy constant,  $V$  is the volume of element) can be overcome by the thermal energy. Hence the thermal fluctuation was active and the elements behave like superparamagnetic. As the nano-islands are being grown, the height and thus the volume of islands increase, which induce higher energy barriers. The thermal fluctuation progressively slows down and the islands moments are frozen at some point during the fabrication stage. During this process, the dipolar interactions between the neighbouring islands plays an important role. It slightly changes the energy barrier in the reverse direction of elements. Therefore, the magnetic moments of each vertex transfer towards their most favourable configurations during the magnetic materials deposition stage. These excitations therefore are expected follow the Boltzmann law for an effective temperature that matches the real temperature when the system is arrested.

This finding proved that the thermal fluctuation can indeed induce the long-range ground state order in the artificial system and triggered intense theory and modelling efforts [66; 67]. However, the as-fabricated state study is a limited methodology. First, the ground state formation is not easy to reproduce due to

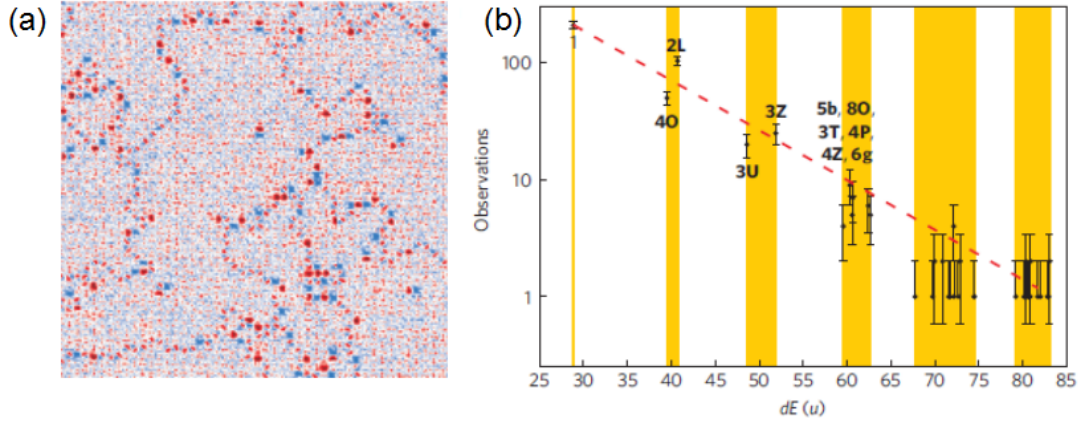


Figure 2.15: (a) Direct observation of the long-range ordered GS in a square pattern with  $\sim 10 \mu\text{m}$  width domain. (b) The frequency of a given excited state against the excitation energy with an exponential fit in red. After Morgan et al. [65]

the wide range of fabrication parameters. Besides, the as-grown state can easily be destroyed by external field and cannot be recovered, which complicates systematic studies. In order to circumvent these limitations, alternative methods were developed. As discussed above, when the system temperature is much lower than the blocking temperature, the thermal fluctuation is suppressed. For the most intensively used material, permalloy, the blocking temperature is much higher than room temperature. Therefore the thermal fluctuations of artificial spin ice are hard to observe at room temperature for typical island sizes. The high temperature observation is beyond the current experimental condition. To solve this problem, the properties of the islands need to be adjusted.

In a pioneering work, Kapaklis et al. [51] changed the material's Curie temperature by modifying the constitution of the material. The material for the nano-element was replaced with  $\delta$ -doped Pd(Fe). The Curie temperature of the film can be tuned by changing the thickness of the layer [68]. This modification can allow the Curie temperature of material to drop from  $\sim 900$  K to 230 K. The magnetization of system is found to fall to zero in a faster way than for the continuous film, which is called the “pre-melting” phenomenon (see figure 2.16(a)).

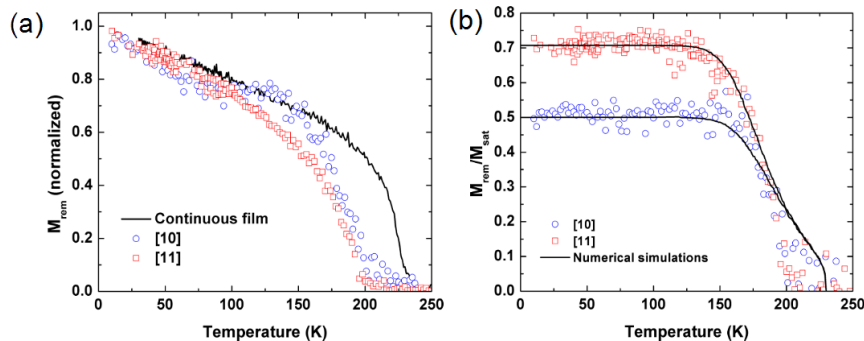


Figure 2.16: (a) Normalized remanent magnetization of array as a function of temperature after a field applied along horizontal ([10]) and diagonal ([11]) direction, compared with the remanent magnetization of the continuous film used for patterning. The array moments collapse at a temperature below the Curie temperature of the material ( $T_c = 230$  K). (b) The ratio of remanent to saturation magnetization of array compared with numerical simulation. After Kapaklis et al. [51]

This is believed to be caused by the disordering of macro-spins occurring at a temperature below the Curie-temperature. The order of macro-spins is due to the magnetostatic interactions between them, and therefore, the macro-spins start to become disorder before the sample reaches the paramagnetic state. The pre-melting experiment was tested by two different initial states which were induced by the application of an external field at a different direction at the beginning. The ratio of remanent to saturation magnetization of each state, therefore, is different (see figure 2.16(b)). For both states, the ratio decays are all consistent with the numerical simulation results. Furthermore, no phase transition to an ordered state was observed. However, each chain of the array is believed to be ordered at a finite temperature, which is confirmed both by the Monte-Carlo simulation and the analytical solution for a 1-D finite Ising chain of macro-spins. The finite size chain order, therefore, is believed to be the origin of pre-melting phenomenon. This pre-melting phenomenon shows that a real thermal dynamic artificial spin ice array is created: however, the system remains disordered even at temperatures close to zero.

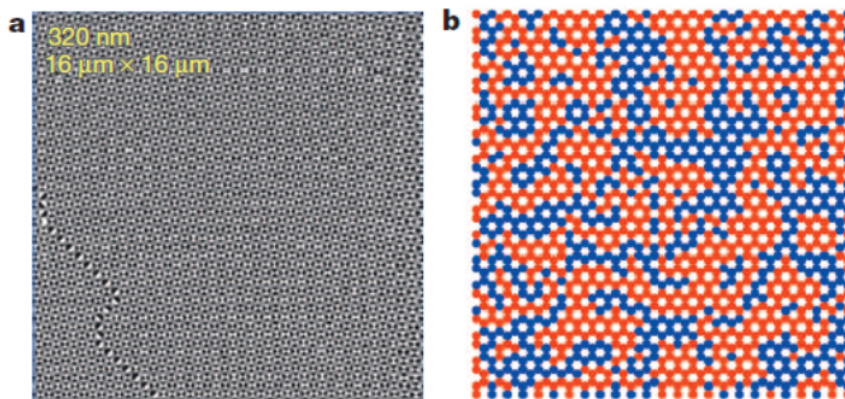


Figure 2.17: (a) The MFM image of square pattern with 320 nm lattice space after thermal annealing at (542.5°C). Pattern size is 16  $\mu\text{m} \times 16 \mu\text{m}$ . Only a few islands are not in the ground state. (b) Magnetic charges maps from MFM image of kagome pattern with 260 nm lattice space. The red and blue correspond to the two magnetic charge ordered states. After Zhang et al. [69]

In order to access the ground state of an artificial system, other protocols were developed. In 2013, a group in the Pennsylvania State University succeeded in approaching the well-defined ground state of the square pattern with small lattice spaces [69]. Here, an alternative method is employed. A special layer  $\text{Si}_3\text{N}_4$  is deposited on the surface of Si in order to increase thermal stability. This special layer protects the sample from film-substrate interdiffusion. The sample was heated above the Curie temperature of its constituents (542.5°C), and then cooled down to room temperature. Carefully choosing the heating and cooling rates, the artificial square pattern approaches the GS across the whole sample and only a few domain boundaries arise. This protocol can be repeated as many times as desired. Not surprisingly, the population of elementary excitation in the thermally annealed square pattern sample has been found to follow the Boltzmann law, which was reported earlier in the as-grown square pattern [65]. The ground state ordering observed in artificial square ice pattern revealed a significant difference between artificial square ice and real spin ice, as it is believed the latter cannot access an ordered ground state due to frustration. This indicates that the frustration in artificial spin ice is weaker than the real spin ice.



The kagome pattern subjected to the thermal annealing protocol was also investigated in this paper. For the kagome pattern, the net magnetic charge for a vertex of three islands is  $\pm 1$  when obeying the pseudo ice rule. Theoretical work [52] has showed that when the kagome spin ice is cooled down from the paramagnetic state at a high temperature, the system will experience a phase transition from the kagome ice I state, in which magnetic charges are disordered but all the spins obey the pseudo ice rule to the kagome ice II state in which magnetic charges are ordered and all the spins obey the pseudo ice rule. In this paper, the thermal annealing experiment has shown that for all the samples with a small lattice constant, all the vertices follow the pseudo ice rule after thermal annealing, which indicates that the system is at least in the kagome ice I state. In a sample with a small lattice constant (260 nm), incipient charge order starts to emerge (see figure 2.17).

For most of the artificial spin ice studies, the system can be treated as an athermal system at room temperature, and therefore, the AFM/MFM technique is sufficient for any static study. In order to investigate the thermal dynamic property of system, some other apparatuses are required. Photoemission Electron Microscopy with X-ray Magnetic Circular Dichroism (PEEM-XMCD) was employed to detect the magnetization distribution of the whole pattern [36; 48; 49; 50]. In a recent study, low energy muon spectroscopy was used to probe the dynamic behaviour in kagome spin ice [54]. These techniques offer the advantage of fast imaging and being sensitive to thermal fluctuation but are also quite expensive.

## 2.3 Penrose pattern

### 2.3.1 Introduction to the quasi-periodic pattern

Periodic solids, or crystals, as a basic concept of the solid state of physics, have been investigated for centuries. Most of the important theories and properties of solids, like the phonon vibration theory, the Bloch theory, the electron transport theory, etc. are based on the assumption that atoms sit periodically on lattices. These theories, however, give different results when the atoms are not arranged

periodically. This has already been verified in disordered systems like glass, where any long-range order is absent.

Apart from ordered and disordered systems, there are quasi-periodic systems whose order is between these two but was not investigated until a few decades ago. As these materials do not possess translational symmetry but instead have rotational symmetry, it was expected that they may possess exotic properties. For example, the unique Bragg diffraction pattern of quasicrystal shows sharp peaks with a five or ten-fold symmetry. This discovery required the International Union of Crystallography to modify the definition of crystals, and acknowledge that the diffraction pattern can be generated either by periodicity or aperiodicity. There are two types of quasicrystals have been realized: the first type is periodic along certain axes, and quasi-periodic, in a plane normal to the axes. The second type is aperiodic in any direction.

### 1-D quasi-periodic pattern

A very useful example is the Fibonacci chain. This can be built by any non-periodic procedure. For example, if we start with two segments, one short  $\mathcal{S}$ , one long  $\mathcal{L}$ , and then if we apply iterative rules to replace each  $\mathcal{S}$  with  $\mathcal{L}$  and each  $\mathcal{L}$  with  $\mathcal{L}\mathcal{S}$

$$\begin{aligned} \mathcal{S} &\rightarrow \mathcal{L} \\ \mathcal{L} &\rightarrow \mathcal{L}\mathcal{S}. \end{aligned} \tag{2.5}$$

After several operations, we could get longer strings. This iteration could be repeated infinitely to get infinite strings. The resultant string has typical quasi-periodic pattern properties, like:

(I) self-similarity: the string after  $n$  step iteration  $F(n)$  can be constructed from the previous two strings, i.e  $F(n) = F(n - 1) + F(n - 2)$ .

(II) Quasi-periodicity: the string does not have any periodic repetitive sequences on any scale; on the other hand, the type of segment of the chain at any point can be inferred from the initial sequence. This means that it still possesses long-range order. Due to the simplicity of the Fibonacci chain, it will be used to demonstrate how to generate a quasi-periodic array from a high dimension space.

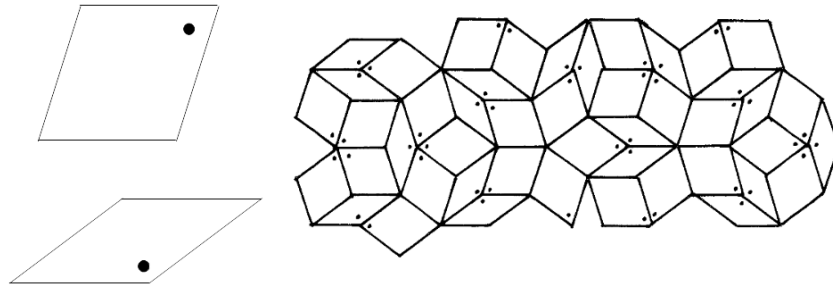


Figure 2.18: Penrose tiling consists of two types of rhombuses: thin and thick. These have to follow matching rules to form a continuous layer, which state that the vertices of rhombuses when consisting of a vertex in Penrose tiling, has to be either all dot or all blank. An example is given on the right.

### 2-D quasi-periodic pattern

In 1974, Roger Penrose showed that a plane could be tiled by two elements in a non-periodic way. This is the well-known Penrose tiling pattern [70]. These two classes of units derive their names from their shapes, which are “kite” and “dart”, respectively. Subsequently, other sets of tiling have been discovered as having the same features as “kite ” and “dart”. One intensive study set is a pair of rhombuses, called the thin and thick rhombuses. Besides, it was found that the Penrose pattern can be constructed by one type of decagon overlapping in two different ways [70]. In each case, the basic tile needs to follow the so-called “matching rule” to avoid overlap [71]. As illustrated in figure 2.18, the vertices of rhombuses when forming a vertex in a Penrose pattern have to be either all dot or all blank. This matching rule can generate various types of Penrose tiling.

#### 2.3.2 How to generate a Penrose pattern

Describing a periodic pattern mathematically is quite simple, as, due to translational symmetry, all positions in the periodic pattern can be written by a set of unit vectors. It becomes, however, non-trivial in quasi-periodic patterns, which

do not possess translational symmetry. As a matter of fact, apart from the 1-D quasi-periodic chain, no formula has been found to describe the 2-D and 3-D quasi-periodic patterns so far. Instead, most methods are based on the self-similarity property, such as: inflation of elementary units [72; 73; 74] and growth from initial seed [70]. In this project, we choose a method called “cut and project” whose details can be found in Appendix A. This method can be summarized as projecting points of a 5-D hypercubic lattice along a special direction onto the physical 2-D plane. This method is advantageous for obtaining the coordinates of each vertex location as well as the neighbouring vertices. Based on this method, we developed a program that can trace each vertex and its neighbouring coordinates as well as the magnetic charge from an MFM image. All these results will be shown in chapter 5.

### 2.3.3 Study on quasicrystal materials

Since long-range order exists in a quasi-periodic pattern, people expect that similar magnetic long-range order may arise in real materials with quasi-periodic structure: a quasicrystal. Experimentally, for a long period, the study was limited by the aluminium transition metal based quasicrystals, which were the only magnetic quasicrystals. In these systems, the magnetic moment per transition metal is very small, therefore, and therefore it is hard to form long-range magnetic order in these compounds.

In 1993, an icosahedral quasicrystalline phase compound Zn-Mg-R (where R is a rare earth element) was discovered. These materials offered an opportunity to study the magnetic behaviour in quasicrystal materials [10; 75; 76]. These materials have well-localized  $4f$  electrons and sizeable moments. Due to this feature, rare earth based quasicrystals were intensively studied by diffraction of x-rays, electrons and neutrons [10; 77; 78; 79; 80].

The x-ray diffraction experiment confirms that the rare earth ions sit quasi-periodically on the quasicrystal [81]. In 1997, Charrier et al. performed neutron diffraction experiments on powder samples [82]. They reported that magnetic long-range order was found when the temperature was below 7 K. This result,

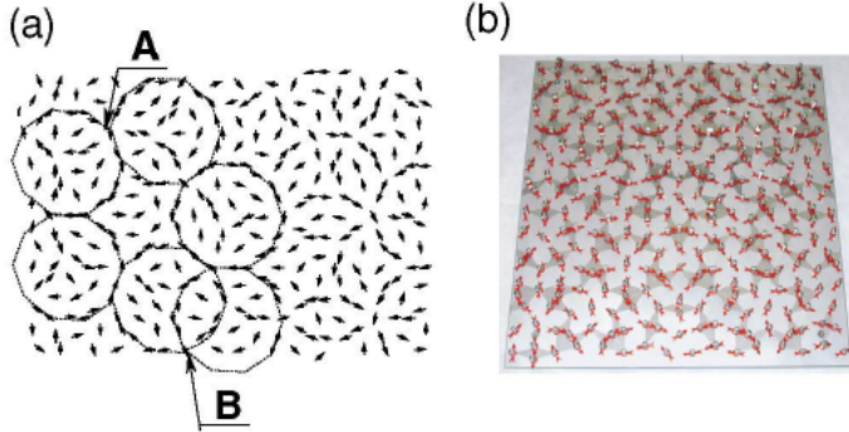


Figure 2.19: (a) The Monte Carlo simulation for pure dipolar interactions. The spins are divided into two parts. One is in ordered state consisting of a perimeter of decagon rings. The rest are in disordered spin glass-like states inside the decagon. (b) The experimental part, magnetic bars on a millimetre scale were fixed onto the nodes of a Penrose tiling, but able to rotate freely. After Vedmedenko et al. [9]

however, is neither consistent with AC susceptibility nor with the  $\mu$ SR experiment [83; 84]. Later, in another neutron experiment [85], Takakura et al. found magnetic short-range order in  $\text{Zn}_{60}\text{Mg}_{31}\text{Ho}_9$ . This was the first time that at least short-range order was confirmed in a quasicrystal. After several neutron experiments [75; 83], this became an accepted conclusion.

The magnetic order in the quasi-periodic structure has already been studied as a fundamental issue theoretically, while quite a few anomalous behaviours were predicted, such as “spiky peaks and pseudo gap at the Fermi level”, and “criticality” in electron wave functions [86; 87]. Nevertheless, these anomalies in real quasicrystals are contradictory with experiments result. Only short-range exchange interactions were taken into account in these theoretical studies. Long-range dipolar interactions have not been considered (see a review in [88]). On the other hand, due to the sizeable magnetic moments of the rare earth elements, the long-range dipolar interactions could compete with short-range exchange interactions, which have already been reported in the spin ice materials [4]. This

feature lets other methodologies be employed to investigate the magnetic order in the quasi-periodic structure. In 2003, Vedmedenko [9] did some pioneering work on the magnetic order in Penrose tiling. In the experimental part, a 2-D micro-structure model was constructed by putting millimeter-scale magnetic bars onto the nodes of a Penrose tiling in-plane (see figure 2.19). This corresponds to the pure dipolar interaction case. Studies have shown that after several relaxations, the total energy of the pattern is always identical. This implies that the ground state in the case of pure dipolar interaction is highly degenerated. The Monte Carlo simulation shows that when the exchange interactions are set to be zero, the ground state consists of two parts: one is the ordered decagon ring, and the other part is the spin glass-like part inside the decagon. The result is consistent with the phenomenon discovered in 3-D quasi-periodic materials.

Another study concentrated on the collective behaviour of aperiodic pattern in nano-scale presented was conducted by V. S. Bhat et al. [45] The Penrose tiling pattern investigated is constructed by the “kite” and “dart” units and the edges are joined to form a continuous network, as shown in figure 2.20. Broadband FMR (Ferromagnetic Resonance) measurement and DC field sweeping were performed on different scale patterns. The FMR absorption experiment showed asymmetry mode existing in the spectra. These spectra are applied field angle dependent and have ten-fold symmetry (a same spectrum arises when rotating the sample by 36 degrees each time). A series of knees arose in the hysteresis loop from the experiment and simulation, which were found to depend on the scale of the pattern and temperature. These knees were associated with the abrupt reversal of groups of equivalent segments in the networked pattern. This suggests that collective behaviour exists along the segment. Neither frustration nor thermal dynamic behaviour were discussed in this paper.

## 2.4 Summary

Artificial spin ice is the realization of the 2-D Ising model and a 2-D geometry frustrated system. Experiments for the manipulation so far have focused on field and thermal-based forcing. Various models and methods were employed to analyze these results, such as “effective temperature”, “pseudo magnetic charge”,

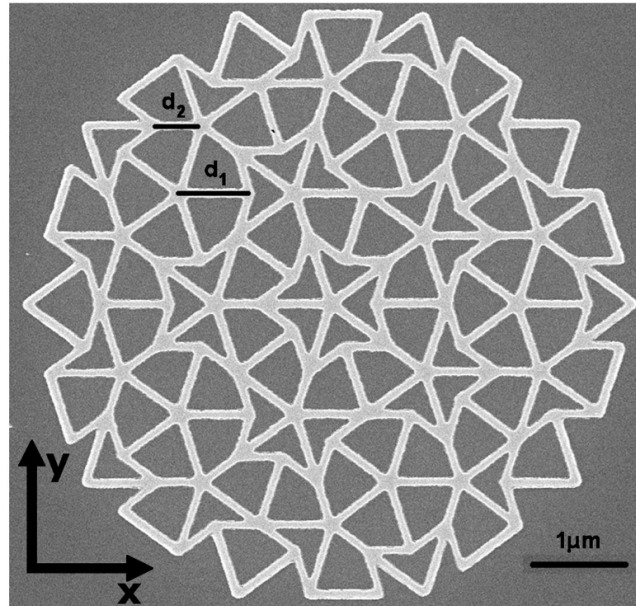


Figure 2.20: SEM image of wire networked Penrose tiling: the black part is silicon, the bright part is permalloy. The units in this pattern are “kite” and “dart” as named after the shape. Segment lengths are  $d_1=810$  nm,  $d_2=500$  nm, and the width is 85 nm. Image is after Bhat et al.[45]

“macro-spin” correlation as well as entropy calculation, among others [17; 36; 51; 69]. All these models and methods, when applied to different geometries give different results, which suggested the physical properties of the artificial spin ice are strongly geometry dependent. Therefore, distinct features are expected to arise in the Penrose tiling pattern.

# Chapter 3

## Methods

### 3.1 Electron Beam Lithography

The technique of electron beam lithography (EBL) dates to the late 1970s, and was widely used for sub-micron structure patterning [89; 90; 91]. EBL utilises a focused electron beam onto a substrate, which is coated with an electron sensitive polymer resist. It forms a lateral nanoscale template, into which materials can be deposited on the substrate. A typical EBL process is shown in figure 3.1. Initially, the electron sensitive resist dissolved in solvent is spin-coated on the substrate at several thousands RPM. The solvent is then subsequently evaporated by heating the substrate, leaving a resist layer with  $\sim 100$  nm thickness. The resist is then exposed to the focused electron beam in vacuum. The electron beam can penetrate into the resist and carve the desired pattern on the resist layer. The electron beam spot is controlled via a computer with patterning software. During this stage, it is essential to choose the correct current and exposure time to achieve the desired dosage.

Material can be deposited on the pattern by the common thin film growth techniques, such as sputter deposition or evaporation. Following this procedure, the remaining resist and material deposit on the resist can be removed by putting the sample in a solvent bath. This procedure is called “lift off”. The desired pattern is retained after the lift-off process.

All the samples used in this project were fabricated at the Center for Functional Nanomaterial (CFN), Brookhaven National Laboratory (BNL). The EBL



used was a JEOL 6300-FS. A single layer of ZEP520A resist was spun on the silicon substrate, baked at 180 °C for 3 min, giving it a thickness of 100 nm. The electron beam current is 150 pA, the beam step size of 1.75 nm was proximity-effect-corrected. The thickness of 25 nm Ni<sub>80</sub>Fe<sub>20</sub> and 2 nm of Ti of films were deposited by the electron beam evaporation.

### 3.2 AFM/MFM

AFM (Atomic Force Microscopy) is a scanning probe microscopy technique, which has been widely used in surface scanning since the mid 1980s. The first AFM results were published by Gerd Binnig, Calvin Quate, and Christopher Gerber in 1986 [92]. This technique is based on Scanning Tunnelling Microscopy (STM). Instead of using an STM tip whose direction is perpendicular to the surface, the AFM tip consists of a cantilever arm and a small  $\sim 10$  nm tip protruding from the end of cantilever. Therefore, the tip end is just above the surface of the material and exerts a force (mainly van der Waals force) on the sample. The force has a magnitude similar to the inter-atomic force. According to the nature of tip motion, AFM operation can be described by three modes: contact mode, tapping mode, and non-contact mode. For the tapping mode used in this project, the tip is driven to oscillate near its resonant frequency  $\sim 100$  kHz. The amplitude is around 10 nm - 100 nm.

All the AFM images in this thesis were generated using Veeco Multimode and Veeco Nanoman systems (both available in Leeds) operating under tapping mode. The tip is Veeco MESP (Magnetic Etched Silicon Probe) cantilever. A diagrammatic representation of operation is given in figure 3.2. When the tip is close to the surface of the materials, the van der Waals force between the tip and the surface will cause the cantilever to bend and this bending will cause a shift in the resonant frequency of the cantilever. This shift will be monitored and recorded when the tip is raster scanned over a given area of sample surface. As figure 3.2 shows, the oscillation of the cantilever is normally monitored by a laser beam, which is reflected by the cantilever onto photo detectors. The cantilever is micro-fabricated and has a spring constant of the order of 1 N/m and resonant

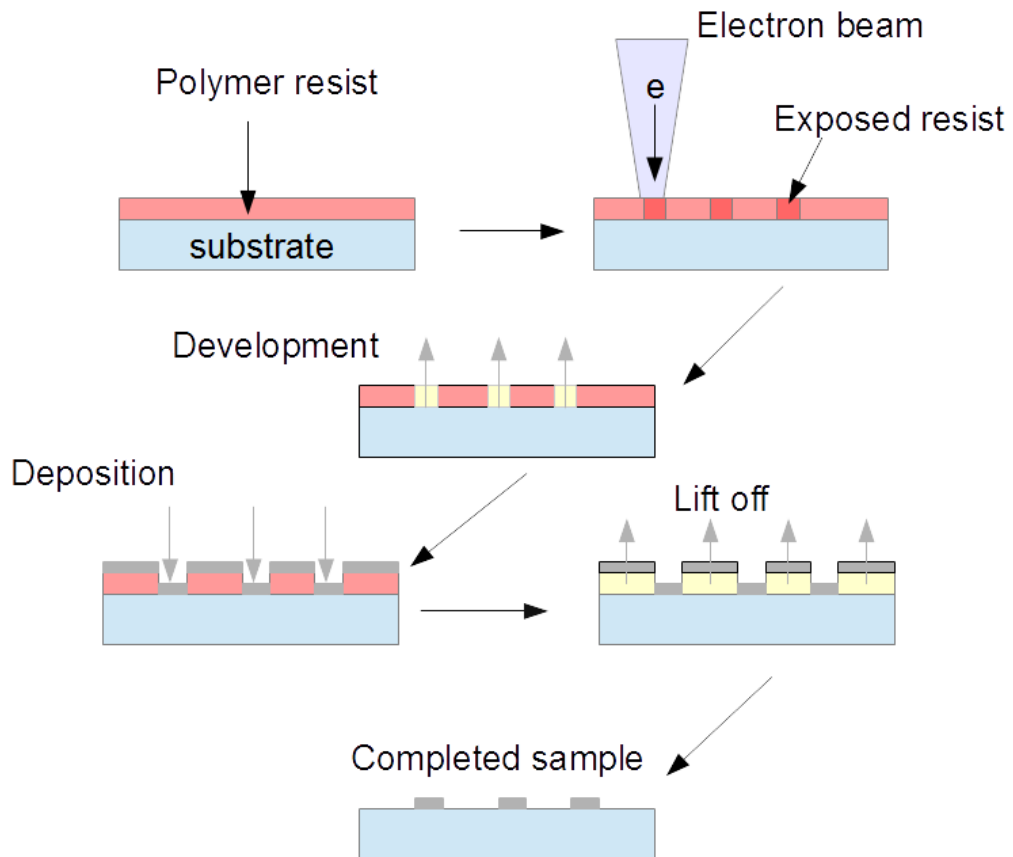


Figure 3.1: Schematic process of the EBL technique: an electron sensitive polymer resist coated on a substrate and dried. Then the electron beam controlled by the computer is incident on the surface of the sample, and exposes the pattern in the resist. In the development section, the exposed resist is removed by development. A desired thin film of material was then deposited onto the surface of the resist and substrate through the gap. After this stage, the resist was removed in the solvent lift-off process, and the final patterned sample remains.

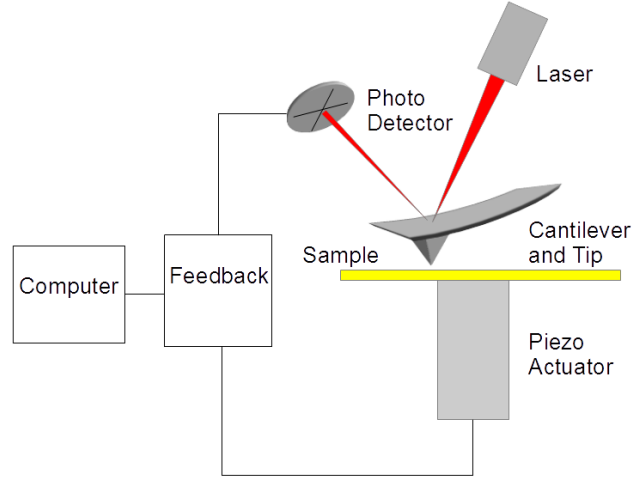


Figure 3.2: Tapping mode of AFM operation. The details are described in the main text.

frequency  $\omega/2\pi$  of tens of kHz, which is high enough to support fast raster scanning. The cantilever is then driven to oscillate by a driving force of set amplitude  $F_0$  and frequency  $\omega_d$  near or at its resonant frequency  $\omega_R = \sqrt{k/m_{\text{eff}}}$ , where  $k$  is the spring constant and  $m_{\text{eff}}$  is the effective mass of the cantilever. The behaviour of cantilever can be described by an equation of damping and forced harmonic oscillation with the solution of amplitude  $D_0 = (F_0/m_{\text{eff}})/\sqrt{(\omega_R^2 - \omega_d^2)^2 + (A\omega_R^2\omega_d^2)}$  [93; 94]. When the cantilever is driven to the surface of a material, this frequency will shift due to the gradient of the interaction force. The spring constant then becomes  $k_{\text{eff}} = k - F'$ , where  $F'$  is the gradient of the interaction force [92; 95]. In order to initiate operation, a cantilever is driven close to the surface. During this process, the frequency and amplitude keeps changing until an amplitude set point in  $D_0$  is achieved. When the tip raster scans the surface line by line, the variation of topography will result in variation in  $\omega$  and  $D_0$ . A closed loop feedback system maintains a constant  $D_0$  via the adjustment of tip and sample separation. This is recorded line by line to build a 3-D topography of the material surface. Adjustable parameters, such as scan speed, scan size, integral gain and

Table 3.1: MESP - Magnetic Etched Silicon Probe - Specifications

Parameter	Quoted Value (for LM-MESP low moment tips)
Thickness	2.5 - 3.5 $\mu\text{m}$
Length	200 - 250 $\mu\text{m}$
Width	23 - 33 $\mu\text{m}$
Resonant frequency $f_0$	60 - 100 kHz
$k$	1 - 5 N/m
Co/Cr layer thickness	10 - 250 nm
Coercivity $H_c$	400 Oe ( $< 400$ Oe)
$\mu$	$1 \times 10^{-13}$ emu ( $0.3 \times 10^{-13}$ emu)

proportional gain allow for surface tracking to be optimised.

The Nanoman system used in Leeds has a maximum view of  $40 \mu\text{m} \times 40 \mu\text{m}$  and a moderately sized image  $512 \times 512$  pixels, which normally requires tens of minutes to acquire. Figure 3.3(a) is a portion of the AFM image of Penrose artificial spin ice with lattice constant of 1000 nm. The resolution of the image can be the order of 10 nm under the reasonable ambient conditions. The image is basically a convolution of the surface of the material with the shape of the given tip. Therefore, the resolution of AFM is mainly limited by the tip size. The tip can become blunted under scanning, which can result in an exaggerated feature such as edge crown [96].

### 3.2.1 MFM

Not long after the invention of AFM, the study of magnetic tip-sample interaction led to this technique developing into “magnetic force microscopy” [97; 98]. The measurement can be performed under an operated mode of the Veeco AFM system. For measurement in this thesis, a MESP cantilever coated with magnetic material (e.g. Co/Cr) was used 3.1. Before performing the scan, the tip is magnetised vertically using a small permanent magnet. The tip therefore is like a magnetic dipole object. It is sensitive to the normal component of the gradient of the stray field from the sample surface. The tip performs an initial line scan in AFM tapping mode operation to obtain the topography profile of the sample

### 3.3 Interpretation of microscopy data

---

surface. A second scan across the same line is then made at a user-defined height above the topography profile. This height is typically around 10 - 100 nm, to eliminate the non-magnetic interaction variation between tip and sample. The component of gradient of the stray field variation therefore acts to change the resonant frequency and effective spring constant of the cantilever. For example, a repulsive force decreases the magnitude of oscillation, which effectively enhances the spring constant of the cantilever. These variations can be mapped from the phase and amplitude of the cantilever oscillation to create an image representative of the magnetic charge distribution. As shown in figure 3.3, for artificial spin ice systems, each magnetic island behaves like a single domain; therefore, the MFM technique provides a qualitative route to probe the magnetic orientation of the magnetisation, which is produced out of the plane. As the MFM probe is an intrusive process, it is possible to affect or reconfigure the magnetic structure of the material surface locally, especially for soft magnetic materials [98; 99]. Therefore, an initial characterisation study is always performed before the experimental procedure. In some cases, a low moment tip has to be employed in order to avoid the tip interaction effect. For the sample studied in this project, due to shape anisotropy, the island's magnetisation is found to be adequately stable when subject to scanning.

## 3.3 Interpretation of microscopy data

### 3.3.1 Interpretation of AFM/MFM image

Due to the high resolution requirement, the whole Penrose pattern images are obtained by scanning four quarters of the sample separately and then the images are stitched together to form a full pattern via image processing software. The pattern structure and magnetic configuration of the array can be mapped from the AFM and MFM images onto the calculated pattern from which the coordinate of each island is precisely given. Figures 3.3(a) and (b) show a portion of AFM and MFM data taken from an  $L = 1000$  nm lattice constant pattern. In order to give sharp contrast, the MFM data is processed via image software Gwyddion. In the MFM image, the north pole and south pole of each element are visible as

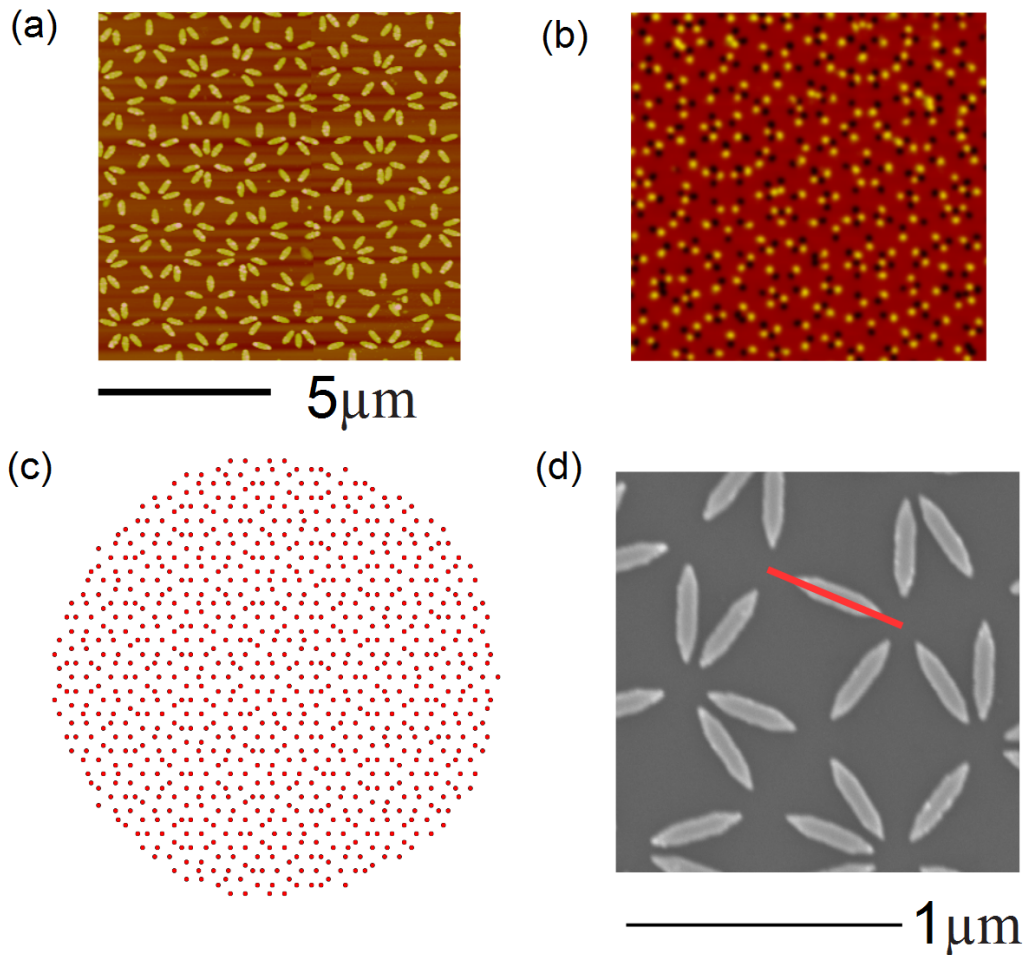


Figure 3.3: (a) and (b) A portion of AFM and MFM image of Penrose tiling with lattice constant  $L = 1000$  nm. (c) A digital image of Penrose tiling pattern, each dot sits in the center of a vertex. (d) A portion of SEM image of Penrose tiling pattern. The lattice constant is defined as the distance between center of one vertex and its neighbouring vertex center (red line).

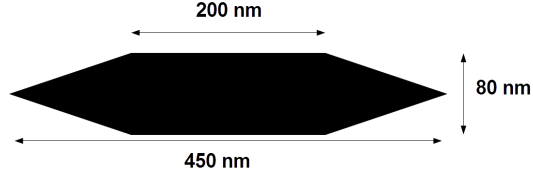


Figure 3.4: The islands were designed to have a shuttle shape. Each island has a lateral size of 450 nm by 80 nm with a thickness of 26 nm.

a black and yellow dot, respectively. Therefore, the elements are confirmed as a single domain. Figure 3.3(c) is a digital image generated via python code. Each dot sits at the center of the vertex and the coordinates for each dot are from the code. Therefore, when this digital pattern is mapped onto the AFM/MFM images, each island position can be precisely figured out. A number of useful parameters therefore can be extracted from AFM/MFM images, such as vertex magnetic charge distribution, net magnetisation, vertex energy distribution, etc. The algorithm of Penrose tiling generation is detailed in Appendix A. Figure 3.3(d) is a portion of SEM image with lattice constant  $L = 600$  nm. The lattice constant  $L$  is defined as the distance from the center of one vertex to its neighbouring vertex center (red line in figure 3.3(d)).

#### 3.3.2 Dipolar energy calculation and net magnetisation calculation

For the sample studied in this thesis, the islands were designed to have a shuttle shape (see figure 3.4). For an island with shape and size shown in figure 3.4, the volume is  $V = 6.67 \times 10^{-22}$  m<sup>3</sup> the magnetisation of permalloy sample is  $M = 8.0 \times 10^5$  A/m. Hence, the magnetic moment of an island is  $m = MV = 5.336 \times 10^{-16}$  Am<sup>2</sup>. For the Penrose tiling, there are seven types of vertex in total (see figure 3.5). For the magnetostatic energy calculation of each type of vertex, we chose the OOMMF micro-magnetic simulation platforms, for which a simulation unit comprising nano-islands is used to form a vertex with the magnetisation orientation set according to different energy configurations [100]. For the simulation, the pattern is treated as 3-D and each object is divided into

### 3.3 Interpretation of microscopy data

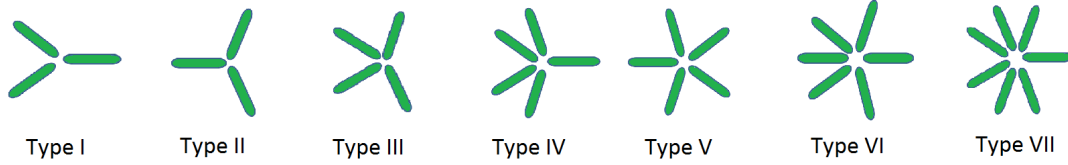


Figure 3.5: The seven different type of vertex in Penrose tiling are shown here.

Table 3.2: The number of possible configuration and energy level for each type of vertex in the Penrose tiling.

Vertex	Possible configuration number	Number of energy level
Type I	8	3
Type II	8	3
Type III	16	6
Type IV	32	10
Type V	32	4
Type VI	64	20
Type VII	128	36

5 nm  $\times$  5 nm  $\times$  5 nm cells. The exchange stiffness of  $1.3 \times 10^{-11}$  J/m, zero crystalline anisotropy and a damping coefficient with 0.5 for Permalloy was used for simulation ( This is an artificially high value of damping, used to ensure fast convergence of the static micromagnetic states). These simulation parameters can be found in [100]. The geometry and size are set as identical to the sample used, and the lattice constant is set to be  $L = 600$  nm. Table 3.2 lists the number of possible vertex configurations and energy level number for each type of vertex. As shown in the table, for type VII vertex, all possible configurations can be grouped into 36 levels with different energies. As the aim of the thesis is to study the low energy states, we will focus on the lowest energy and second lowest energy configurations for each vertex. The possible configurations with corresponding energy for type I vertex is illustrated in figure 3.6. The configurations and corresponding energy for the rest of vertices are listed in Appendix B.



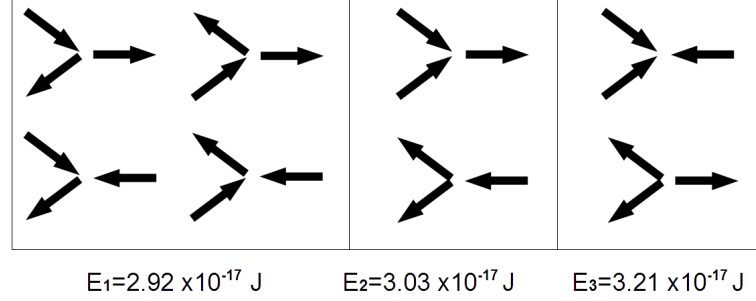


Figure 3.6: All possible configurations and corresponding energies for type I vertex. The energy comes from OOMMF micro-magnetic simulation.

### 3.3.3 Net magnetisation calculation

As mentioned in Chapter 2, when a square pattern is effectively demagnetised, a digital net magnetisation is close to zero and therefore hard to be probe from magnetometer device. Alternatively, the net magnetisation can be obtained from MFM image, i.e. the net magnetic moments in square patterns can be calculated by  $\mathbf{M} = M_X \hat{\mathbf{x}} + M_Y \hat{\mathbf{y}}$ , where  $M_X = \sum m_x$ ,  $m_x = \pm 1$ ,  $m_y = \pm 1$  is the Ising moment along the transverse and perpendicular direction of the array, respectively. These Ising moments values can be directly read from the MFM images. For a Penrose tiling, all the islands aligned in one of five different directions. Therefore, the net magnetisation could be calculated by summing up all the net magnetic moments along these 5 directions.  $M_i = \sum m_i$ , where  $m_i (i = 1, 2, 3, 4, 5) = \pm 1$ , moments along each direction can be decomposed along  $x, y$  direction:  $m_{ix} = m_i \cos \theta_i$ ,  $m_{iy} = m_i \sin \theta_i$  where  $\theta_i = i \times 72^\circ$ . Then the total net magnetic moment is  $M = \sqrt{m_x^2 + m_y^2}$ , where  $m_x = \sum_{i=1,2,3,4,5} m_{ix}$ ,  $m_y = \sum_{i=1,2,3,4,5} m_{iy}$ .

### 3.3.4 Order parameter calculation

Correlation functions have been employed in early studies of square and kagome patterns, and have provided information about frustration [14; 69]. The correlation function can be defined in different ways. For example, in the square artificial spin ice system, a set of pairwise correlations are defined between distinct neighbouring pairs. When the moments of paired elements are in an energetically

### 3.3 Interpretation of microscopy data

---

favourable configuration, the correlation value is 1, otherwise it is -1. Due to frustration, different types of pairwise elements correlate in different ways. Therefore, the effects frustration can be inferred from the correlation calculations. For the ac demagnetisation study, when the net moment of array is zero, the correlation study provides an instructive method to describe the demagnetisation effect. As discussed in [15], the complex ac demagnetisation states can be described by just two types of pair correlations.

For Penrose tiling, in order to discuss the disorder of the states obtained from different protocols, we chose an alternative way to define the order parameter. Rather than calculate the dipolar interactions between different islands, the correlation function is given by the scalar product of the Ising moments in the ground state and measured states:

$$C = \frac{\sum_i S_i \cdot S'_i}{N},$$

where  $S_i$  and  $S'_i$  are the island macro-spin in the same location of the ground state and measured state, respectively.  $N$  is the total number of macro-spins being taken into account. The macro-spin moment is taken as unity. The ground state here refers to a theoretical predicted configuration (details in the following chapter). The spin scalar product is defined to be 1 if the moment of an element from a measured state has the same direction as it would in the ground state, otherwise defined as -1. Therefore, the correlation value can vary from -1 to 1. If the moments in the measured state are all parallel (anti-parallel) to the ground state, the order parameter will be 1 (-1). When this correlation calculation is performed across the whole pattern, i.e. when all the macro-spins are taken into consideration, it was found that the value of correlation is particularly small, which implied that no large scale ground state emerged. Therefore, a modified correlation function was employed. Instead of summing up the product of a spin with its counterpart in the ground state  $S_i \cdot S'_i$  for all the spins, the modified definition is summing up the  $S_i \cdot S'_i$  for a group of spins surrounding it  $C_i = \sum_n S_i \cdot S'_i$  first, where  $n$  represents  $n^{\text{th}}$  nearest neighbour spins of spin  $S$ . Then average all the correlation  $C_i$  for all the spin in the pattern. The correlation is given by

$$C_n = \frac{\sum_i |\sum_n S_i \cdot S'_i|}{\sum_i \sum_n 1}. \quad (3.1)$$

### 3.4 The AC demagnetisation and thermal annealing detail

---

The absolute value operation is used to prevent the correlation value with different signs cancelling out. In this modified definition, the correlation between a spin and its counterpart in the ground state is weighted by its neighbouring spins; therefore, the correlation is expected to decay when further neighbouring spins are considered. As the states from our experiment are identified to be locally ordered only, this correlation calculation will give an estimate of correlated region size. The correlation calculation result will be discussed in Chapter 6.

## 3.4 The AC demagnetisation and thermal annealing detail

### 3.4.1 The detail of AC demagnetisation

The ac demagnetisation protocol we chose was a rotating linearly-ramped applied field rather than oscillating magnitude of field protocol. The linear demagnetisation protocol has been proved to be as effective as the oscillation demagnetisation protocol [62]. An in-plane magnetic field was applied starting from 2000 Oe while decreasing linearly with a ramping rate 10 Oe/s until it reached zero. In the mean time, the sample was rotating around an axis normal to the sample plane with a frequency  $f = 20$  Hz. After demagnetisation, the remanent magnetic moments orientation were imaged by MFM.

### 3.4.2 The detail of thermal annealing

Silicon substrates coated with 200 nm LPCVD nitride were used for thermal annealing. The thermal annealing experiment was carried out in the MBE (Molecular Beam Epitaxy) chamber where the high vacuum and low stray field conditions can satisfied. The vacuum of MBE system in Leeds University is  $10^{-10}$  mbar. The thermal annealing protocol is the same as protocol used in [69]. The sample was first heated up to 545 °C at a rate of 20 °C per minute and then maintained at this temperature for 15 minutes. The sample was then cooled down to 445 °C at a rate of 1 °C per minute. Following this step, the sample was cooled down

### **3.4 The AC demagnetisation and thermal annealing detail**

to room temperature naturally ( $\approx 10$  °C per minute). When the sample cooled down to room temperature, the magnetic structure was then imaged by MFM.

# Chapter 4

## Ground state of the Penrose tiling

### 4.1 Introduction

In this chapter, the macroscopic ground state of Penrose tiling will be illustrated. Before we discuss the Penrose tiling, it is worth comparing the ground state of real spin ice, artificial square ice and artificial kagome ice system. For the real spin ice system, the spins are disordered when the local configuration obeys the rule that two spins point inwards and two spins outwards in a basic tetrahedron. The number of possible configurations for the ground state of a single tetrahedron of spins are  $C_4^2 = 6$  when all the spins follow the “ice-rules” (see figure 2.1). These local “ice-rules” cannot guarantee a long-range order; therefore, a real spin ice system is disordered at any temperature and displays a low temperature entropy. For the square artificial spin ice, the 2-D geometry results in energy differences between states obeying the “ice-rules”. In this case, the lowest energy state of a single vertex only has two fold degeneracy. As this condition propagates from one vertex up to the whole system, only two states can satisfy this rule, i.e. it results in a ground state with long-range order (see figure 2.7), which has been confirmed by thermal annealing experiments [69].

For the kagome artificial system, the three elements in a vertex are equivalent to each other, so that the “ice-rules” becomes “two in one out” or vice versa. Unlike the “ice-rules” in a square pattern, this rule results in a ground state of

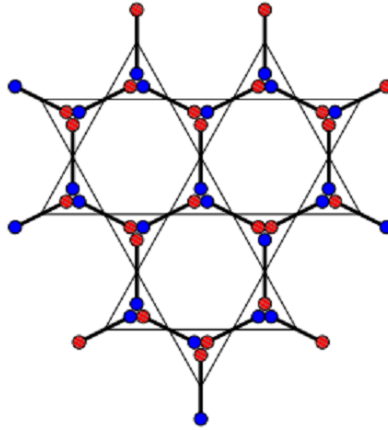


Figure 4.1: The charge ordered state of the kagome pattern. All the vertices obey the “ice-rules”, i.e. the magnetic charge of each vertex is  $\pm 1$ . The charge distribution in this configuration is ordered to reduce the total energy. The adjacent triangles carry charges with opposite sign. After Chern et al. [52]

a vertex with six-fold degeneracy, therefore can be satisfied by a macroscopically large number of micro-states. In other words, the rule cannot lead to a long-range order. When all the vertices in the system follow these “ice-rules”, the magnetic charge of each vertex is  $\pm 1$ , the kagome pattern is in a low energy state. The total energy can be further minimised by considering the further neighbour interactions of elements. For example, when a kagome pattern is described by a dumbbell model (each element is treated as an object consisting of two magnetic charges with opposite sign), when the adjacent magnetic charge interactions are minimised, the system enters a state called “charge ordered state” [52]. The charge ordered state is supposed to have lower energy as well as longer order (see figure 4.1).

For the Penrose tiling pattern, a similar idea is used to construct the ground state. First, in order to get a low energy state of the whole system, each vertex energy is minimised. There should exist similar “ice-rules” to keep the vertex in the lowest energy configuration. Second, if these rules give a long-range order, then the system’s lowest energy configuration can be obtained by tiling all the vertices in a low energy state compatibly. If these rules do not give a long-range

order, i.e. the state can be satisfied by a large number of configurations, then the further neighbour interactions need to be considered to reduce the total energy of the system. It was found that unlike the square and kagome pattern, there is no unique “ice-rules” for putting each vertex in a low energy state. As for the Penrose tiling, there are seven different types of vertex and for each vertex, the “ice-rules” is different. Carefully tiling each vertex in a low energy state leads to a low energy configuration of the Penrose tiling pattern. As illustrated below, this configuration consists of two parts: one has long-range order, which has only two-fold degeneracy, while the other part can be satisfied by a number of configurations.

## 4.2 Ground state of the Penrose tiling

### 4.2.1 Vertex energy configuration

As discussed above, the first step towards solving the problem of the ground state of a system would be finding the ground state configuration of each vertex. For Penrose tiling, there are seven types of vertex, as listed in figure 3.5. The configuration of the two lowest vertex energies for each vertex is listed in figure 4.2. At first glance, the lowest energy configurations of each vertex follow similar alignment to the square pattern and kagome pattern. The macro-spins of each vertex point in and out alternately to minimise the total energy. This alignment can be termed as generic “ice-rules”. Besides, each vertex has different degeneracy, which implies that when these vertices are tiled together to form a whole pattern, the ones that have two-fold degeneracy may lead to a long-range order, while the other vertices may lead to states with more than two fold degeneracy. Due to the geometry of some vertices, the Ising-like moments in these vertices can point to either of the two directions without altering the total energy of the vertex, as represented by red double-arrow in figure 4.2. However, as each element is shared by two vertices, when both vertices that share the element are taken into consideration, the elements moments direction may not be flexible any more. All these situations will be displayed below.

## 4.2 Ground state of the Penrose tiling

Vertex type	Energy level 1	Degeneracy	Energy level 2	Degeneracy	Energy difference between level 1 and 2 (normalized)
1		4		2	4.568
2		2		4	1.885
3		2		2	9.141
4		4		2	3.477
5		10		10	18.27
6		2		4	15.93
7		2		4	1.00

Figure 4.2: Schematic showing the low energy configuration of seven types of vertex (only lowest and second lowest energy configuration are listed). The energy difference between level one and two has been normalised by the one of vertex VII. The double-headed arrows represent the Ising-like moment of the island that could point to either of the two directions without changing the total energy of vertex. The energy calculation is based on the OOMMF micromagnetic simulation.



### 4.2.2 Ground state of two decagons

As the lowest energy configuration of each type of vertex has been obtained, we need to tile these low energy vertices to form a Penrose tiling pattern. If these vertices are compatible with each other, we can get a low energy configuration of the whole pattern. For Penrose tiling, due to its non-periodicity, one has to tile these vertices one by one manually to form a Penrose tiling pattern. This is like playing a tiling game and for the pattern we studied, which contains 1650 islands, it is a nontrivial problem. Fortunately, the Penrose tiling pattern can be decomposed into two different decagon units, each of which contains several vertices (see figure 4.3). If we could find the low energy configuration of these decagons by tiling the vertices one by one, then the whole Penrose tiling can be tiled by these larger units rather than seven different vertices, which significantly reduces the amount of work. The construction details are given below. As a first step, ground state constructions for the two types of decagon will be illustrated one by one. These constructions are largely based on the vertex configuration list of figure 4.2. Finally, the decagons are joined into the larger pattern.

#### GS of type A decagon

If one starts constructing the type A decagon (as listed in figure 4.3) from any single island and follows the vertex ground state configurations listed in figure 4.2, it can be easily found that the vertices inside the decagon are compatible with each other. An example of this process is shown in figure 4.4. The whole pattern configuration can be easily inferred from a single island alignment. This is because most of the vertices in this decagon have only two fold degeneracy. When these vertices are connected together, the degeneracy is lifted. Therefore, the configuration in the type A decagon forms order across the whole decagon, in such a way that when this type of decagon is connected with other decagons, the order is connected together and crosses the whole pattern eventually. The single island degeneracy in the type V vertex is preserved in this decagon, which is marked in red in figure 4.4. The islands along the decagon edge are shared with other vertices; therefore, their states need to be confirmed in the neighbouring decagon configurations. This will be discussed below.

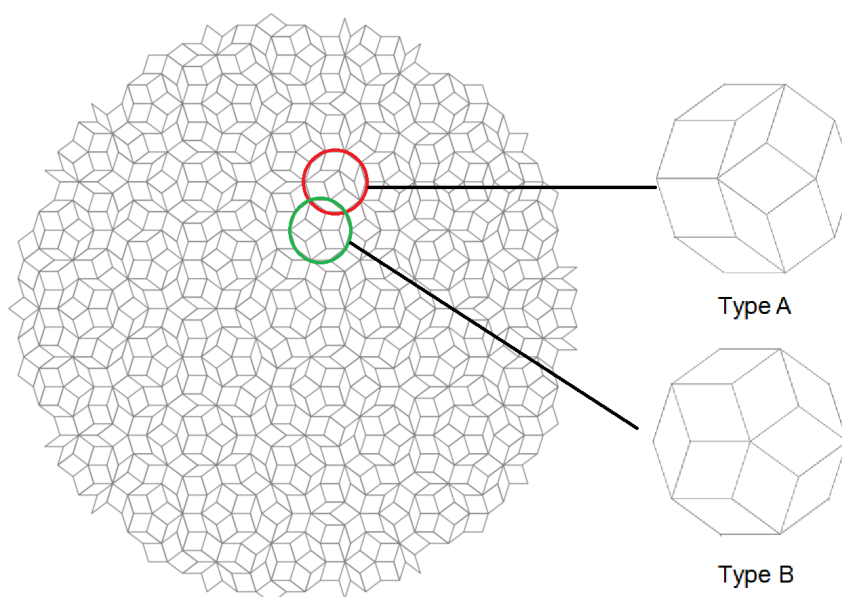


Figure 4.3: The Penrose tiling can be decomposed into two types of decagons, highlighted by the red circle (type A decagon) and green circle (type B decagon).

### GS of type B decagon

The type B decagon has five-fold symmetry; therefore, the whole decagon can be divided equally into five parts. For any one part, if we follow the same strategy outlined above, we will find immediately that not all elements can be satisfied at the same time. The three possible low energy configurations of this part are listed in figure 4.5 (a), (b) and (c). In these three configurations, the type II vertex and a pairwise element along the edge cannot be in a low energy state at the same time. In order to tile these vertices together, a pair of elements has to be configured to a higher energy state, as represented by red arrows in figure 4.5 (a), (b) and (c) respectively. The double arrow represents how the element moment can point to either of the two directions without costing extra energy. The energy difference between these configurations is listed in figure 4.5 (d). The configuration in figure 4.5 (a) has lower energy than other two. The other four parts have the same low energy configuration as this one due to the same geometry. The joint elements between these five parts can be arranged into

## 4.2 Ground state of the Penrose tiling

---

low energy configurations by aligning the five parts in a proper order. The final configuration is illustrated in figure 4.5 (e). The vertex in the center (type V vertex) can be easily tiled into a low energy state by following the generic “ice-rules” of one in, one out, alternately. The double arrows disappear, because the constraints of the “ice-rules” lift the degeneracy. However, the low energy state of the type V vertex has ten-fold degeneracy as listed in table 4.2; therefore, the low energy state configuration of the type B decagon has ten-fold degeneracy.

### When two decagons overlap

The low energy states of two types of decagon have been obtained. Next, these decagons need be tiled one by one manually to form a Penrose tiling. During this process, when two decagons meet, the element’s alignment in the joined area has to be considered. There three cases to be consider are:

1. When type A and type B decagons overlap, both decagons can be in a low energy state compatibly, as shown in figure 4.6(a).

2. When two type A decagons overlap, there will be two type II vertices whose energy cost when lifting to another energy level is smaller than other vertices in this structure, as represented by the black dot and red dot in figure 4.6(b). However, the low energy configuration of these two vertices is frustrated. It can be solved by lifting either of them to another energy level, which will let another vertex stay in one of the two degenerated low energy configurations (yellow vertex).

3. When two type A decagons and a type B decagons join together, there will be four type II vertices that become frustrated. This can be solved by lifting two of them to another level, leading the type VII vertex (red arrows) to be able to occupy its ground state. These two type II vertices that stay at a higher energy level are marked by red dots in figure 4.6(c).

### 4.2.3 The ground state of the whole pattern and its character

When considering all of the above, the whole pattern can be tiled decagon by decagon. The final low energy state is shown in figure 4.7. From the point of

## 4.2 Ground state of the Penrose tiling

---

view of order, a large numbers of elements are “chained” together, similar to the square pattern. The macro-spins in this part have only two fold degeneracy and this order crosses the whole pattern, making it possible for the long-range order to arise in Penrose tiling. This part is therefore termed the “skeleton” part (see the black part of the figure 4.7). On the other hand, there is another type of element, which is not “chained” to the macro-spins in the skeleton part. These elements include type V, VI and VII vertices. For a type V vertex, it can stay at one of its ten degenerate configurations without changing the total energy of the pattern, while for type VI and VII vertices, it can stay at any one of two degenerate configurations. The elements in these vertices seems to be flippable, and therefore this part is termed the “flippable” part (see figure 4.7, red part).

Due to the properties of the aperiodic structure, the whole pattern configuration is constructed almost manually. As illustrated in figure 4.2, part of the type II vertices have to stay at the second energy level due to frustration. This frustration arises from the topology of the Penrose tiling pattern, therefore, is a kind of “topologically induced emergent frustration”. A similar frustration has been found in another type of artificial spin ice system with different geometry [101] where part of the vertices have to stay at higher energy states. In similar way, the configuration for the whole Penrose tiling pattern accommodates most vertices at low energy states and we refer to this state as the ground state of the Penrose tiling. As will be illustrated below, several samples, when put through an energy minimisation protocol, do show a trend towards this low energy configuration.

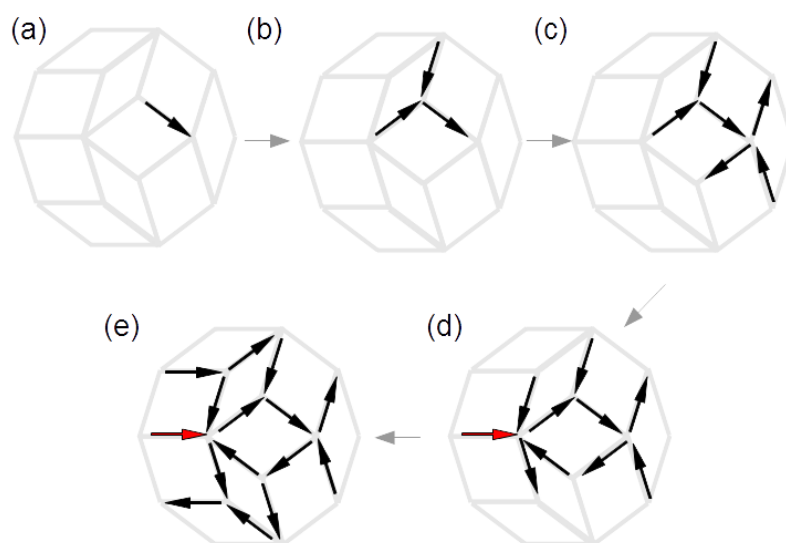


Figure 4.4: Type A decagon ground state construction process: (a) Assuming a single element magnetic moment direction is given, (b) then the favourite magnetic moment directions of the neighbour islands can be inferred from figure 4.2. (c) and (d) more island's magnetic moment directions can be inferred from the configuration in figure 4.2. The red arrow denotes that the moment can flip without costing extra energy, preserving the type V vertex degeneracy at the decagon level. (e) The spin direction of the remaining islands inside the decagon can be worked out following similar rules.

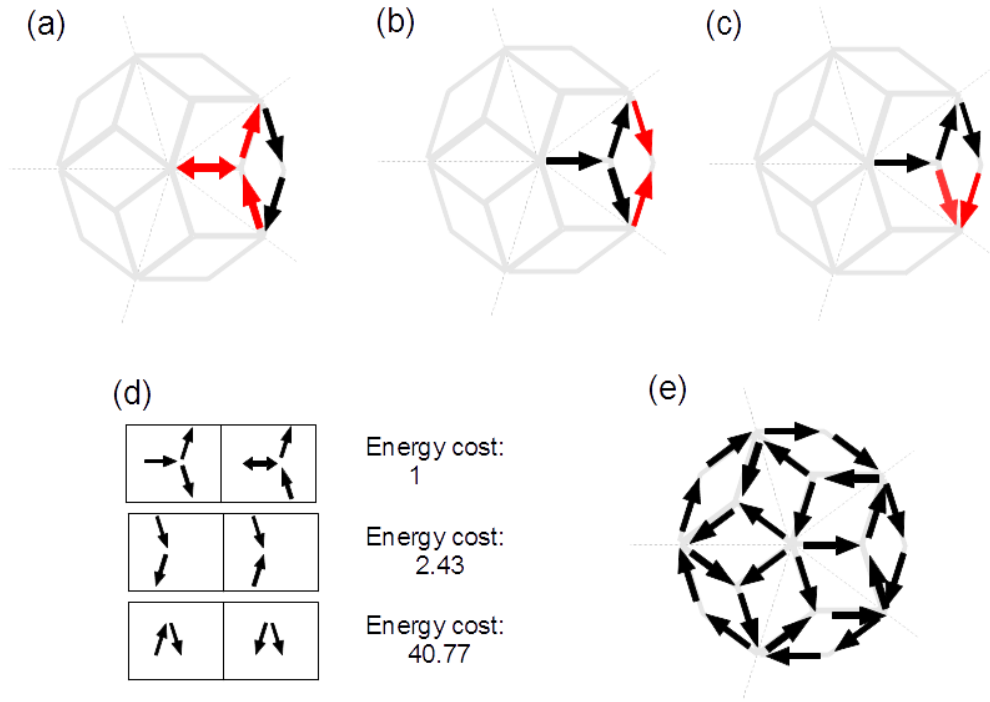


Figure 4.5: Type B decagon ground state construction: the type B decagon can be divided into five equal portions (dashed line). Three possible low energy configurations for one portion are listed in (a), (b) and (c). The double arrow represents how the element moment can point to any direction without costing extra energy. For a portion, the type II vertex and a pairwise element cannot stay in a low energy configuration at the same time. The higher energy state is represented by red arrows. The energy difference between the low energy state and higher energy state is listed in (d) (normalised by energy difference of a type II vertex). Therefore, (a) has lower energy than (b) and (c). The final configuration of decagon B is drawn in (e).

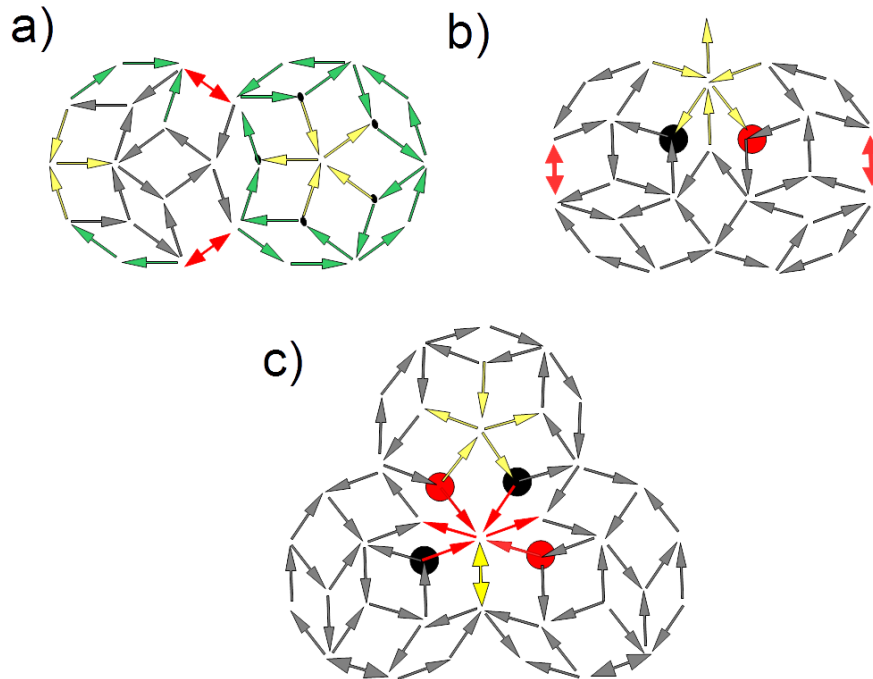


Figure 4.6: Three cases of two joined decagons: (a) Type A and type B decagons joined together, where both decagons can stay in their lowest energy state compatibly. (b) When two decagons overlap, there are two type II vertices that cannot be in their low energy states compatibly, which is represented by black and red dots, respectively. One of these two vertices has to be lifted to a higher level, which results in another vertex staying at one of its two degenerate state (yellow arrows). (c) Two types of decagon A and a type B decagon joined together. The four type II vertices are not compatible, which leads to two of them lifting their energy configuration level (red dots).

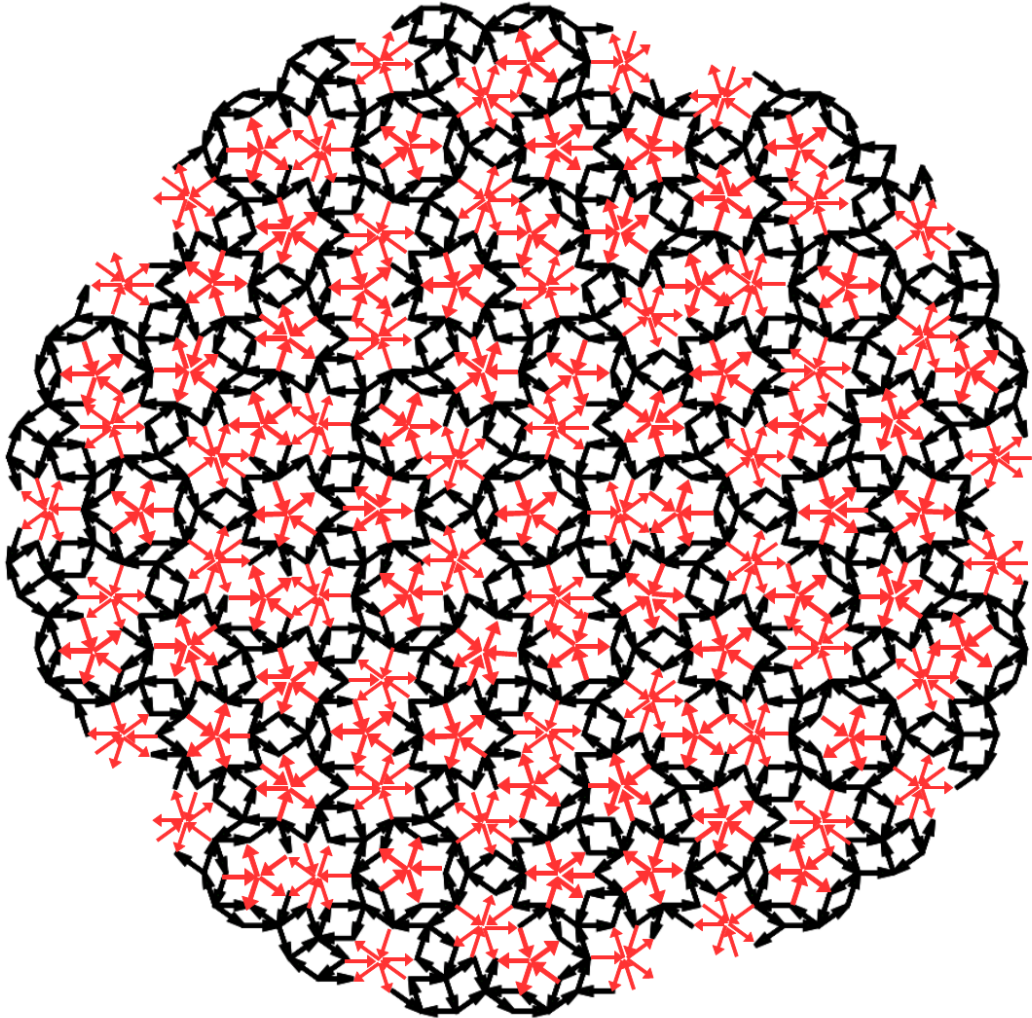


Figure 4.7: The ground state of the whole pattern consists of two parts. The skeleton part (black arrows) consists of type I, II, III, IV vertices. The magnetic moments build long-range order across the whole pattern, which has two-fold degeneracy. The flippable part (red arrows) consist of type V, VI and VII vertices. Each vertex can stay at one of its several degenerate states without altering the total energy of the pattern (for a type V vertex, the degeneracy is ten, for a type VI and VII vertex, the degeneracy is two).



# Chapter 5

## Statistical results of rhombus, and colour maps

### 5.1 Introduction

As discussed above, a predicted low energy state of Penrose tiling is obtained manually, which contain two parts, the skeleton part and the flippable part. The skeleton part has two-fold degeneracy, similar to the ground state of square pattern, the long range order is more possible to arise in this part than the flippable part. As the Penrose tiling is a quasi-periodic pattern, the long range order here refers to a group of magnetic elements that, in principle, show finite correlations up to any arbitrary distance. It will be demonstrated below from the rhombus population analysis that the sample after thermal annealing “looks” more close to the predicted ground state than the other states such as the as-grown state or the ac demagnetised state. Nevertheless, a further analysis based on a colour mapping method reveals that no long-range order arises either in the thermally annealed state or in the other states.

## 5.2 Different Rhombus configuration distribution

### 5.2.1 Different types of rhombus configurations and corresponding populations in each state

In this chapter, the Penrose tiling is analysed in terms of rhombuses rather than vertices. In Penrose tiling, there are two types of rhombuses, which are termed as “thick” and “thin” rhombuses. As shown in figure 5.1, the configurations of rhombuses can be grouped into four types regardless of the shape discrepancy of “thick” and “thin”. The first type of rhombus, for which the magnetic moments form a loop, has the lowest magnetostatic energy amongst the four types of rhombuses. Therefore, in the predicted ground state, most rhombuses stay in this configuration. The second type rhombus possess polarisation, therefore can be easily found in polarised state. For the third rhombus, the configuration can be obtained by reversing one element from the first type rhombus. This configuration has higher energy than the first type rhombus. Due to its high configuration degeneracy, this type of rhombus has a large population in the random aligned state. For the fourth rhombus, all adjacent element pairs are aligned “head to head” or “tail to tail”. These types of pairwise elements are energy unfavourable, and therefore possess the highest energy compared to other types of vertices. Consequently, this type of vertex does not emerge in the predicted state and also is very rarely observed in experiment. These four types of rhombus configuration populations from the sample in different states are plotted in figure 5.1. Compared with the as-grown state and ac demagnetised state, the ratio of different configurations in the thermally annealed state is found to be very close to the predicted ground state. However, it cannot guarantee a long-range order arising in the thermally annealed state. In order to verify the long-range order, we use a colour mapping method that maps different coloured rhombuses on to the different rhombus configurations.

## 5.2 Different Rhombus configuration distribution

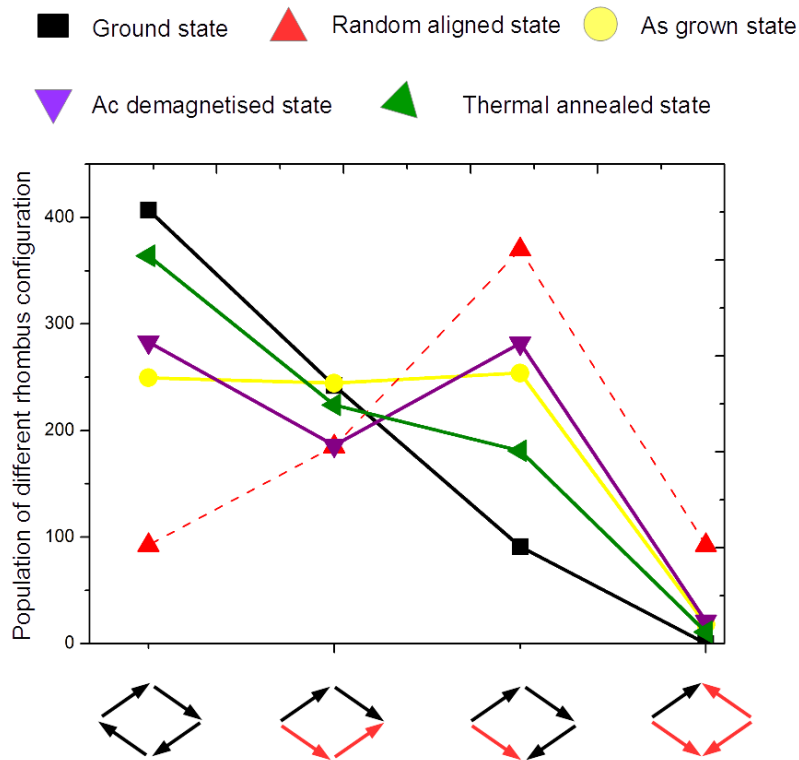


Figure 5.1: The population of rhombus moments configurations in different states: Below, the abscissa represents the four types of rhombuses with different moment configurations. The red arrows indicate the different moments respect to the first rhombus configuration. The four rhombus population ratios in the thermally annealed state are much closer to the ground state than the other ones. All the data are from four patterns with 600 nm lattice spacing.

## 5.2 Different Rhombus configuration distribution

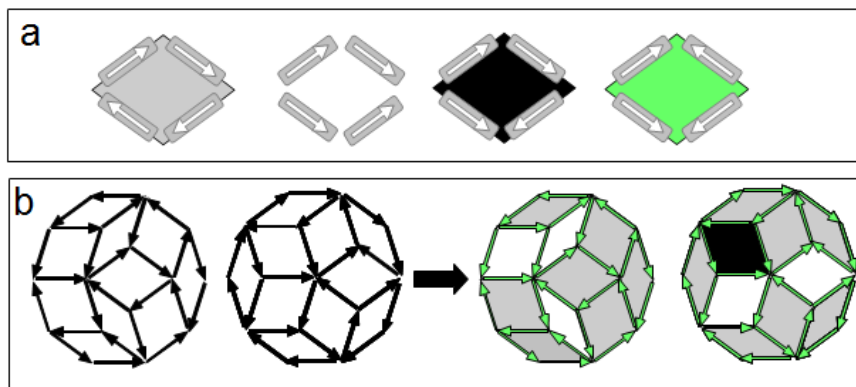


Figure 5.2: Coloured magnetic configuration: (a) The rhombus moments are mapped in different colors based on the configuration. (b) Two types of decagons in the ground state after colour mapping. The green rhombus with the highest energy configuration does not arise in any low energy decagon configuration.

### 5.2.2 Colour mapped MFM images analysis

As shown in figure 5.2(a), different rhombus configurations can be represented by different colours. In the predicted ground state, the two types of decagon configurations after colour mapping are shown in 5.2(b). Due to the symmetry of decagon configuration, other energy degenerate decagon configurations can be obtained via simple operations (by rotation or horizontal flip). The coloured decagons when mapped onto structure with moment direction can be used to identify possible correlate elements in a decagon scale. If any ground state order with “domain” scale larger than a decagon arise, a coloured low energy decagon should be found from the colour mapped MFM images. Here, the term “domain” should be used with great caution: as in quasi-periodic pattern, magnetic domains have not been defined before. Here we use it to define a group of macro-spins that have a kind of correlation.

As an example, a MFM images of a sample in a state prepared by thermal annealing 5.3 is mapped by coloured rhombuses and the result is listed in figure 5.4. At first glance, it is hard to identify which decagons are in the low energy state. This problem can be easily solved by considering the feature of coloured decagons in ground states. Firstly, no green rhombus emerges in any coloured

## 5.2 Different Rhombus configuration distribution

---

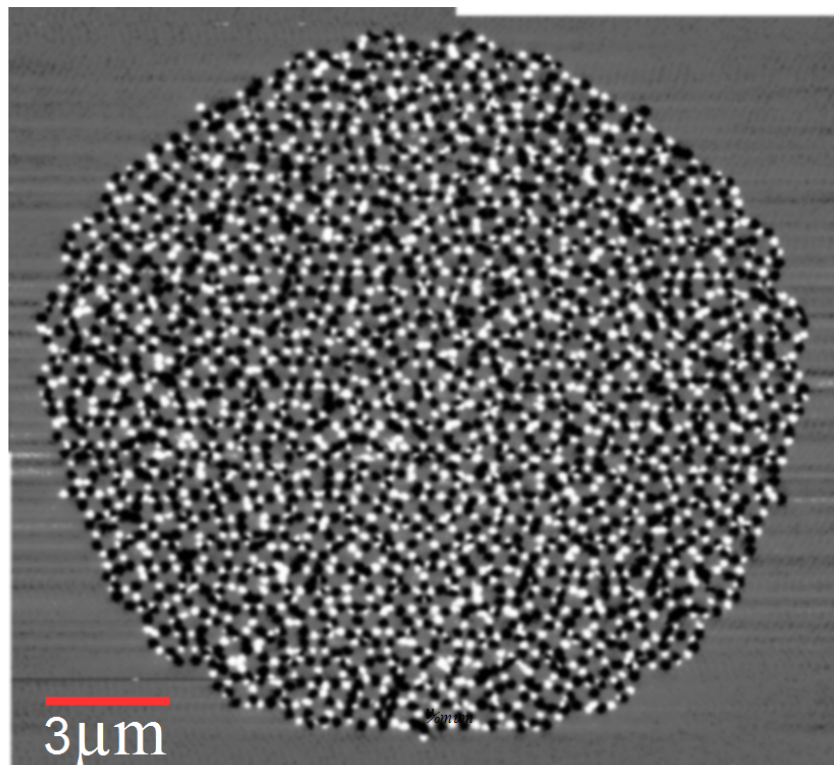


Figure 5.3: A MFM image of a sample in a state prepared by thermal annealing, the lattice constant is 600 nm.

## 5.2 Different Rhombus configuration distribution

---

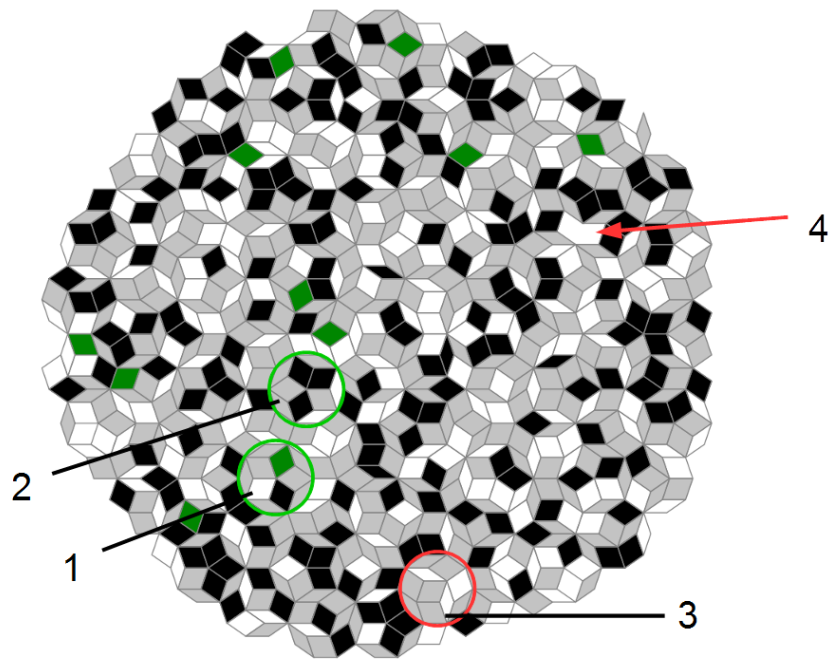


Figure 5.4: Coloured MFM image from the sample after thermal annealing (600 nm lattice space). The rhombus colour is based on its magnetic configuration from figure 5.2. The type B decagon in location 1 is not in a low energy state due to a green rhombus arising. Its neighbour, a type B decagon in location 2 can be excluded from low energy state because a paired black rhombus exists. The type A decagon in location 3 (red circle) is in a low energy state. Lost lines (as an example, a lost line is marked by line 4) are partly due to being physically lost and partly due to the low resolution of the MFM image.

## 5.2 Different Rhombus configuration distribution

---

low energy decagon configuration. Any coloured decagon from the coloured MFM images can be excluded from a low energy configuration if containing a green rhombus. An example is illustrated in figure 5.4, location 1. Secondly, all the type B decagons are disconnected to each other in a Penrose tiling. Therefore, the black rhombuses that only arises in type B decagon low energy state are not connected to each other when the whole pattern is in low energy state. If any black rhombuses are found to be paired together or more than one black rhombus are found in a decagon, it can be inferred that the decagon is not in a low energy state. An example is given in 5.4, location 2. Following the features of coloured decagon in low energy state, it can be easily verified that most of the decagons in coloured MFM images are not in a low energy state, as most of the black rhombuses are paired together and green rhombuses arise. We did find some low energy type A decagon along the boundary of the sample with small lattice constant (see figure 5.4 location 3). This may be due to the frustration being weak along the edge, which results in a low energy state of the decagon. This kind of low energy decagon is also found from the edge of other patterns with 700 nm lattice constant in an as-grown state.

### 5.2.3 Conclusion

The small lattice spacing and thus strong dipolar interactions between islands result in stronger correlations in an artificial system. Hence, for a square pattern, long-range order are more easily found in samples with the small lattice space [69]. For Penrose tiling pattern, a similar result is expected. The long-range ordered ground state however is not easily identified from the magnetic moments configuration. Hence, a colour mapping method is employed. From the colour mapped MFM images, few large GS “domain” emerge from samples with the smallest lattice constant (600 nm). As will be shown later, this is partly because the samples, even after thermal annealing, have not approached the predicted ground state, and partly because one type of vertex (type VII vertex) prefers to stay at the second lowest energy configuration rather than the lowest one after thermal annealing. This type of vertex sits right at the joined part between decagon A and decagon B, which changes both of the decagon configurations.

## **5.2 Different Rhombus configuration distribution**

---

On the other hand, how far these states are from the predicted ground state is not easy to infer from rhombus population and colour mapped MFM images. In order to obtain such information, an order parameter will be employed in the following chapter.



# Chapter 6

## Domain size estimate

### 6.1 Introduction

A correlation function is often used in statistical mechanical systems. For example, in a 2-D Ising model (the spins in the system can only pointing up or pointing down and the values can only be 1 or -1), consider the alignment of two Ising spins  $S(x)$  and  $S(x+r)$  separated by a distance  $r$  in the system. If the separation of the two spins  $r$  is much larger than a typical domain size  $L$ , their average product

$$C(r) = \langle S(x)S(x+r) \rangle$$

will be near zero as the spins have 50 % chance to align or misalign. If  $r$  is much smaller than a typical domain size  $L$ , the spins are aligned parallel to one another. The averaged product of the spins will be one. Hence the averaged domain size of the system can be extracted from a correlation function as the length scale on which correlations die away. Moreover, when the system experiences a phase transition, the domain size will vary from one phase to another, and the correlation function can provide information about the phase transition. When the correlation function is used in an artificial spin ice system, similar information can be extracted from the correlation between islands, such as “domain” size.

As discussed earlier, the thermal annealing protocol has been confirmed to be more effective in energy minimisation than in the other protocols. When it was implemented on a square pattern with a small lattice constant, ground state

ordering was achieved [69]. It was observed that when the sample lattice space increased, the ground state domain size started to reduce, which was qualitatively confirmed by examining the MFM images. When these phenomena were investigated by a correlation function, a trend was clearly revealed by the magnitude of correlation decay behaviour as a function of lattice separation. The radius of average domain sizes can be estimated from the correlation decay behaviour (see figure 6.1).

## 6.2 Skeleton-part correlation function

For a Penrose tiling, we have shown that the symmetry can lead to the emergence of long-range ordered ground state in the skeleton part. However, due to fabrication limitations, the lattice constant can only be reduced to 600 nm before the islands touch each other. This constraint makes the ground state ordering in Penrose tiling difficult to access for the samples used for this project. A correlation function is introduced to discuss the disordering of arrays in a wide range of lattice spacing (600 nm to 1000 nm). The correlation function has been defined in Chapter 3 by equation 3.1. As discussed there, the correlation between the ground state and the other states for each spin is weighted by its “neighbouring spins’ correlation”.

For Penrose tiling, each island sits on one of the edges of a non-periodic pattern, in which the number of nearest neighbour of each island varies from site to site. Therefore, the distance to a neighbouring island is not defined in real space, but in terms of hop steps, i.e. the  $n$ th nearest neighbours are defined as the islands that need  $n$  hops from the reference island, as illustrated in figure 6.2(a). As long-range order is expected to arise only in skeleton part (as discussed in Chapter 4), the spins we are concerned with are those in the skeleton part only. Figure 6.2 gives the correlation function between the ground state and three states from the sample with 600 nm lattice spacing. The difference is easily visible; the thermally annealed states are more ordered than the other two states. The difference between the as-grown and the ac demagnetised state is small compared with the thermally annealed state, which indicates that demagnetisation does not increase the order as much as the thermal annealing protocol. A similar

## 6.2 Skeleton-part correlation function

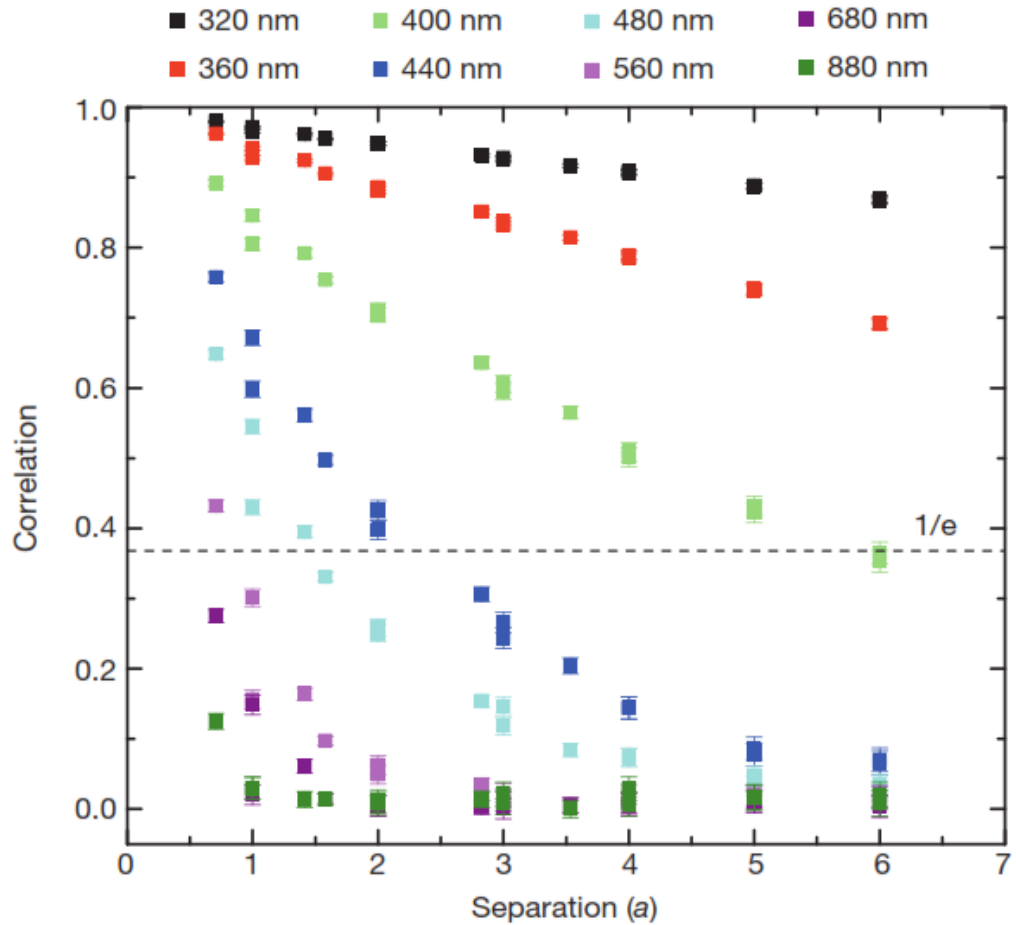


Figure 6.1: Magnitude of correlation as a function of lattice spacing for annealed square artificial spin ice: different curves correspond to different lattice constants. The colour mark is illustrated at the top. The intersection of a horizontal dash line  $1/e$  with each curve gives an estimate of the averaged domain size. After Zhang et al. [69]

## 6.2 Skeleton-part correlation function

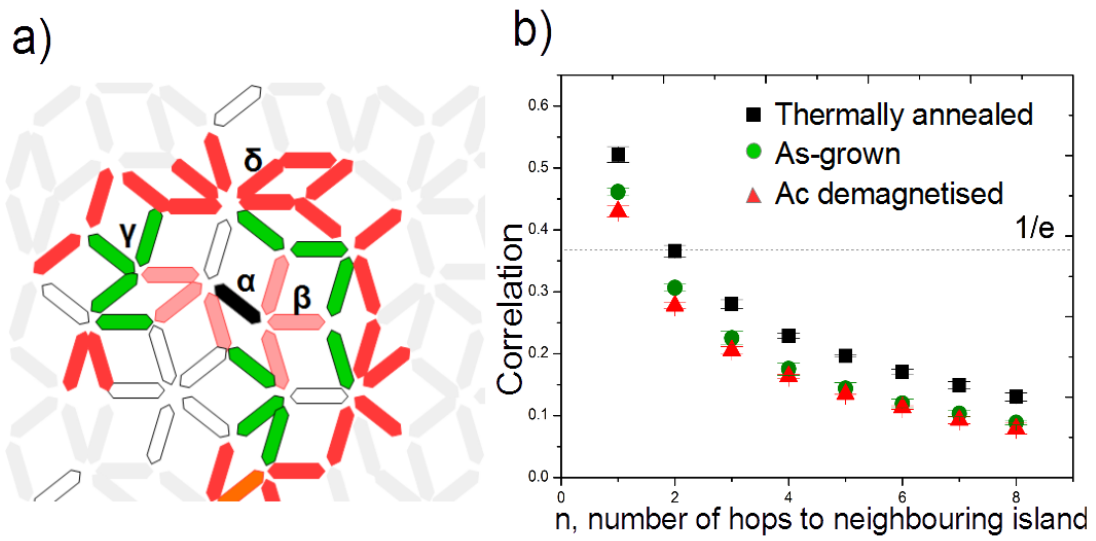


Figure 6.2: Correlation between different states and the ground state: for correlation calculation, each spin's neighbouring islands correlation is taken into account. The three nearest neighbours of a island are sketched in (a). The neighbour definition is explained in the text. The white islands do not belong to the skeleton part and hence are excluded from the analysis. The correlation between the ground state and other states as a function of neighbour island distances are plotted in (b). The correlation function calculation is based on equation 3.1. The lattice spacing of the arrays is 600 nm.

method from a square pattern is used to estimate the domain size of states in Penrose tiling. As shown in figure 6.2, the interception of a line  $1/e$  with each correlation curve gives an estimation of the domain sizes. The estimation of domains sizes therefore is less than two neighbouring islands for the as-grown and ac demagnetisation state and beyond two neighbouring islands for the thermally annealed state. It needs to be pointed out that the islands we considered are from the skeleton part only. The correlation in the flippable part is difficult to calculate since the configuration has more than two-fold degeneracy.

## 6.3 Domain in Penrose tiling pattern

Next, we will demonstrate that the domains in the skeleton part can be visualised by colour mapping the magnetic configuration of each state. This method turns out to be equivalent to the correlation function discussed above. Instead of assigning a value of  $\pm 1$  to the correlation  $\mathbf{S}_i \cdot \mathbf{S}'_i$ , the islands are assigned different colours depending on the correlation with the ground state skeleton part. If an island from a state has the same direction to its counterpart in the ground state, i.e. if  $\mathbf{S}_i \cdot \mathbf{S}'_i = 1$ , this island is coloured blue, otherwise, it will be coloured red, which corresponds to  $\mathbf{S}_i \cdot \mathbf{S}'_i = -1$ , where  $S_i$  is the normalised spin from the state,  $S'_i$  is the normalised spin from same location in the ground state. The spin configurations from any state after colour mapping will consist of two types of coloured spin; one is “blue” spin, which has the same moment direction with its counterpart in the ground state while the other is “red” spin, which has opposite moment direction with its counterpart in the ground state. Two examples are illustrated in figure 6.3. In figure 6.3(a), the spin configuration of a sample in the as-grown state with 1000 nm lattice space is mapped by two different colours. The red spin and blue spin are mixed together, and therefore no “domain” is formed in this state, which are consistent with the previous correlation calculation. In contrast to this, the spin configuration from the sample with 600 nm lattice space after thermal annealing clearly shows different coloured “domains” (as shown in figure 6.3(b)). In order to characterise these domains, an averaged domain size is employed, which is given by the whole area of the sample divided by the sum of perimeter of all the domains in the pattern  $L = A / \sum_i s_i$ , where  $A$  is the area

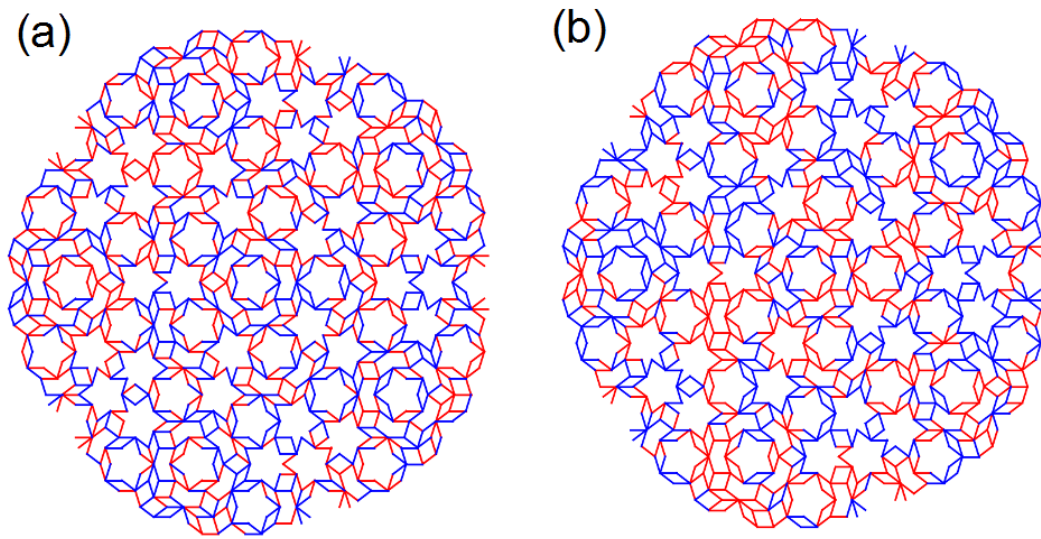


Figure 6.3: Colour mapping of magnetic configuration of the two states: (a) Sample in the as-grown state with 1000 nm lattice constant; (b) Sample with 600 nm lattice constant after thermal annealing. The moments colour depends on the correlation with the ground state. If the island moment has the same direction to its counterpart in the ground state, it will be coloured blue, otherwise, it will be coloured red. The magnetic configurations are extracted from MFM images of the samples.

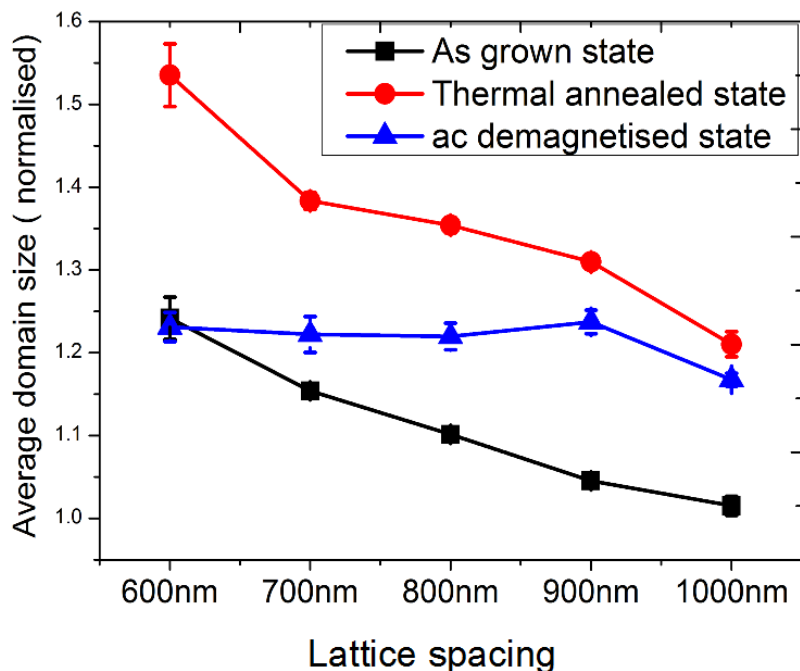


Figure 6.4: The average domain size from samples in different states as a function of lattice spacing: The average domain size is calculated based on the equation given in the text. Each dot is an averaged value from the MFM images taken from three different samples. The error bar is the standard error of these three measures.

of whole skeleton part, and  $s_i$  denotes a domain's perimeter. The summation is over all the domains in the skeleton part. Since the pattern consists of islands, the total area is constant. The boundary separating two different coloured domains refers to the vertices, which consist of blue and red spins. Therefore, the perimeter here is estimated by the number of vertices that consist of red spin and blue spin. When more domains are formed in a pattern with a constant area, the domains becomes smaller and the total perimeter of all the domains becomes larger. Therefore, it is a reasonable parameter to estimate the domain size. The estimated domain sizes from different samples in different states are illustrated in figure 6.4. For the as-grown state and the thermally annealed state, the domain sizes clearly show a decreasing trend when the lattice spacing increases. As these

two states are remanent states after the thermalisation process, the domain size variation for both states therefore has a similar trend. As the thermally annealed state is fully thermalised compared with the as-grown state, it is not a surprise that the average domain is larger.

For the ac demagnetised state, the domain size of samples with lattice spacing from 600 nm to 900 nm is nearly constant. A similar phenomenon was found in the case of hexagonal array ac demagnetisation, where the effective temperature  $1/\beta_e$ , which is used to characterise the ac demagnetisation, is found to be independent with the lattice spacing [39]. For Penrose tilings, due to multiple types of vertices as well as the multiple vertex energies, the effective thermodynamic descriptions has not been employed to investigate the ac demagnetisation; however, the domain sizes that reflect the ordering of the pattern should also be valid for the ac demagnetisation description. It implies that the inter-element interactions play a weaker role in ordering through ac demagnetisation. These phenomena are still under investigation. It is worth noting that the number of “red spins” and “blue spins” are very close to each other for all the samples in different states with different lattice spacing. Neither of the coloured spins show dominance even in the sample with the smallest lattice spacing after thermal annealing. This implies that the system is still in a phase where the symmetry has not been globally broken.

## 6.4 Summary

The order in the skeleton part of the system has been revealed by the calculation of an order parameter and of an average domain size, which has been extracted from colour mapped magnetic configurations for three different states. Both methods show that the thermally annealed states are more ordered than the other two states but still far from the ground state. The lattice spacing in the ac demagnetisation process was found to play a weak role in the ordering.



# Chapter 7

## Thermal fluctuation studies of Penrose tilings

### 7.1 Introduction

Not long after the artificial spin ice system was created, thermalisation was found preserved in as-grown states [65]. This discovery proved that ground state ordering could be achieved. The explanation of such an observation relies on the fact that when the nanoislands are in the initial deposition stage, the small volume of the islands means the energy barrier is small enough that it can be overcome by the thermal energy  $E = k_B T$  at the deposition temperature, where  $k_B$  is the Boltzmann constant. The energy barrier is given by

$$E_r = KV = \frac{1}{2}\mu_0 DM(T)^2 V, \quad (7.1)$$

where  $V$  is island volume,  $K$  is the shape anisotropy constant,  $\mu_0$  is the magnetic vacuum magnetic permeability and  $D$  is the difference between demagnetisation factors along the in-plane short and long axis of the island and magnetisation  $M(T) \propto 1 - cT^{3/2}$ , where  $c$  is a constant. Therefore, the elements behave like superparamagnets during the initial deposition stage. As the nano-islands are being grown, the islands' height and thus the volume of islands increases, as does the energy barrier to reversal. The rate of thermal fluctuation progressively slows down and the moment of islands gradually freeze. The islands therefore undergo

a transition from the superparamagnetic state to the ferromagnetic state. This kind of transition also happens in the thermal annealing experiment. For thermal annealing experiments, the temperature is varied from above the Curie temperature of the material back down to room temperature. The islands therefore undergo the same transition, since their energy barriers to reversal are low just below the Curie point, and they are briefly superparamagnetic before freezing on further cooling. In both cases, a blocking temperature can be used to characterise this phenomenon. The blocking temperature is given by

$$T_B = \frac{KV}{k_B \ln(t/t_0)}, \quad (7.2)$$

where  $K$ ,  $V$ ,  $k_B$  is the same as used in equation 7.1,  $t$  is the experiment measurement time and  $t_0$  is an attempt time, which is typically  $10^{-10}$  s. When a system is at a temperature below the blocking temperature  $T_B$ , the moment of an island cannot flip continuously between two stable directions, i.e. they are “blocked”. The blocking temperature thus depends on the particular laboratory experiment technique used, which defines  $t$ .

For artificial spin ice systems, the effect of the “inter-island coupling” cannot be neglected. When considering the inter-islands interactions, the energy barrier becomes  $E_b = E_r + E_i$ , where  $E_r$  is intrinsic energy barrier, and  $E_i$  arise from inter-islands interactions. These dipolar interactions between the islands slightly raises/lowers the energy barrier  $E_b$ , which can induce unfavourable/favourable moments configurations. The system can therefore transit towards low energy states during these thermally-activated dynamical processes.

Take the thermal annealing of the square ice, for example: when the system is at a temperature just below  $T_C$ , the magnetisation  $M_s \sim 0$ , and therefore the energy barrier as well as the dipolar interactions can be neglected. All 16 possible vertices energy states are equally-populated at this stage. As  $T_B$  is being approached, the energy barrier and the dipolar interactions increase: therefore, these interactions will gradually lift the degeneracy of four vertex configurations. This is because the thermal energy can overcome the shape anisotropy barrier towards lower energy. The reverse process becomes less likely because in order to jump from a low energy configuration to a high energy configuration, the

## 7.2 Temperature driven dynamics of Penrose tiling

---

thermal energy should not only overcome the shape anisotropy energy, but also overcome the additional energy that is the energy difference between these two configurations. Hence, a depopulation of high energy configurations is expected. If we describe the jump over the barrier from a high energy state to a low energy state process as the downward channel, the reverse process is the upward channel. The possibility of a jump happening in these two channels is different and is determined by the difference in the energy barriers that must be overcome. When  $T_B$  is approached, the energy difference is so large that the upward channel will freeze before all jumps become impossible (i.e. below  $T_B$ ).

For one of the square ice thermal annealing experiments, it has been shown that the energy difference between each vertex configuration is larger than the thermal energy when the temperature is close to the  $T_B$  [102]. Hence, below  $T_B$ , with significant depopulation of the high energy vertices, the system is expected to contain type one vertices only, i.e. the ground state. However, in some experiments, the samples did not approach the purely type one vertex configuration [102]. Instead, several domain boundaries arise between different ground state regions. One of explanations for this discrepancy is traced to the defects, such as island size and shape distribution, as not all the islands are identical due to the nano fabrication process, where a distribution of blocking temperature arises. During cooling process, the region with higher  $T_B$  would freeze first and nucleate the ground state ordered region. These frozen regions will become a seed of ground state order in different parts of the array. As the temperature decreases further, these regions will progressively expand until they reach another ground state region. These two regions will merge forming a larger region if they have the same form of order, or a boundary of type two and/or type three vertices will form if the two regions' order are incommensurate.

## 7.2 Temperature driven dynamics of Penrose tiling

For the Penrose tiling, due to non-periodicity, the number of neighbouring islands varies from site to site, as do the inter-islands interactions. Therefore, a wide blocking temperature distribution is expected. As discussed earlier, the ground state of Penrose tiling consist of two parts. One is the flippable part, which

## 7.2 Temperature driven dynamics of Penrose tiling

---

consists of type V, VI, and VII vertices and the other is the skeleton part, which consists of type I, II, III and IV vertices. For any vertex in the flippable part, due to the environment, it can choose one of its degenerate low energy configurations freely without changing the global energy of the system, i.e. no boundary can arise in the flippable part. Besides, the long-range order cannot be built in these regions as they are not connected to each other. On the other hand, the nucleation of the low energy state in these regions will not affect the long-range order in the skeleton part. For the vertices in the skeleton part, where the long-range order is expected to arise, due to the variety of blocking temperatures of different types of vertex, the long-range ordering through thermal annealing may be difficult. The reason is similar to the domain boundary forming in the square pattern during the thermal annealing experiment. As for Penrose tiling, a large distribution of blocking temperature is expected, a likely thermal annealing result is these vertices form a ground state region locally and these ground state regions form “domains”, which are consistent with that observed in the thermal annealing experiment (see figure 6.3).

### 7.2.1 The energy distribution of each vertex in different states

Based on the assumption that a long-range order may arise, we conduct a statistical analysis of vertex configuration populations for the thermally annealed state and the as-grown state. The results are displayed in figure 7.1 and 7.2 (the anomalies arise in energy population distribution are demonstrated in the later figure).

At a first glance, the energy levels are more uniformly occupied when the samples are in the as-grown state. After thermal annealing, the energy distributions have a clear shift toward the low energy direction for all types of vertex, which indicates that the thermal annealing is more effective in energy minimisation than the as-grown state. Most of the vertices are at the lowest and second lowest energy levels; hence, in order to simplify the analysis, we focus our study on these two levels of each vertex. The configurations of these two energy levels

## 7.2 Temperature driven dynamics of Penrose tiling

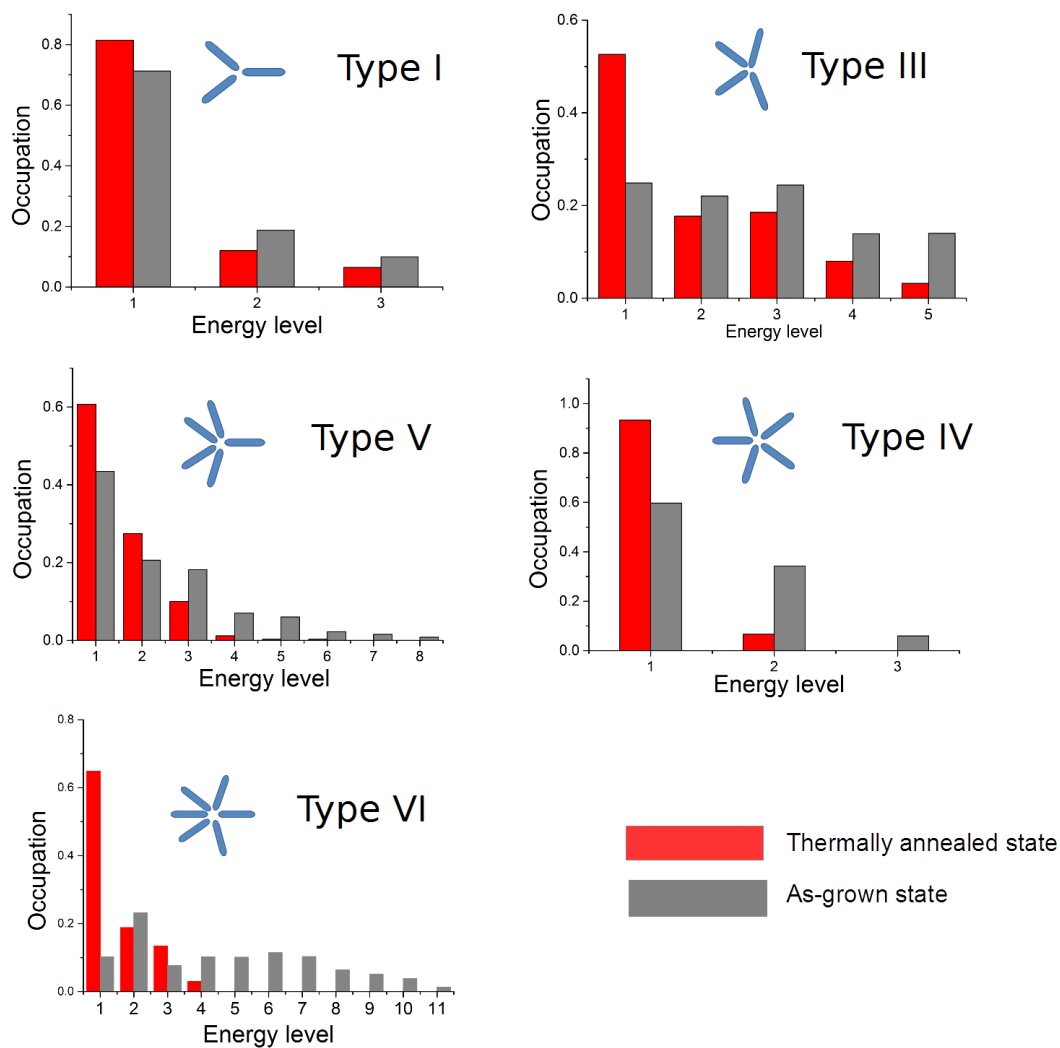


Figure 7.1: Vertex energy level occupations (part I): The energy level occupation of five types of vertices when samples are in the as-grown state (gray bar) and the thermally annealed state (red bar). Each figure shows the population of the vertex energy levels for a certain vertex type.

## 7.2 Temperature driven dynamics of Penrose tiling

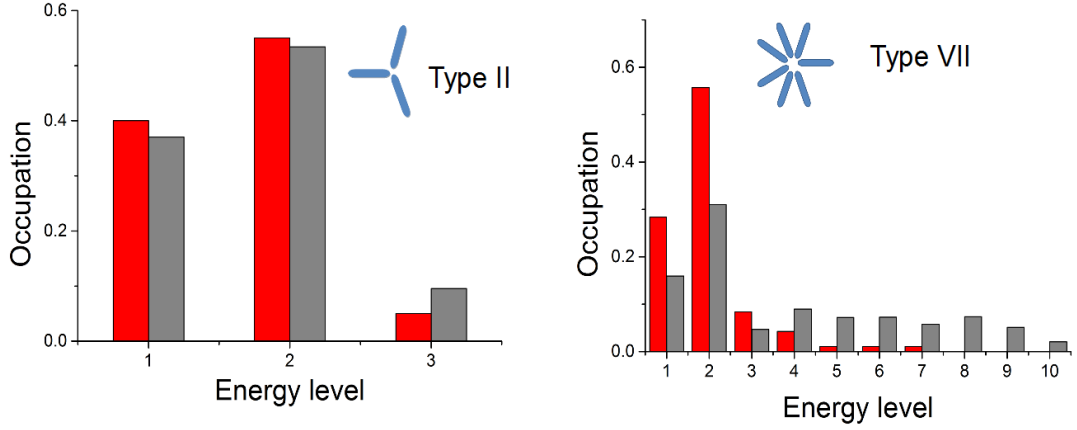


Figure 7.2: Vertex energy level occupations (part II): The energy level occupation for remaining two types of vertices when samples are in as-fabricated state (gray bar) and the thermally annealed state (red bar). The type VII vertex energy level are partly listed.

for each type of vertex have been listed in figure 4.2. Based on the calculation, each energy level of vertex configuration can be identified from the MFM images.

For thermodynamic studies in artificial spin ice systems, the frequency of the excitations is expected to follow the Boltzmann distribution. This has been found both from the as-grown state and the thermally annealed state for the square pattern [65; 69]. For the Penrose tiling, the number of excitations at high energy level for most of vertices is insufficient to extract a Boltzmann law. Nevertheless, from the population distribution of the lowest two energy level, we could still extract some information. For type I, III, IV, V, and VI vertices, the population of the second energy level is significantly less than the lowest energy level after thermal annealing. This is expected as in the thermal annealing process, the thermal energy would prefer to overcome the energy barrier towards low energy configuration direction. However, for type II vertices in the as-grown state and the thermally annealed state, more vertices were found to stay at the second energy level. For type VII vertices, this excessive population is more significant (see figure 7.3). This phenomena has been both observed in the as-grown state

## 7.2 Temperature driven dynamics of Penrose tiling

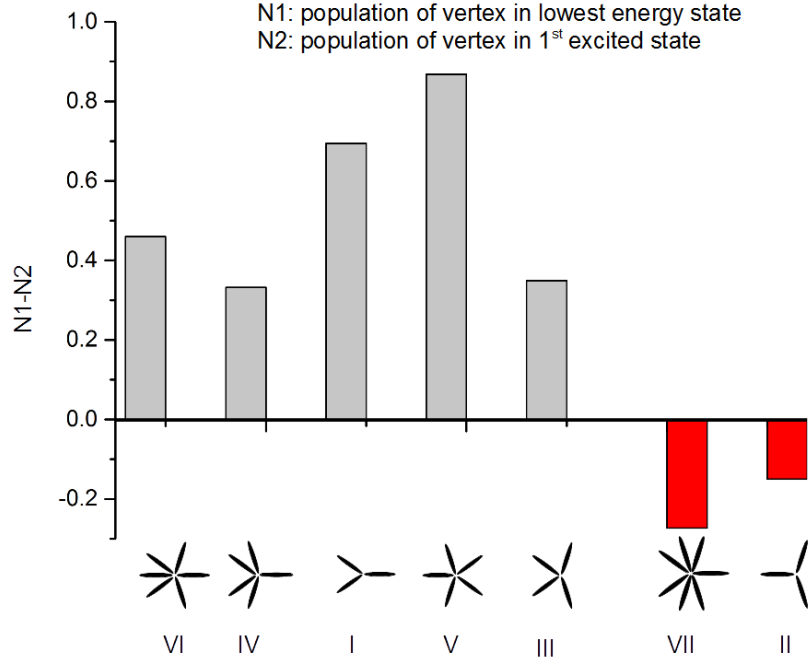


Figure 7.3: The difference between the lowest and second lowest vertex energy configuration populations for seven vertices when samples are in the thermally annealed state. Negative values mean that the second energy level has a higher population than the first energy level. Data comes from four samples with a lattice constant 600 nm.

and the thermally annealed state, hence it is not a statistical anomaly.

For type II vertex, the excessive population is reasonable. This is because part of type II vertex has to stay at the second energy level due to the construction of the ground state of the whole pattern. The ratio of  $E_1/E_2$  for type II vertex is 0.4 in the ideal ground state of the Penrose tiling, which is slightly lower than the experimental value. However, for type VII vertex, the excessive population is unusual. As we will show below, this result is due to the Boltzmann distribution. A more precise Boltzmann distribution should take the degeneracy factor into account, which is

$$n(J) = g(J) \exp E(J)/k_B T$$

where  $n(J)$  is the population density of level  $J$  and  $g(J)$  is the degeneracy which

## 7.2 Temperature driven dynamics of Penrose tiling

---

is the number of degenerated states in energy level  $J$ . The population ratio in two different energy states therefore is

$$\frac{F_1}{F_2} = \frac{g(1)}{g(2)} \exp \frac{E_1 - E_2}{k_B T}. \quad (7.3)$$

In most case, the degeneracy factor is neglected, as it is insignificant compared with the exponential factor. However, we will show below that for type VII vertex, when the temperature is close to  $T_B$ , the energy difference between the first and second energy level is comparable with the thermal energy. Hence the degeneracy factor plays a more important role in the population distribution.

For a type VII vertex, we will show below that it costs little energy to excite from the ground state to the first excited state. As illustrated in figure 7.4, when a Penrose tiling array is in the ground state, it needs to flip three islands to excite a type VII vertex from its lowest energy state to its first excited state. These three islands flipping will alter the configurations of their neighbouring vertices, which is marked by number 1, 2 and 3 in figure 7.4. The vertices 1 and 3 are all type II vertices; the islands flipping will raise the energy of one vertex and lower the other, which does not change the total energy. The states of the two vertices are marked by a red or green dot in figure 7.4, respectively. For the number 2 vertex, which is a type I vertex, the island flipping would not change the vertex energy, as the relevant island degenerates when type I vertex is in the lowest energy state (see figure 4.2). Therefore, when a type VII vertex is excited from its ground state to its first excited state, it can be treated as a disconnected vertex. The only energy cost is the energy difference between the initial and final energy states. Therefore, it is much lower than the corresponding energy cost in other type of vertices. As discussed earlier, the thermal activation rate from ground state to the first excited state (upward channel) depends on the shape energy barrier  $E_r$  and the inter-island interactions energy barrier  $E_i$ . More precisely, it is proportional to  $\exp(-(E_i + E_r)/k_B T)$ , while the reverse process rate (downward channel) depend on the shape energy barrier only, i.e. proportional to  $\exp(-E_r/k_B T)$ . (It does not need to overcome the inter-islands interactions in the reverse process). The depopulation of an energy state depends on the ratio of these two, which is  $\exp(-E_i/k_B T)$ . For a type VII vertex, the small  $E_i$  implies that the depopulation rate for the first excited state is low.



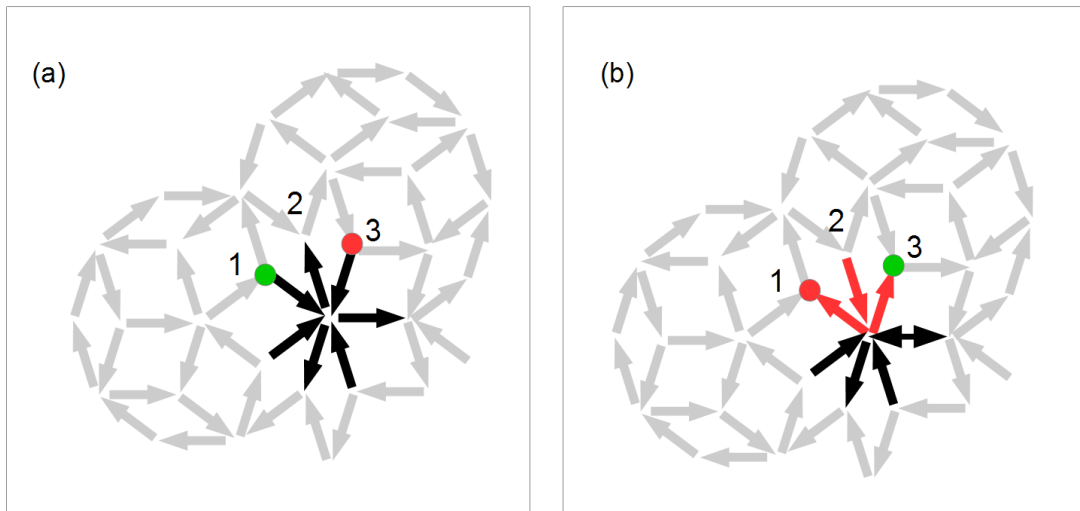


Figure 7.4: Type VII vertex configuration transit: (a) A type VII vertex (black arrows) is in the lowest energy configuration. (b) The type VII vertex is in the first excited energy configuration. The red arrows represent that the elements moments are reversed with respect to the configuration in (a). The reversed islands change the configurations of three neighbouring vertices, which are labelled 1, 2 and 3, respectively. The flipped islands will affect two type II vertices (marked by number 1 and 3) by raising the energy of one and lowering the energy of the other by exactly the same amount. The other flipped island did not change the energy of type I vertex (marked by number 2).

## 7.2 Temperature driven dynamics of Penrose tiling

---

On the other hand, for a type VII vertex, three islands need to be flipped to alter the configuration (either from  $E_2$  to  $E_1$  or from  $E_1$  to  $E_2$ ). As indicated by equation 7.1, the energy barriers are proportional to the volume of the reversing magnetic body, and so the energy barrier for a type VII vertex to relax into its ground state is higher than for the other vertex that only needs to flip a single island to do so. Considering all of the above, these type VII vertices drop out of the thermal equilibrium sooner and can arrest at a higher temperature than the others, leaving a highly excited population to be imaged in MFM experiments. The population ratio between  $E_2$  and  $E_1$  observed from the MFM experiments is 1.964, which is close to the value at the high temperature. (At high temperature, the magnetisation and thus the dipolar interactions can be neglected; therefore, energy difference  $E_2 - E_1$  in type VII vertex is close to zero. The population ratio between these two energy levels is given by the degeneracy factor ratio, which is 2). The observation confirms the assumption made above.

To realise this, we can consider in detail the blocking temperature of type VII vertices. The blocking temperature can be evaluated from the expression of  $T_B$  given above (Eq. 7.2), which can be cast in the following form:

$$\ln \frac{\tau_m}{\tau_0} k_B T_B = KV = \frac{1}{2} \mu_0 M_s^2(T_B) DV. \quad (7.4)$$

The  $t_m$  is the measurement time, we use  $t_m = 3$  s considering that the cooling rate in the thermal annealing process is 0.33 K/s (assuming that the moment on a particle is relaxed in 3 seconds when the system is cooled by 1 K). The measured  $M_s$  versus  $T$  of a 25 nm thickness film made of Py with 200 nm silicon nitride buffer is shown in figure 7.5; we use  $D = 0.141$  (calculated using the expressions given in [103]). The volume of a nanoisland is  $6.67 \times 10^{-22}$  m<sup>3</sup>. For a type VII vertex in our Penrose tiling, the reversal energy barrier can be estimated by considering reversal of one element from the ground state configuration, resulting in the creation of a second excited energy state, as shown in figure 7.6, as this would mostly minimise the  $E_r$  and  $E_i$  at the same time. The blocking temperature equation 7.4 can be solved graphically. The blocking temperature equation can be rewritten as  $F(T_B) = M_S(T_B)$ , where

$$F(T_B) = \sqrt{\frac{2 \ln \frac{t_m}{t_0} k_B T_B}{\mu_0 \Delta N V}}. \quad (7.5)$$

## 7.2 Temperature driven dynamics of Penrose tiling

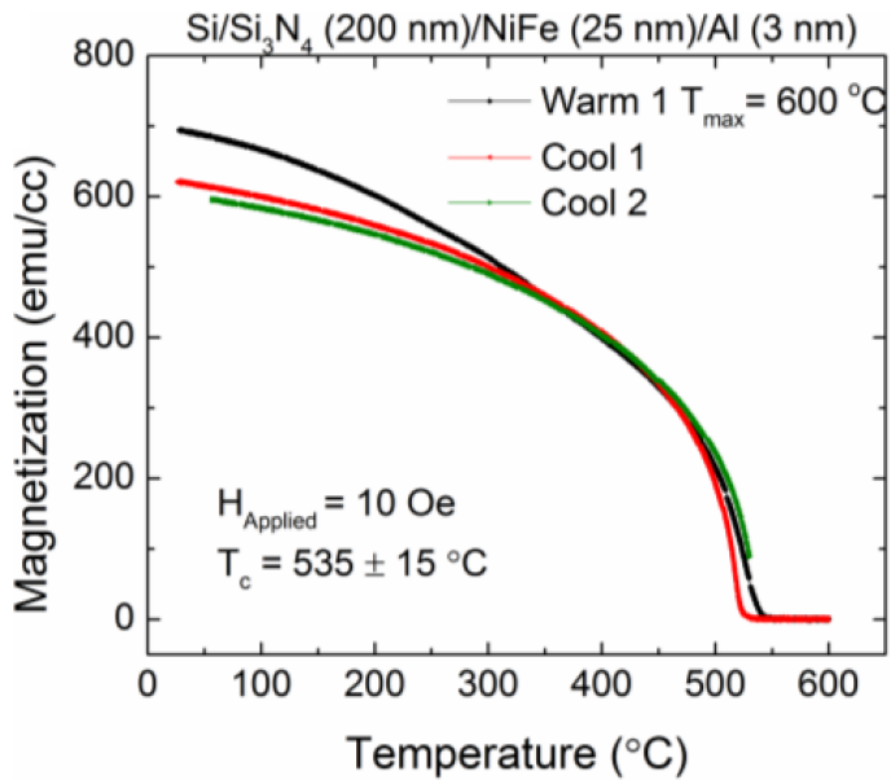


Figure 7.5: Magnetisation data for a permalloy film on Si<sub>3</sub>N<sub>4</sub>: Magnetisation as a function of temperature for a 25 nm thickness permalloy film on Si/Si<sub>3</sub>N<sub>4</sub>. Data comes from [69].

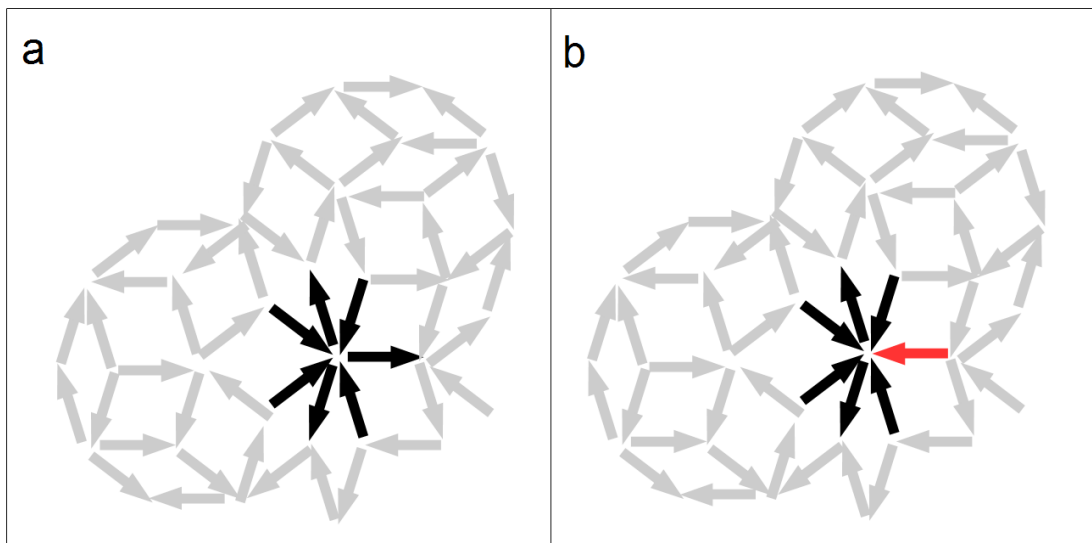


Figure 7.6: The inter-island interaction barrier estimation in type VII vertex: a element in type VII vertex ground state reverses its magnetic moment, resulting in a second energy level configuration; its neighbouring vertex (type IV vertex) configuration energy does not change because the element moment is degenerate in this vertex. This choice is the optimised way to minimise the reversal energy barrier.

## 7.2 Temperature driven dynamics of Penrose tiling

---

The result is shown in figure 7.7(a), where the intersection gives the blocking temperature  $T_B=789$  K. At this temperature, the saturation magnetisation has a value of 64 kA/m, which we used to evaluate the dipolar magnetostatic energy for different configurations. The energy was calculated using the OOMMF micro-magnetics simulation platform, for which we used a simulation unit comprising nanoislands forming a vertex with the specified  $M_S$  above and the orientation of each element moment was set according to each vertex magnetic configuration. Each island is divided into cubic cells with a 5 nm side for the simulation. For the type VII vertex, the energy of the ground state, first excited state, and the second excited state are 0.4043 aJ, 0.4057 aJ and 0.4253 aJ, respectively. The thermal energy at the blocking temperature is 0.109 aJ. The degeneracy factor of the ground state, first excited state, and the second excited state of type VII vertex are 2, 4, and 2. Based on these parameters, the population ratio of  $E_2/E_1$  and  $E_3/E_1$  can be calculated using equation 7.3 and the result is plotted in figure 7.7(b), which is not far from the experimental value. Therefore, the anomaly in the population distribution is from the degeneracy factor in the Boltzmann distribution law. In the calculation above, the inter-island interactions are neglected, i.e.  $E_i$  has not been considered in the blocking temperature equation. A more precise equation should be

$$\ln \frac{t_m}{t_0} k_B T_B = \frac{1}{2} \mu_0 M_s^2(T_B) \Delta N V + E_i. \quad (7.6)$$

The order of the inter-islands interaction can be estimated from this equation. As  $\ln \frac{t_m}{t_0}$  is roughly 24, which means the shape anisotropy energy  $KV$  is about 24 times of the thermal energy  $k_B T_B$  at the blocking temperature, while according to the calculation above, the  $E_i$  for type VII vertex is roughly 1/8 of the thermal energy at the blocking temperature. Therefore, the shape anisotropy energy is approximately more than 100 times that of the  $E_i$  for type VII vertex, which means  $E_i$  can be neglected in the calculation above. The population ratio of the other vertices can also be obtained in the same way. The population distributions for type 1 and 3 vertices are shown in figure 7.8a and b, respectively, which capture most details of the experiment. To further explain this model, we give a comparison of population distribution between square pattern and Penrose tiling pattern. According to the calculation and simulation in [102], the blocking

## 7.2 Temperature driven dynamics of Penrose tiling

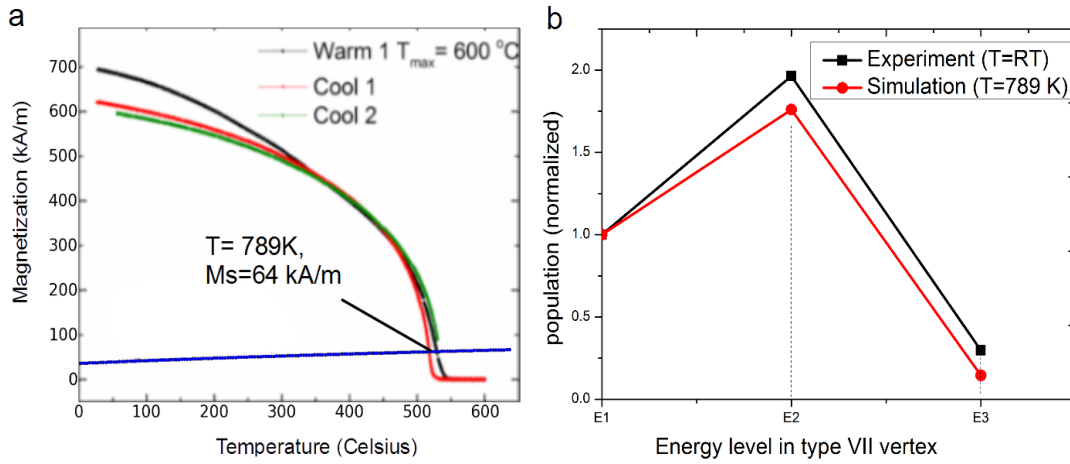


Figure 7.7: Blocking temperature equation solution and energy population of type VII vertex: (a) The blocking temperature function (see equation 7.5) of a nano-island (blue) and magnetisation of a 25 nm thickness Permalloy film (red) as a function of temperature. The intersection gives the blocking temperature of type VII vertex and the corresponding saturation magnetisation. (b) The energy population distribution of type VII vertex from experiment (black line) compared with simulation result (red line). Only the lowest three energy levels occupation are present. Experimental values are from the MFM images and the simulation result is based on the OOMMF simulation at blocking temperature given by (a).

## 7.2 Temperature driven dynamics of Penrose tiling

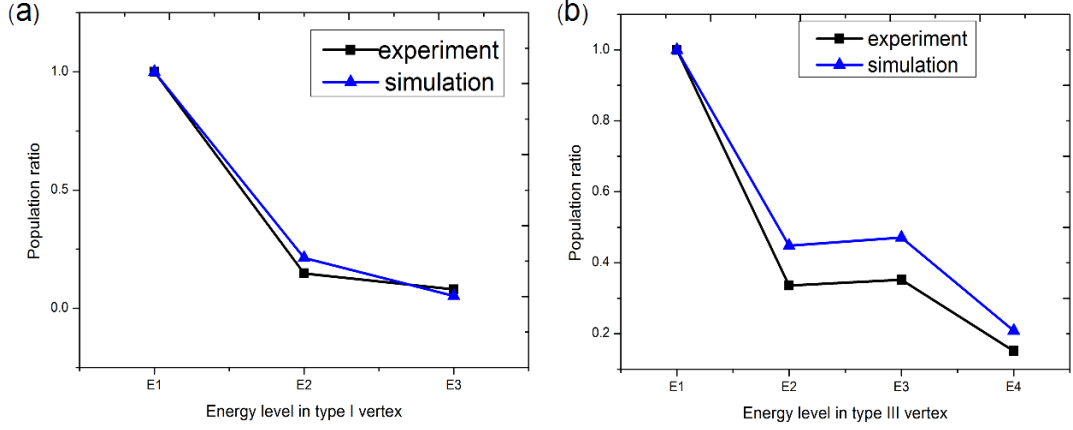


Figure 7.8: The energy population distribution of type I and type III vertex from experiment (black line) and simulation (blue line).

temperature of a square pattern array with 400 nm lattice constant is around 66 meV, and the energy difference between first and second vertex is roughly 390 meV. The  $E_2/E_1$  population ratio at the blocking temperature is 0.0054 according to the Boltzmann law; therefore, the degeneracy factor can be neglected and large ground state domains are found in the sample as most vertices are in the lowest energy state. The domain boundary which still arises, according to the discussion in [102], may be due to the distribution of island sizes or shapes that is unavoidable during the lithography process, which means there will be a distribution of blocking temperatures. Therefore, different regions nucleate at different temperatures and generate degenerated ground state regions.

For the Penrose tiling, as we calculated above, due to the large lattice constant (600 nm), the energy difference between different configurations is smaller than the square pattern, so that the excitations are much more frequently observed. For Penrose tilings, the blocking temperature has an intrinsic distribution, which is mainly caused by the non-periodicity rather than the defects generated during the fabrication process. However, this effect has not hindered the ground state being accessed. This can be inferred from the “domain” length calculation in chapter 6, as the “domain” length increased while the lattice spacing was reduced to 600 nm. From the blocking temperature calculation, it can be inferred that

the lattice constant reduction will induce strong inter-island interactions and consequently will broaden the blocking temperature distribution. However, this is not consistent with the trend of the “domain” length variation when the lattice spacing decreases; therefore, access to the ground state in the Penrose tiling is mainly driven by the lattice constant. The blocking temperature distribution may cause a notable effect at some point when the lattice spacing is reduced further; however, this is hard to achieve with the current lithography limits (otherwise the islands in type VII vertex will touch each other), and in order to further reduce the excitation and minimise the energy, the ratio of  $E_i/k_B T_B$  needs to be increased. For the future work, the energy minimisation effort should be made in modifying this ratio.

### 7.3 Summary

In summary, based on the blocking temperature calculation, the simulation result of population distribution at the blocking temperature is consistent with the experimental results obtained at room temperature, which shows that access to the ground state is mainly restricted by the lattice constant rather than the distribution of the blocking temperatures.



# Chapter 8

## Summary and future work

### 8.1 Summary

This thesis has experimentally addressed the behaviour of artificial magnetic Penrose tiling pattern under different energy minimisation protocols on different lattice constants. Magnetic force microscopy (MFM) allowed the magnetic configuration to be probed, from which the statistical analysis was conducted. In order to study the energy minimisation problem, we offered a low energy configuration of the whole pattern, which can accommodate most vertices in the lowest energy configurations. Hence, it is deemed to be a ground state of Penrose tiling. The ground state construction is based on the vertex configuration energies determined from the OOMMF simulations. Generic “ice-rules” were found to construct the lowest energy configuration for each vertex. Following this rule, the element’s magnetic moments of each vertex should point in and out alternately to minimise the magnetostatic energy. When tiling these low energy vertex configurations together, the degeneracy of each vertex configuration is removed, which induces two parts of the structure. One part, termed as the “skeleton part”, has a two-fold degenerate state. Hence, like the square pattern, a long-range order is expected to arise in this part. The other part, termed as the “flippable part”, has a multiply degenerate ground state. The vertices in this part can chose freely between degenerate states without altering the energy in the other part.

Based on the ground state of Penrose tiling, the energy minimisation has been addressed by three methods: as-grown state, rotational magnetic field demagneti-

sation, and thermal annealing after the fabrication stage. The as-grown state and thermally annealed state have been proved to induce long-range order in a square pattern [17; 65; 69]. These achievements suggest that the long-range order is expected to arise when similar protocols are conducted on the Penrose tiling pattern. From the rhombus population analysis, the population ratio of different rhombuses' configurations is close to the ground state when the samples are thermally annealed. However, a further study demonstrated that no large clusters stay in the lowest energy configuration. In order to further identify the order in the samples, a correlation function calculation was conducted on the sample's skeleton part. The magnitude of correlation for the thermally annealed state was found to be significantly higher than the other states. The correlation length that was estimated from the correlation curve is more than two neighbouring islands, i.e. only short-range correlation was found. Further to this, a special "domain" was defined based on the colour mapping of MFM images with the ground state skeleton part. An averaged "domain size" was calculated and clearly shows that the thermal annealing and as-fabricated state have similar trends as the lattice spacing is reduced. This shows that both of the states are thermally induced states. As a contrast, the averaged "domain" size is found to be almost irrelevant to the lattice constant after the field demagnetisation. It implies that the lattice constant plays a weaker role in the field ordering process and further investigation is ongoing to explore this phenomenon.

For the thermally annealed state, an excess population phenomenon was found to exist in the VII vertex energy population. Based on the calculation of the blocking temperature, the thermal excitations are found to follow the Boltzmann distribution at the blocking temperature. Hence the excitation population depends on the ratio between excitation energy and thermal energy at the blocking temperature. In order to reduce the number of excitations and thus minimise the total energy, this ratio needs to be enlarged. This can be approached by either decreasing the blocking temperature or increasing the inter-islands interactions.

## 8.2 Future work

The work presented in this thesis provides various avenues for future research. A number of points to be addressed are left out in this work. While the ground state of the Penrose tiling has been predicted, the validity of this configuration needs to be further tested. From an experimental view, it has been shown that the system's order in the skeleton part was significantly increased by the thermal annealing. However, the predicted long range order in the skeleton part is still far from being achieved. As shown in chapter 7, the thermal excitation populations are mainly determined by the ratio between the thermal excitation and thermal energy at the blocking temperature, rather than the distribution of the blocking temperature. Therefore, in order to minimise the total energy and increase the order of the system, this ratio has to be modified.

For the ac demagnetisation investigation, due to the complexity of the structure, it is difficult to conduct an "effective temperature" treatment on a Penrose tiling pattern. However, the study on a specially defined "domain" size shows that the averaged domain size increased after ac demagnetisation, but not by as great an extent as from the thermal annealing protocol. Besides, the lattice constants are found to play a weak role in the field ordering process. The details have not been investigated explicitly, and this would for an interesting avenue for future work. The field reversal problem has been intensively studied in square and kagome patterns. How the moments of system are correlated during field reversal due to interactions and frustration has become an interesting and important aspect. For Penrose tiling, not surprisingly, the different geometry induced different interactions as well as frustration will lead to new phenomena; hence, more work is expected in the future. For the thermalisation study, in the short-term, by varying the cooling rate or performing minor temperature loop, one can investigate the ground state ordering and averaged domain size distribution as a function of the cooling rate. In the long-term, the thermal fluctuation should be further investigated with other materials with different Curie temperatures and the behaviour can be studied by the other techniques such as Photoemission Electron Microscopy with X-ray Magnetic Circular Dichroism (PEEM-XMCD).

# Appendix A

## How to generate 2-D Penrose tiling

Since the aperiodic pattern possesses long range order, each element site can be predictable if the initial element site is known. However, mathematically, apart from the 1-D quasiperiodic chain (Fibonacci chain), there is no mathematical formula that could be relay upon to give each element site in the quasiperiodic pattern. Generally, in order to obtain Penrose tiling, one could utilise the self similar property of the quasiperiodic pattern, which could generate a large scale Penrose tiling pattern from a small piece (inflation rule). However, for this project, we need to trace each element site for statistical reasons. Therefore, another method is needed.

Rather than use the inflation/deflation rule, it was found firstly by de Bruijn [72] that Penrose tiling can be generated by projecting a certain slice of high dimensional cubic lattice into low dimension, which is called the “cut and projection” method. Several methods were developed afterwards [104; 105; 106]. The method we used is another form of the “cut and projection”, called the “section method”, which has advanced in calculation and coding. Details can be found in [107], but the basic idea is given below.

If one considers a  $N$  dimension cubic lattice  $\Lambda$  with an orthogonal unit vector, it has  $n$ -fold rotational invariance and belongs to rotational group  $\Gamma$ . The  $N$  cube lattice  $\Lambda$  can be decomposed into two subspaces, which we call  $R_{\parallel}$  (parallel space) and its complementary space  $R_{\perp}$  (perpendicular space), which have dimension

$N_{\parallel}$  and  $N_{\perp}$  respectively. The bases of  $R_{\parallel}$  and  $\Lambda$  are linked by the following transformation:

$$R_{\parallel}(j) = \sum_{i=1}^N q_{ij} \cdot \Lambda_i,$$

where  $q_{ij}$  is the transformation matrix element,  $R_{\parallel}(j)$  is the basis of  $R_{\parallel}$  and  $\Lambda_i$  is the basis of  $\Lambda$ . Let  $C$  be a unit hypercube of  $\Lambda$ . When  $C$  is projected into perpendicular space  $R_{\perp}$ , the object that derives,  $C_{\perp}$ , is called “window”.

When a set of points  $X$  in  $\Lambda$  are projected into its parallel space  $R_{\parallel}$  and perpendicular space  $R_{\perp}$ , one will get point sets  $X_{\parallel}$  and  $X_{\perp}$  respectively. If parallel space  $R_{\parallel}$  is chosen to invariance under rotational group  $\Gamma_{R_{\parallel}}$ , where  $\Gamma_{R_{\parallel}}$  is an irreducible subgroup of rotation group  $\Gamma$ , then the point set  $X_{\parallel}$  would be invariant under  $\Gamma_{R_{\parallel}}$ . If the transformation element  $q_{ij}$  are irrational numbers, the set of points  $X_{\parallel}$  will form a quasiperiodic pattern [108].

## A.1 1-D quasiperiodic pattern

We will begin from a one dimensional example, the Fibonacci chain, which is a 1-D aperiodic structure. It can be generated from a 2-D square lattice, as illustrated in figure A.1. A 2-D square lattice is aligned with an irrational slope respect to the horizontal line. The slope is given by  $\cos \alpha / \sin \alpha = \tau$ , where  $\tau$  is the golden ratio and  $\alpha$  is the angle between the square row and the horizontal line. For each point in the square lattice, a vertical bar is placed on it with width  $D$ ,  $D$  is a window in this case, which is defined as a unit square diagonal projected along vertical direction (perpendicular space). The vertical bar has cross section with a horizontal line (parallel space), and gives a set of points which form the quasiperiodic chain, or in other words, the Fibonacci chain.

## A.2 Penrose tiling

The 2-D Penrose tiling pattern can be derived from a five dimensional cubic lattice. When a five dimensional cubic lattice  $\Lambda$  is given, it is invariant under five-fold rotation which belongs to rotation group  $\Gamma$ .  $\Gamma$  can be decomposed into three irreducible subgroup  $\Gamma_{R_{\parallel}}, \Gamma_{R_{\perp}}, \Delta$ . In this case, the  $\Gamma_{R_{\parallel}}$  is the parallel space

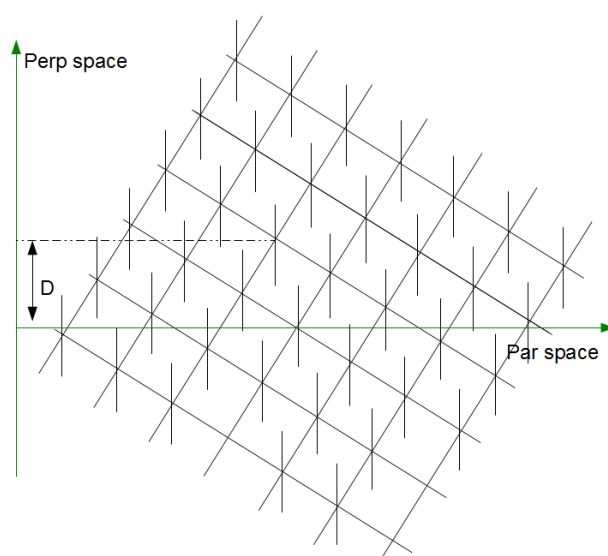


Figure A.1: 2-D projection method: A 2-D square lattice is aligned with an irrational slope in respect to the horizontal line. Each point in 2-D lattice is placed on a vertical bar(see text). Some vertical bars have a cross section in the horizontal line( parallel space), which gives a set of points. These points can be deemed to be the Fibonacci chain.

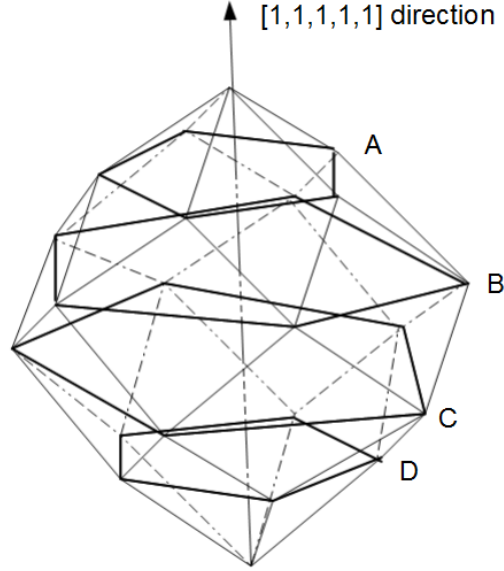


Figure A.2: Icosahedral space: When a unit hypercube in 5-D is projected into a 3-D perpendicular space, a rhombic icosahedron will be formed. The points which are projected from  $\Gamma$  are constrained in four pentagonal planes, which are normal to the  $[11111]$  direction. They are marked A, B, C, and D, respectively.

in this case, and the  $\Gamma_{R_{\perp}}$  sum with  $\Delta$  is the perpendicular space. The  $\Gamma_{R_{\parallel}}$  space inherits the five-fold rotational invariance from  $\Gamma$ . The  $\Delta$  space is a one dimensional space along the  $[11111]$  direction. The transformation matrix that links the basis of the subspace and the basis of the hypercube space is

$$R_{\parallel} = \sqrt{2/5} \begin{pmatrix} 1 & \cos \theta & \cos 2\theta & \cos 2\theta & \cos \theta \\ 0 & \sin \theta & \sin 2\theta & -\sin 2\theta & -\sin \theta \end{pmatrix}$$

$$R_{\perp} = \sqrt{2/5} \begin{pmatrix} 1 & \cos 2\theta & \cos \theta & \cos \theta & \cos \theta \\ 0 & \sin 2\theta & -\sin \theta & \sin \theta & -\sin 2\theta \\ \frac{1}{\sqrt{2}} & \frac{1}{\sqrt{2}} & \frac{1}{\sqrt{2}} & \frac{1}{\sqrt{2}} & \frac{1}{\sqrt{2}} \end{pmatrix}$$

where  $\theta = 2\pi/5$ . From the second matrix equation, we know that when projected into the  $R_{\perp}$  space, the points would sit on four planes, which are normal to the  $[11111]$  direction with intervals of  $1/\sqrt{5}$  of unit length in 5-D. The “window”  $C_{\perp}$  is obtained by projecting a hypercube unit C into perpendicular space  $R_{\perp}$ , therefore being formed by 4 pentagonal planes, which amount to a rhombic icosahedron,

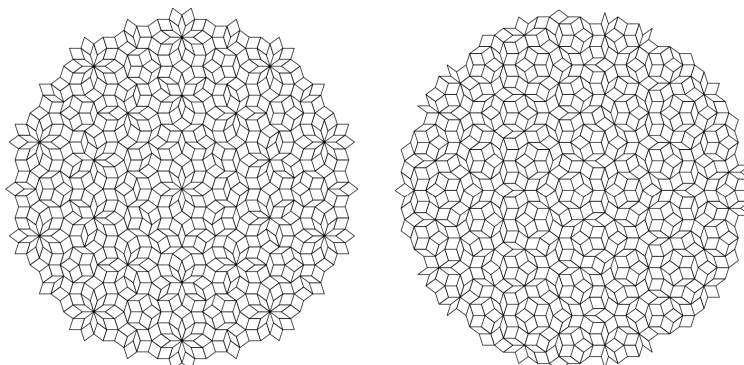


Figure A.3: Tiling generated by different value of  $\gamma$ : Left: When choosing  $\gamma = 0$ , the pattern contains ten-fold symmetry vertices. Right: When choosing  $\gamma = 0.3$ , the pattern is a Penrose tiling.

as shown in figure A.2. Therefore, a finite section of  $\Lambda$  is chosen, called  $X$ . If the points of  $X$  that are projected into perpendicular space sit inside  $C_{\perp}$  (window), then the points in the parallel space would be invariantly under a five-fold rotation. The pattern obtained, however, possesses both five-fold symmetry and two-fold symmetry, thus it cannot be a Penrose tiling pattern. In order to break the two-fold symmetry, there is another important parameter  $\gamma$ , which is used to shift the four planes in  $C_{\perp}$  along the  $[11111]$  direction. It has been shown that when  $\gamma$  varies from 0 to 0.5, it generate distinct patterns [109]. When  $5\gamma = 0 \pmod{1}$ , the pattern contains locally ten-fold symmetric vertices. When  $5\gamma = 0.5 \pmod{1}$ , the structure is a Penrose tiling, as shown in figure A.3. For the pattern used in the experiment in this thesis, the scale of the 5-D hypercube is chosen to be 3 unit lengths along each axis, and  $\gamma$  is 0.3.



# Appendix B

## All possible vertex configurations and their corresponding energies

### B.1 Appendix B

All possible configurations of each type of vertex in the Penrose tiling, with corresponding magnetostatic energy and degeneracy are listed below:

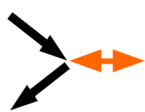
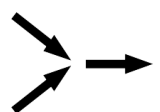
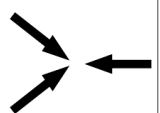
Type I			
Energy( $10^{-17}$ J)	2.923	3.03	3.21
Degeneracy	4	2	2

Figure B.1: All possible configurations, and corresponding energies, of a type I vertex. The red arrow represents an energetically degenerate island moment.

Type II			
Energy( $10^{-17}$ J)	2.674	2.699	2.904
Degeneracy	2	4	2

Figure B.2: All possible configurations, and corresponding energies, of a type II vertex. The red arrow represents an energetically degenerate island moment.

Type III						
Energy( $10^{-17}$ J)	3.9	4.00	4.08	4.10	4.18	4.54
Degeneracy	2	2	4	2	4	2

Figure B.3: All possible configurations, and corresponding energies, of a type III vertex.

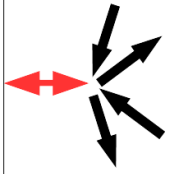
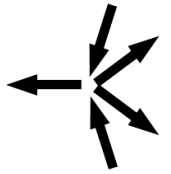
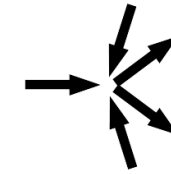
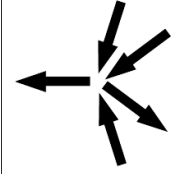
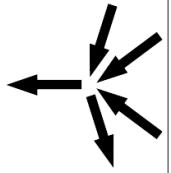
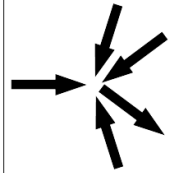
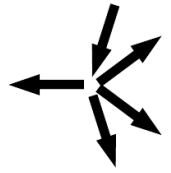
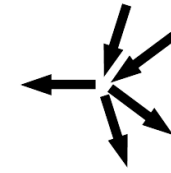
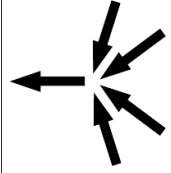
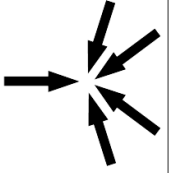
Type IV					
Energy( $10^{-17}$ J)	4.42	4.44	4.49	4.78	4.9
Degeneracy	4	2	2	4	4
Type IV					
Energy( $10^{-17}$ J)	5.00	5.07	5.18	5.49	5.90
Degeneracy	4	4	4	2	2

Figure B.4: All possible configurations, and corresponding energies, of a type IV vertex. The red arrow represents an energetically degenerate island moment.

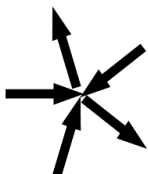
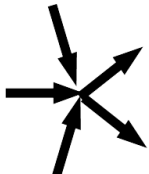
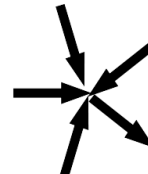
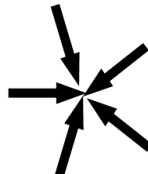
Type V				
Energy( $10^{-17}$ J)	4.74	4.94	5.11	5.67
Degeneracy	10	10	10	2

Figure B.5: All possible configurations, and corresponding energies, of a type V vertex.

Type VI					
Energy( $10^{-17}$ J)	5.23	5.39	5.45	5.50	5.53
Degeneracy	2	4	2	4	2
Energy( $10^{-17}$ J)	5.57	5.61	5.70	5.71	5.79
Degeneracy	2	4	4	4	4
Energy( $10^{-17}$ J)	5.87	5.88	5.93	6.07	6.16
Degeneracy	4	4	4	4	2
Energy( $10^{-17}$ J)	6.20	6.29	6.55	6.58	7.23
Degeneracy	2	4	4	2	2

Figure B.6: All possible configurations, and corresponding energies, of a type VI vertex.

Type VII						
Energy( $10^{-17}$ J)	5.97	5.99	6.18	6.20	6.292	6.294
Degeneracy	2	4	4	4	4	2
Type VII						
Energy( $10^{-17}$ J)	6.33	6.35	6.36	6.46	6.51	6.53
Degeneracy	4	4	4	2	4	4
Type VII						
Energy( $10^{-17}$ J)	6.538	6.54	6.56	6.57	6.743	6.746
Degeneracy	4	4	4	4	4	2
Type VII						
Energy( $10^{-17}$ J)	6.747	6.78	6.79	6.91	6.93	6.94
Degeneracy	4	4	2	2	4	4
Type VII						
Energy( $10^{-17}$ J)	6.99	7.11	7.15	7.31	7.326	7.329
Degeneracy	4	4	4	4	4	4
Type VII						
Energy( $10^{-17}$ J)	7.515	7.54	7.747	7.752	8.12	8.93
Degeneracy	4	4	4	4	2	2

Figure B.7: All possible configurations, and corresponding energies, of a type VII vertex.

# Appendix C

## Some selected AFM, MFM and SEM images

### C.1 Appendix C

Some representative AFM and MFM images used for statistical study of Penrose tiling system in three different states are given in the following (all the images were obtained from a Veeco nanoman system with standard MESP tip and all the images in this series have 900 nm lattice constant):

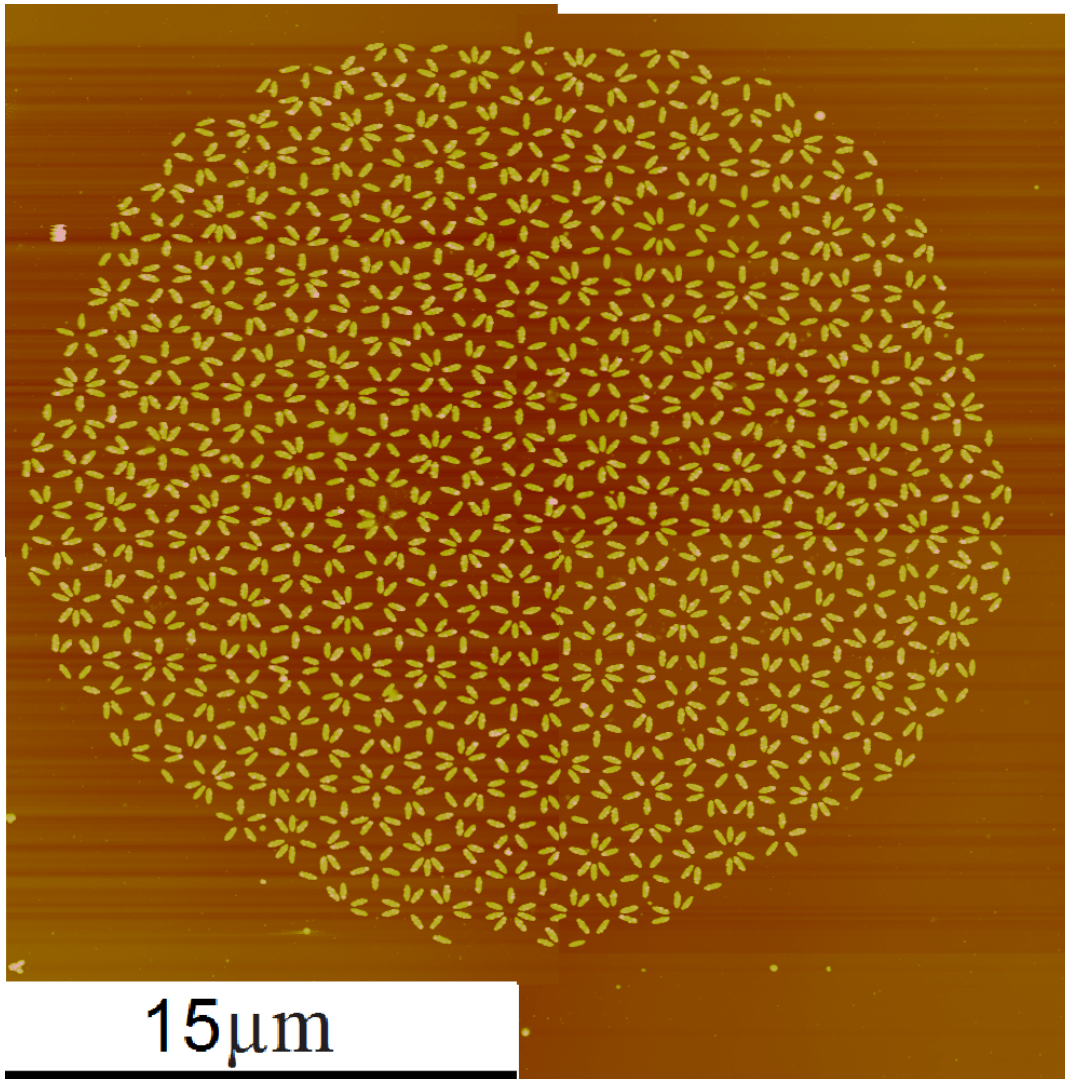


Figure C.1: The AFM image of pattern when the sample was in the as grown state.

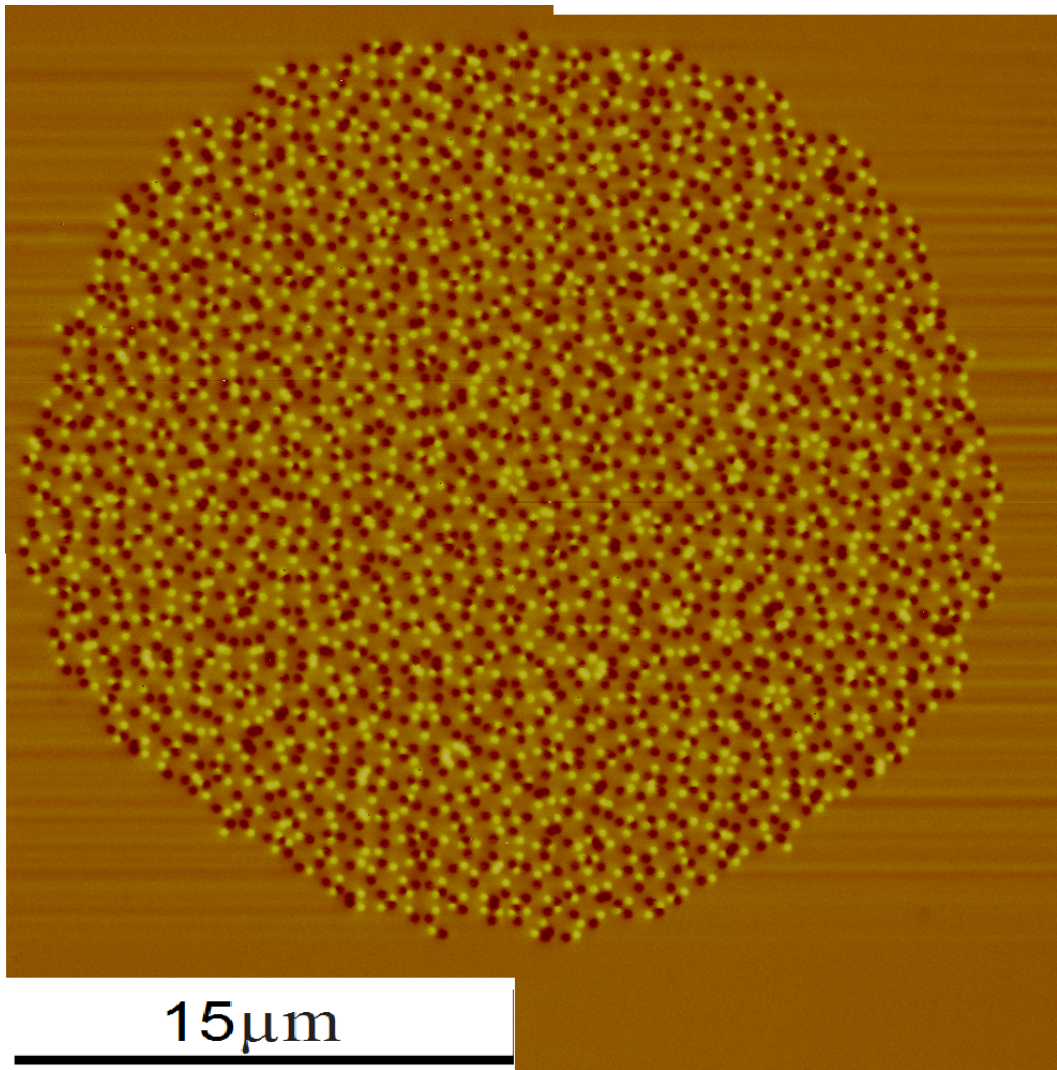


Figure C.2: The MFM image of the pattern when the sample was in the as grown state. The image corresponds to the topography image in the previous figure.



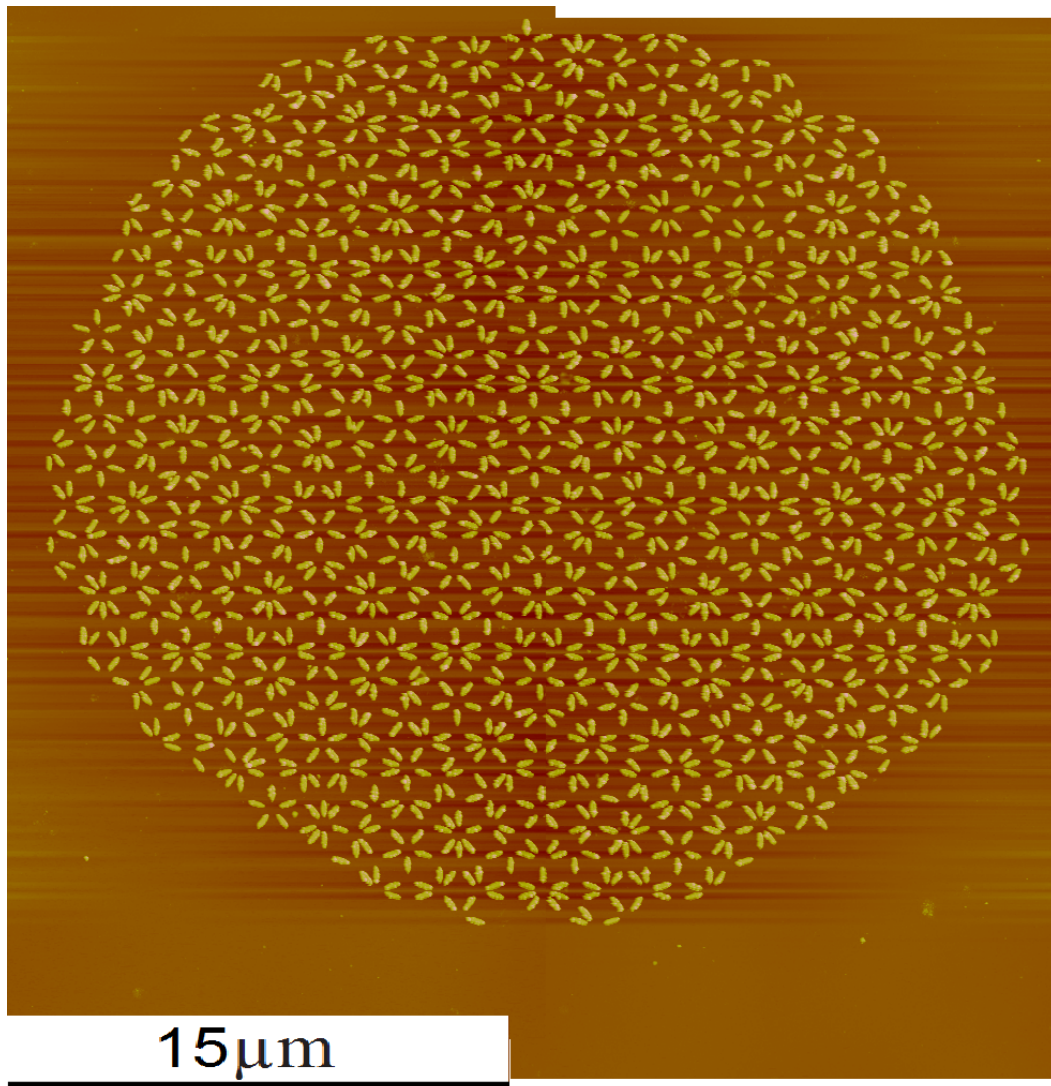


Figure C.3: The AFM image of the pattern when the sample was in the ac demagnetised state.

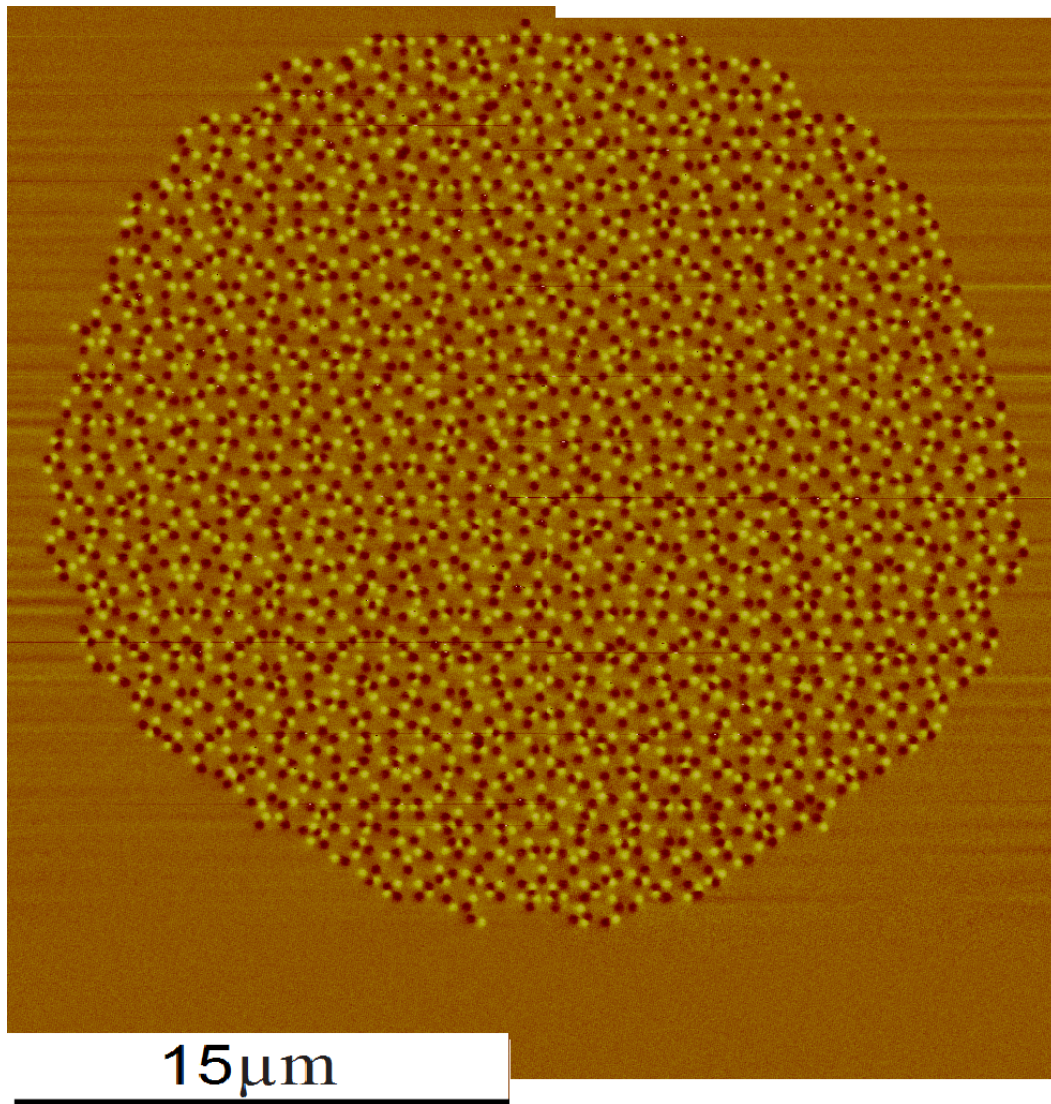


Figure C.4: The MFM image of the pattern when the sample was in the ac demagnetised state. The image corresponds to the topography image in the previous figure.



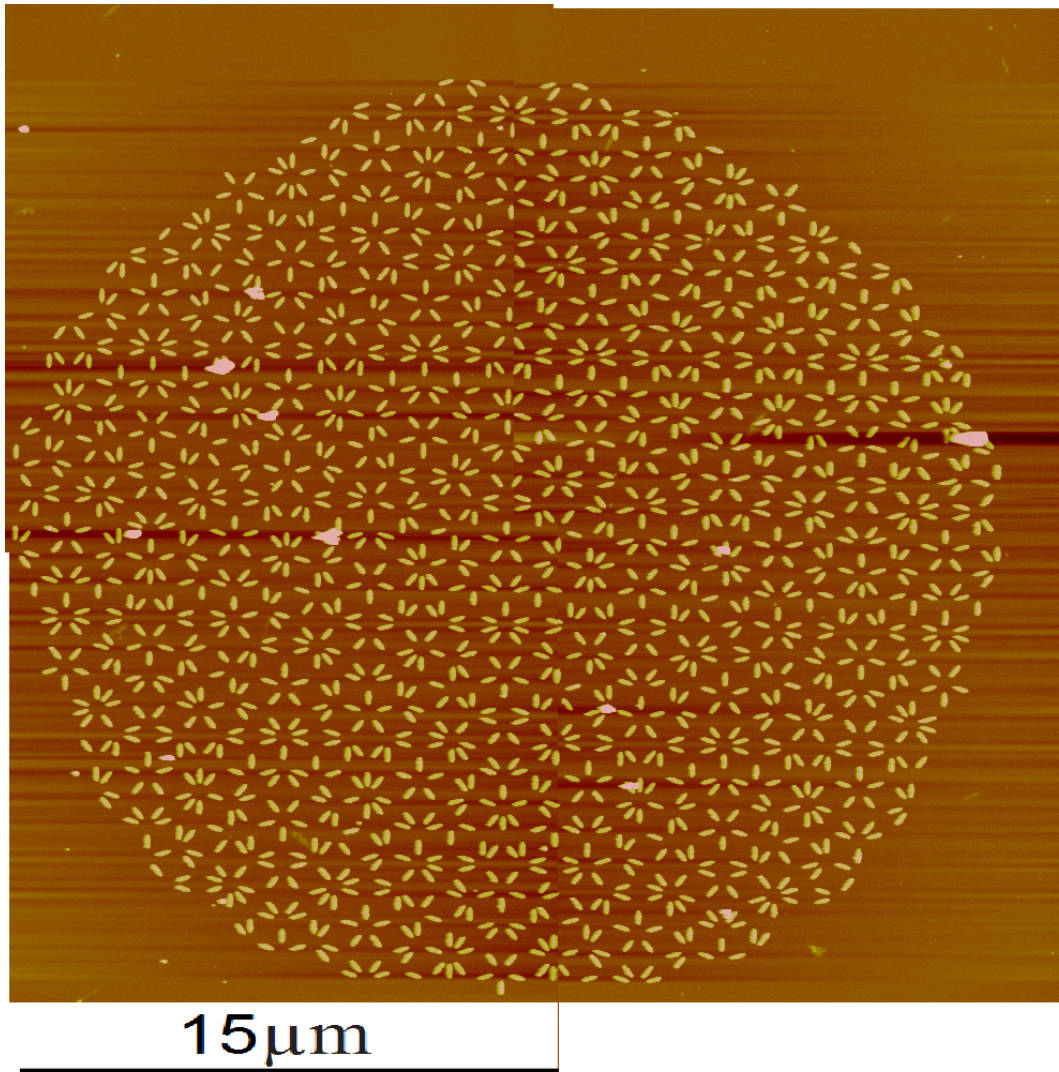


Figure C.5: The AFM image of the pattern when the sample has been thermally annealed. The pattern survived the anneal well and only a few small pieces of debris appeared, which do not affect the magnetic imaging, as can be seen in the next figure.

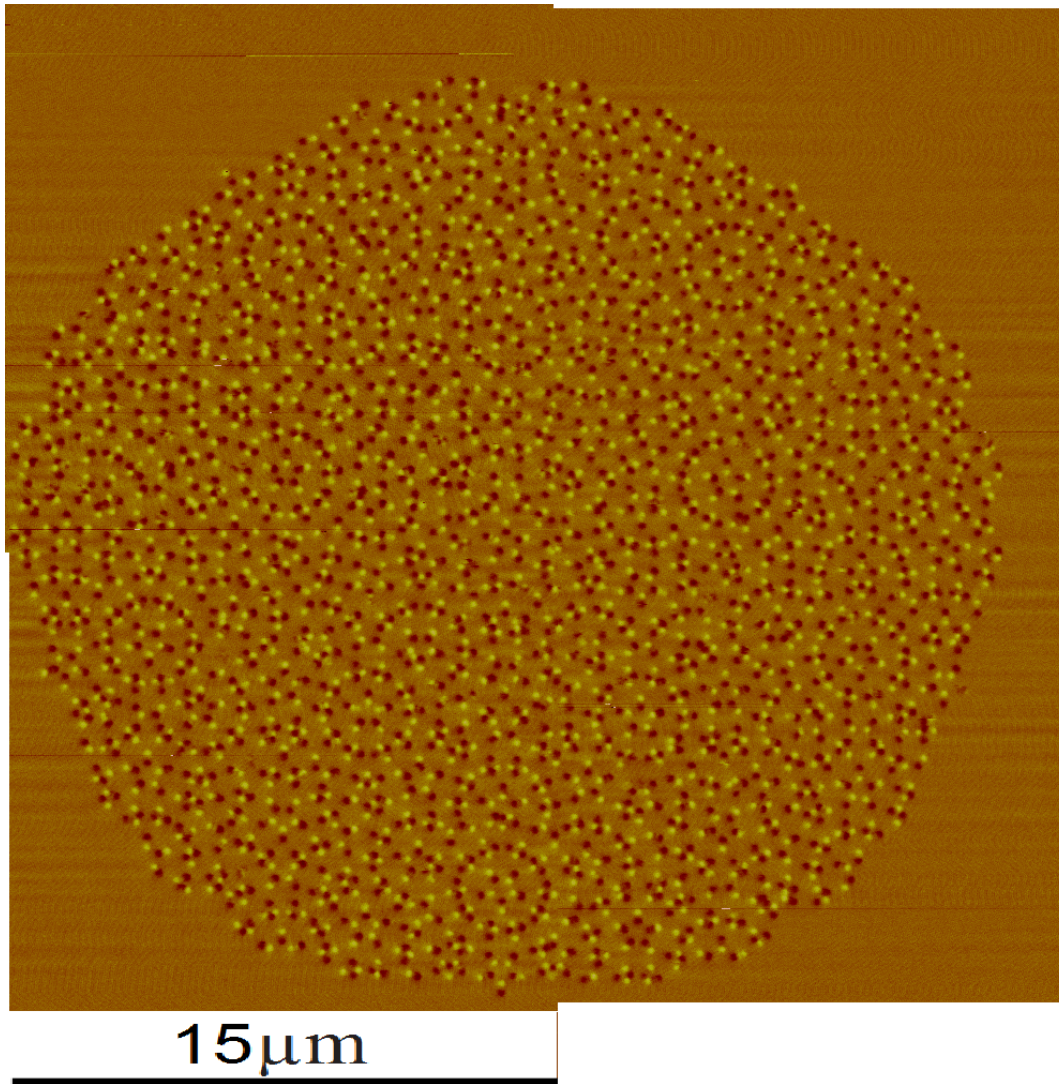


Figure C.6: The MFM image of the pattern when the sample has been thermally annealed. The image corresponds to the topography image in the previous figure. The debris that appeared in the previous figure has no affected the magnetic imaging.



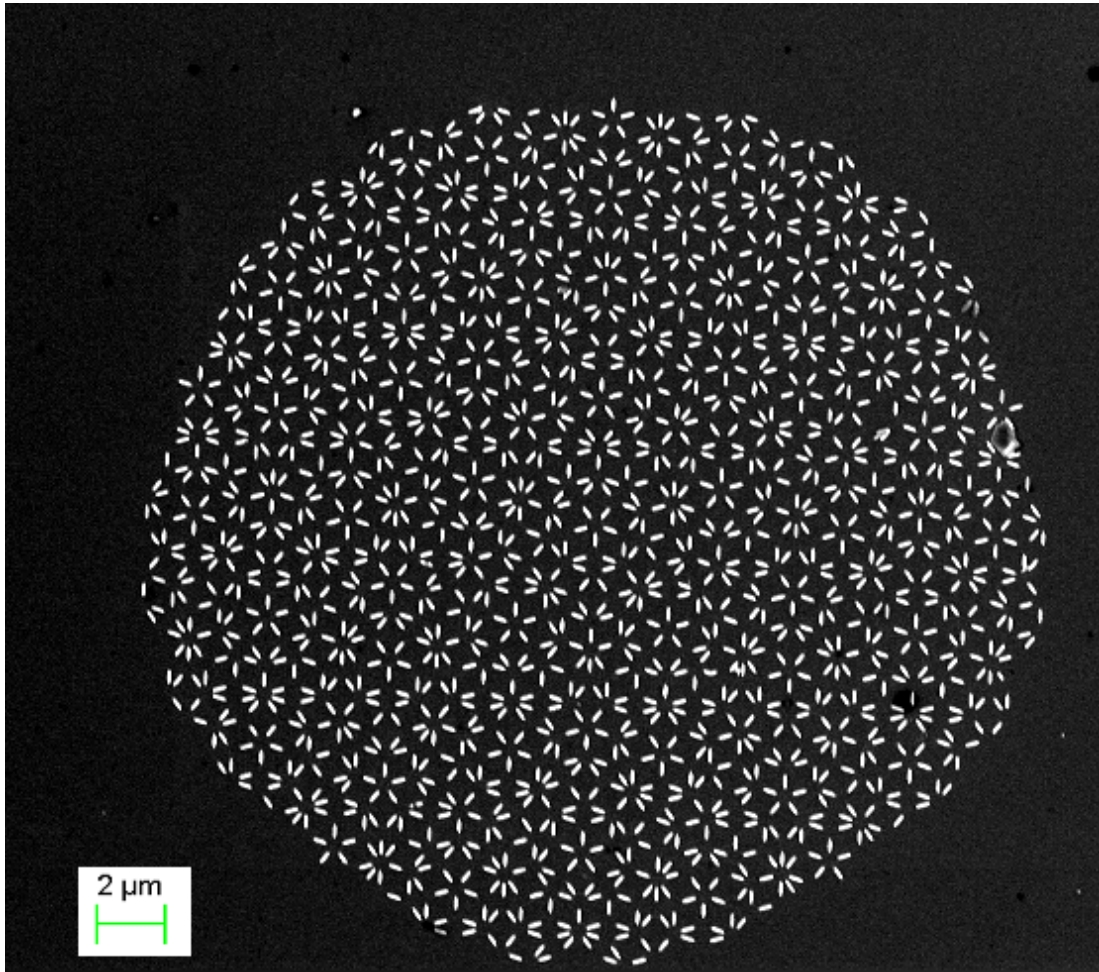


Figure C.7: The SEM image of a pattern when the sample was in the as grown state.

# References

- [1] S. Nagata, P. H. Keesom, and H. R. Harrison, “Low-dc-field susceptibility of CuMn spin glass,” *Phys. Rev. B*, vol. 19, p. 1633, 1979. [1](#)
- [2] S. Blundell, *Magnetism in Condensed Matter*. Oxford University Press, 2001. [1](#)
- [3] M. J. Harris, S. T. Bramwell, D. F. McMorrow, T. Zeiske, and K. W. Godfrey, “Geometrical frustration in the ferromagnetic pyrochlore  $\text{Ho}_2\text{Ti}_2\text{O}_7$ ,” *Phys. Rev. Lett.*, vol. 79, p. 2554, 1997. [2](#), [7](#), [8](#)
- [4] S. T. Bramwell, M. J. Harris, B. C. den Hertog, M. J. P. Gingras, J. S. Gardner, D. F. McMorrow, A. R. Wildes, A. L. Cornelius, J. D. M. Champion, R. G. Melko, and T. Fennell, “Spin correlations in  $\text{Ho}_2\text{Ti}_2\text{O}_7$ : A dipolar spin ice system,” *Phys. Rev. Lett.*, vol. 87, pp. 047205 1–4, 2001. [2](#), [8](#), [10](#), [34](#)
- [5] S. T. Bramwell and M. Harris, “Frustration in Ising-type spin models on the pyrochlore lattice,” *J. Phys.: Cond. Matt.*, vol. 10, pp. 215–220, 1998. [2](#)
- [6] C. Castelnovo, R. Moessner, and S. L. Sondhi, “Magnetic monopoles in spin ice,” *Nature*, vol. 451, p. 42, 2008. [2](#), [9](#), [10](#), [11](#)
- [7] A. Ramirez, “Strongly geometrically frustrated magnets,” *Annu. Rev. Mater. Sci.*, vol. 24, pp. 453–480, 1994. [3](#)
- [8] C. Janot, *Quasicrystals: A Primer*. Clarendon Press, 1992. [3](#)

## REFERENCES

---

- [9] E. Vedmedenko, H. P. Oepen, and J. Kirschner, “Decagonal quasiferromagnetic microstructure on the Penrose tiling,” *Phys. Rev. Lett.*, vol. 90, p. 13, 2003. [3](#), [34](#), [35](#)
- [10] T. Sato, H. Takakura, A. Tsai, and K. Shibata, “Anisotropic spin correlations in the Zn-Mg-Ho icosahedral quasicrystal,” *Phys. Rev. Lett.*, vol. 81, pp. 2364–2367, 1998. [3](#), [33](#)
- [11] T. Ishimasa, M. M., S. Matsuo, and Nakano, “Anisotropic magnetic property of single-grained  $\text{Al}_{68}\text{Pd}_{23}\text{Mn}_9$  icosahedral quasicrystals,” *Journal of the Physical Society of Japan*, vol. 62, p. 4044, 1993. [3](#)
- [12] M. Chernikov, A. Bernasconi, C. Beeli, A. Schilling, and H. Ott, “Low temperature magnetism in icosahedral  $\text{Al}_{70}\text{Mn}_9\text{Pd}_{21}$ ,” *Phys. Rev. B*, vol. 48, pp. 3058–3065, 1993. [3](#)
- [13] D. Bahadur, *Magnetic properties of Al-based icosahedral alloys*, vol. 34(1-4). Progress in Crystal Growth and Characterization of Materials, 1997. [3](#)
- [14] R. F. Wang, C. Nisoli, R. S. Freitas, J. Li, W. McConville, B. J. Cooley, M. S. Lund, N. Samarth, C. Leighton, V. H. Crespi, and P. Schiffer, “Artificial ‘spin ice’ in a geometrically frustrated lattice of nanoscale ferromagnetic islands,” *Nature*, vol. 439, pp. 303–306, 2006. [4](#), [12](#), [16](#), [21](#), [46](#)
- [15] X. Ke, J. Li, C. Nisoli, P. E. Lammert, W. McConville, R. F. Wang, V. H. Crespi, and P. Schiffer, “Energy minimization and ac demagnetization in a nanomagnet array,” *Phys. Rev. Lett.*, vol. 101, p. 037205, 2008. [4](#), [12](#), [17](#), [18](#), [19](#), [20](#), [21](#), [22](#), [47](#)
- [16] Y. Qi, T. Brintlinger, and J. Cumings, “Direct observation of the ice rule in an artificial kagome spin ice,” *Phys. Rev. B*, vol. 77, p. 094418, 2008. [4](#), [12](#), [14](#)
- [17] C. Nisoli, R. Wang, J. Li, W. F. McConville, P. E. Lammert, P. Schiffer, and V. H. Crespi, “Ground state lost but degeneracy found: the effective thermodynamics of ‘artificial spin ice’,” *Phys. Rev. Lett.*, vol. 98, p. 217103, 2007. [4](#), [12](#), [21](#), [24](#), [36](#), [95](#)

## REFERENCES

---

- [18] R. Wang, *Geometrical magnetic frustration and demagnetization of artificial spin ice*. PhD thesis, The Pennsylvania State University, The Graduate School, Department of Physics, 2007. [4](#), [13](#), [18](#)
- [19] H. Zabel, A. Schumann, A. Westphalen, and A. Remhof, “Order and frustration in artificial magnetic patterns,” *Acta Physica Polonica A*, vol. 115(1), pp. 59–62, 2009. [4](#)
- [20] W. Giaque, “Molecular rotation in ice at 10 K. Free energy of formation and entropy of water,” *Phys. Rev.*, vol. 43, p. 81, 1933. [6](#)
- [21] L. Pauling, “The structure and entropy of ice and of other crystals with some randomness of atomic arrangement,” *J. Am. Chem. Soc.*, vol. 57, p. 2680, 1935. [6](#)
- [22] J. D. Bernal and R. H. Fowler, “A theory of water and ionic solution, with particular reference to hydrogen and hydroxyl ions,” *J. Chem. Phys.*, vol. 1, p. 515, 1933. [6](#)
- [23] T. Fennell, O. A. Petrenko, B. Fak, S. T. Bramwell, M. Enjalran, T. Yavors’kii, M. J. P. Gingras, R. G. Melko, and G. Balakrishnan, “Neutron scattering investigation of the spin ice state in  $\text{Dy}_2\text{Ti}_2\text{O}_7$ ,” *Phys. Rev. B*, vol. 70, pp. 134408 1–7, 2004. [7](#)
- [24] L. Pauling, *The nature of the chemical bond*. Cornell, Ithaca., 3rd ed., 1960. [7](#)
- [25] P. W. Anderson, “Ordering and antiferromagnetism in ferrites,” *Phys. Rev.*, vol. 102, p. 4, 1956. [7](#)
- [26] H. Blote, R. Wielinga, and W. Huiskamp, “Heat-capacity measurements on rare-earth double oxides  $\text{R}_2\text{M}_2\text{O}_7$ ,” *Physica*, vol. 43, pp. 549–568, 1969. [7](#)
- [27] J. Greedan, M. Sato, and Y. Xu, “Spin-galss-like behaviour in  $\text{Y}_2\text{Mo}_2\text{O}_7$ , a concentrated, crystalline system with negligible apparent disorder,” *Solid State Communication*, vol. 59, pp. 895–897, 1986. [7](#)



## REFERENCES

---

- [28] A. P. Ramirez, A. Hayashi, R. J. Cava, R. Siddharthan, and B. S. Shastry, “Zero-point entropy in “spin ice”,” *Nature*, vol. 399, pp. 333–335, 1999. [8](#), [9](#)
- [29] R. Siddharthan, B. S. Shastry, A. Ramirez, A. Hayashi, R. J. Cava, and S. Rosenkranz, “Ising pyrochlore magnets: Low-temperature properties, ice rules, and beyond,” *Phys. Rev. Lett.*, vol. 83, pp. 1854–1857, 1999. [8](#)
- [30] S. Isakov, R. Moessner, and S. L. Sondhi, “Why spin ice obeys the ice rules,” *Phys. Rev. Lett.*, vol. 95, p. 217201, 2005. [9](#)
- [31] L. D. C. Jaubert and P. C. W. Holdsworth, “Signatures of magnetic monopole and Dirac string dynamics in spin ice,” *Nature Phys.*, vol. 5, p. 258, 2009. [10](#)
- [32] T. Fennell, P. P. Deen, A. R. Wildes, K. Schmalzl, D. Prabhakaran, A. T. Boothroyd, R. J. Aldus, D. F. McMorrow, and S. T. Bramwell, “Magnetic Coulomb phase in the spin ice  $\text{Ho}_2\text{Ti}_2\text{O}_7$ ,” *Science*, vol. 326, p. 415, 2009. [10](#)
- [33] D. J. P. Morris, D. A. Tennant, S. A. Grigera, B. Klemke, C. Castelnovo, R. Moessner, C. Czternasty, M. Meissner, K. C. Rule, J.-U. Hoffmann, K. Kiefer, S. Gerischer, D. Slobinsky, and R. S. Perry, “Dirac strings and magnetic monopoles in the spin ice  $\text{Dy}_2\text{Ti}_2\text{O}_7$ ,” *Science*, vol. 326, p. 411, 2009. [10](#)
- [34] H. Kadowaki, N. Doi, Y. Aoki, Y. Tabata, T. J. Sato, J. W. Lynn, K. Matsuhira, and Z. Hiroi, “Observation of magnetic monopoles in spin ice,” *J. Phys. Soc. Jpn.*, vol. 78, p. 103706, 2009. [10](#)
- [35] N. Rougemaille, F. Montaigne, B. Canals, A. Duluard, D. Lacour, M. Hehn, R. Belkhou, O. Fruchart, S. El Moussaoui, A. Bendounan, and F. Maccherozzi, “Artificial kagome arrays of nanomagnets: A frozen dipolar spin ice,” *Phys. Rev. Lett.*, vol. 106, p. 057209, 2011. [12](#)

- 
- [36] E. Mengotti, L. Heyderman, A. Rodríguez, A. Bisig, L. Le Guyader, F. Nolting, and H. Braun, “Building blocks of an artificial kagome spin ice: Photoemission electron microscopy of arrays of ferromagnetic islands,” *Phys. Rev. B*, vol. 78, p. 144402, 2008. [12](#), [14](#), [30](#), [36](#)
- [37] X. Ke, J. Li, S. Zhang, C. Nisoli, V. Crespi, and P. Schiffer, “Tuning magnetic frustration of nanomagnets in triangular-lattice geometry,” *Appl. Phys. Lett.*, vol. 93, p. 252504, 2008. [12](#), [13](#)
- [38] J. Li, X. Ke, S. Zhang, D. Garand, C. Nisoli, P. Lammert, V. H. Crespi, and P. Schiffer, “Comparing artificial frustrated magnets by tuning the symmetry of nanoscale permalloy arrays,” *Phys. Rev. B*, vol. 81, p. 092406, 2010. [12](#), [13](#)
- [39] C. Nisoli, J. Li, X. Ke, D. Garand, P. Schiffer, and V. H. Crespi, “Effective temperature in an interacting vertex system: Theory and experiment on artificial spin ice,” *Phys. Rev. Lett.*, vol. 105, p. 047205, 2010. [12](#), [21](#), [25](#), [77](#)
- [40] S. Ladak, D. E. Read, G. K. Perkins, L. F. Cohen, and W. R. Branford, “Direct observation of magnetic monopole defects in an artificial spin-ice system,” *Nature Phys.*, vol. 6, p. 359, 2010. [12](#)
- [41] E. Mengotti, L. J. Heyderman, A. Fraile Rodríguez, F. Nolting, R. V. Hügli, and H. B. Braun, “Real-space observation of emergent magnetic monopoles and associated Dirac strings in artificial kagome spin ice,” *Nature Phys.*, vol. 7, pp. 68–74, 2011. [12](#)
- [42] C. Phatak, M. Pan, A. Petford-Long, S. Hong, and Graef, De, “Magnetic interactions and reversal of artificial square spin ices,” *New J. Phys.*, vol. 14, p. 075028, 2012. [13](#)
- [43] M. Tanaka, E. Saitoh, H. Miyajima, T. Yamaoka, and Y. Iye, “Magnetic interactions in a ferromagnetic honeycomb nanoscale network,” *Phys. Rev. B*, vol. 73, p. 052411, 2006. [13](#)

- 
- [44] R. F. Wang, C. Nisoli, R. S. Freitas, J. Li, W. McConville, B. J. Cooley, M. S. Lund, N. Samarth, C. Leighton, V. H. Crespi, and P. Schiffer, “Demagnetization protocols for frustrated interacting nanomagnet arrays,” *J. Appl. Phys.*, vol. 101, p. 09J104, 2007. [13](#), [17](#), [18](#), [19](#)
- [45] V. S. Bhat, J. Sklenar, B. Farmer, J. Woods, J. T. Hastings, S. J. Lee, J. B. Ketterson, and Long, L. E. De, “Controlled magnetic reversal in permalloy films patterned into artificial quasicrystals,” *Phys. Rev. Lett.*, vol. 111, p. 077201, 2013. [13](#), [35](#), [36](#)
- [46] A. Libál, C. J. O. Reichhardt, and C. Reichhardt, “Creating artificial ice states using vortices in nanostructured superconductors,” *Phys. Rev. Lett.*, vol. 102, p. 237004, 2009. [13](#)
- [47] A. Libál, C. Reichhardt, and C. J. O. Reichhardt, “Realizing colloidal artificial ice on arrays of optical traps,” *Phys. Rev. Lett.*, vol. 97, p. 228302, 2006. [13](#)
- [48] U. Arnalds, A. Farhan, R. Chopdekar, V. Kapaklis, E. Balan, A. Papaioannou, M. Ahlberg, F. Nolting, L. Heyderman, and B. Hjörvarsson, “Thermalized ground state of artificial kagome spin ice building blocks,” *Appl. Phys. Lett.*, vol. 101, p. 112404, 2012. [14](#), [30](#)
- [49] A. Farhan, A. Kleibert, P. Derlet, L. Anghinolfi, A. Balan, M. Chopdekar, R.V. Wyss, S. Gliga, F. Nolting, and L. Heyderman, “Thermally induced magnetic relaxation in building blocks of artificial kagome spin ice,” *Phys. Rev. B*, vol. 89, p. 214405, 2014. [14](#), [30](#)
- [50] A. Farhan, P. Derlet, A. Kleibert, A. Balan, R. Chopdekar, M. Wyss, L. Anghinolfi, F. Nolting, and L. Heyderman, “Exploring hyper cubic energy landscapes in thermally active finite artificial spin ice systems,” *Nature Phys.*, vol. 9, p. 375, 2013. [14](#), [30](#)
- [51] V. Kapaklis, U. Arnalds, A. Clarke, E. Papaioannou, M. Karimipour, P. Korolis, A. Taroni, P. Holdsworth, S. Bramwell, and B. Hjörvarsson, “Melting artificial spin ice,” *New Journal of Physics*, vol. 14, p. 035009, 2012. [15](#), [27](#), [28](#), [36](#)

## REFERENCES

---

- [52] G.-W. Chern, P. Mellado, and O. Tchernyshyov, “Two-stage ordering of spins in dipolar spin ice on kagome,” *Phys. Rev. Lett.*, vol. 106, p. 207202, 2011. [17](#), [30](#), [51](#)
- [53] G.-W. Chern and O. Tchernyshyov, “Magnetic charge and ordering in kagome spin ice,” *Philos. Trans. A Math. Phys. Eng. Sci.*, vol. 370, pp. 5718–5737, 2012. [17](#)
- [54] L. Anghinol and et al., “Thermodynamic phase transitions in a frustrated magnetic metamaterial,” *Nat. Commun.*, vol. 6, p. 8278, 2015. [17](#), [30](#)
- [55] D. Davidović, S. Kumar, D. Reich, J. Siegel, S. Field, R. C. Tiberio, R. Hey, and K. Ploog, “Correlations and disorder in arrays of magnetically coupled superconducting rings,” *Phys. Rev. Lett.*, vol. 76, pp. 815–818, 1996. [17](#)
- [56] D. Davidović, S. Kumar, D. H. Reich, J. Siegel, S. B. Field, R. C. Tiberio, R. Hey, and K. Ploog, “Magnetic correlations, geometrical frustration, and tunable disorder in arrays of superconducting rings,” *Phys. Rev. B*, vol. 55, pp. 6518–6540, Mar 1997. [17](#)
- [57] J. R. Kirtley, C. C. Tsuei, Ariando, H. J. H. Smilde, and H. Hilgenkamp, “Antiferromagnetic ordering in arrays of superconducting  $\pi$ -rings,” *Phys. Rev. B*, vol. 72, p. 214521, Dec 2005. [17](#)
- [58] Y. Han, Y. Shokef, A. Alsayed, P. Yunker, T. Lubensky, and A. Yodh, “Geometrical frustration in buckled colloidal monolayers,” *Nature*, vol. 456, pp. 898–903, 2008. [17](#)
- [59] Y. Shokef and T. C. Lubensky, “Stripes, zigzags, and slow dynamics in buckled hard spheres,” *Phys. Rev. Lett.*, vol. 102, p. 048303, Jan 2009. [17](#)
- [60] R. Cowburn, “Probing antiferromagnetic coupling between nanomagnets,” *Phys. Rev. B*, vol. 65, p. 092409, 2002. [17](#)
- [61] A. Imre, G. Csaba, G. Bernstein, W. Porod, and V. Metlushko, “Investigation of shape-dependent switching of coupled nanomagnets,” *Superlattices and Microstructures*, vol. 34, pp. 513–518, 2003. [17](#)

## REFERENCES

---

- [62] J. P. Morgan, A. Bellew, A. Stein, S. Langridge, and C. H. Marrows, “Linear field demagnetization of artificial magnetic square ice,” *Frontiers in Physics*, vol. 1, p. 28, 2013. [18](#), [48](#)
- [63] G. D’Anna, P. Mayor, A. Barrat, V. Loreto, and F. Nori, “Observing brownian motion in vibration-fluidized granular matter,” *Nature*, vol. 424, pp. 909–912, 2003. [21](#)
- [64] A. Mehta and S. Edwards, “Statistical mechanics of powder mixtures,” *Physica A*, vol. 157, pp. 1091–1100, 1989. [21](#)
- [65] J. Morgan, A. Stein, S. Langridge, and C. H. Marrows, “Thermal ground state ordering and elementary excitations in artificial magnetic square ice,” *Nature Phys.*, vol. 7, pp. 75–79, 2011. [26](#), [27](#), [29](#), [78](#), [83](#), [95](#)
- [66] Z. Budrikis, K. L. Livesey, J. P. Morgan, J. Akerman, A. Stein, S. Langridge, C. H. Marrows, and R. L. Stamps, “Domain dynamics and fluctuations in artificial square ice at finite temperatures,” *New Journal of Physics*, vol. 14, p. 035014, 2012. [26](#)
- [67] S. Greaves and H. Muraoka, “Formation of thermally induced ground states in two-dimensional square spin ices,” *Appl. Phys. Lett.*, vol. 112, p. 043909, 2012. [26](#)
- [68] M. Parnaste, M. Marcellini, E. Holmstrom, N. Bock, J. Fransson, O. Eriksson, and B. Hjörvarsson, “Dimensionality crossover in the induced magnetization of Pd layers,” *Journal of Physics: Condensed Matter*, vol. 19, p. 246213, 2007. [27](#)
- [69] S. Zhang, I. Gilbert, C. Nisoli, G. Chern, M. Erickson, L. O’Brien, C. Leighton, P. Lammert, V. Crespi, and P. Schiffer, “Crystallites of magnetic charges in artificial spin ice,” *Nature*, vol. 500, pp. 553–557, 2013. [29](#), [36](#), [46](#), [48](#), [50](#), [68](#), [71](#), [72](#), [83](#), [88](#), [95](#)
- [70] R. Penrose, *Pentaplexity: A class of nonperiodic tilings of the plane*, vol. 2. The Mathematical Intelligencer, 1979. [32](#), [33](#)

- 
- [71] S. Marjorie, *Quasicrystals and geometry*. Cambridge University Press, 1996. [32](#)
- [72] N. Bruijn, “Algebraic theory of Penrose’s non-periodic tilings of the plane,” *Nederl. Akad. Wetensch. Proc. Ser. A*, vol. 84, pp. 38–52, 1981. [33](#), [97](#)
- [73] N. Bruijn, “Algebraic theory of Penrose’s non-periodic tilings of the plane,” *Indag. Math.*, vol. 43, pp. 53–66, 1981. [33](#)
- [74] J. Socolar and P. Steinhardt, “Quasicrystals. ii. unit-cell configurations,” *Phys. Rev. B*, vol. 34, pp. 617–647, 1986. [33](#)
- [75] T. Sato, H. Takakura, A. Tsai, K. Shibata, K. Ohoyama, and K. Andersen, “Antiferromagnetic spin correlations in the Zn-Mg-Ho icosahedral quasicrystal,” *Phys. Rev. B*, vol. 61, pp. 476–486, 2000. [33](#), [34](#)
- [76] T. Sato, H. Takakura, A. Tsai, and K. Shibata, “Magnetic excitations in the Zn-Mg-Tb icosahedral quasicrystal: An inelastic neutron scattering study,” *Phys. Rev. B (Condensed Matter and Materials Physics)*, vol. 73, p. 054417, 2006. [33](#)
- [77] Y. Hattori, A. Niikura, A. and Tsai, A. Inoue, T. Masumoto, K. Fukamichi, H. Aruga-Katori, and T. Goto, “Spin-glass behaviour of icosahedral Mg-Gd-Zn and Mg-Tb-Zn quasi-crystals,” *Journal of Physics: Condensed Matter*, vol. 7, pp. 2313–2320, 1995. [33](#)
- [78] D. Schmitt and B. Charrier, “Magnetic properties of  $R_8Mg_{42}Zn_{50}$  quasicrystals ( $R = Tb, Dy, Ho, Er$ ).,” *Journal of Magnetism and Magnetic Materials*, vol. 171, pp. 106–112, 1997. [33](#)
- [79] D. Charrier, B. and Schmitt, “Dynamical and irreversible magnetic effects in  $Ir_8Mg_{42}Zn_{50}$  quasicrystals ( $R=Tb, Dy$ ).,” *Journal of Magnetism and Magnetic Materials*, vol. 189, pp. 165–172, 1998. [33](#)
- [80] D. Noakes, G. Kalvius, R. Wappling, C. Stronach, M. White, H. Saito, and K. Fukamichi, “Spin dynamics and freezing in magnetic rare-earth quasicrystals,” *Physics Letters A*, vol. 238, pp. 197–202, 1998. [33](#)

## REFERENCES

---

- [81] A. Yamamoto, S. Weber, A. Sato, K. Kato, K. Tsai, A. Niikura, K. Hiraga, A. Inoue, and T. Masumoto, “Electron density of icosahedral Zn-Mg-Y quasicrystals determined by a six-dimensional maximum entropy method.,” *Philosophical Magazine Letters*, vol. 73, pp. 247–254, 1996. [33](#)
- [82] B. Charrier, B. Ouladdiaf, and D. Schmitt, “Observation of quasimagnetic structures in rare-earth-based icosahedral quasicrystals.,” *Phys. Rev. Lett.*, vol. 78, pp. 4637–4640, 1997. [33](#)
- [83] Z. Islam, I. R. Fisher, J. Zarestky, P. C. Canfield, C. Stassis, and A. I. Goldman, “Reinvestigation of long-range magnetic ordering in icosahedral Tb-Mg-Zn.,” *Phys. Rev. B*, vol. 57, pp. R11047–R11050, 1998. [34](#)
- [84] T. Sato, H. Takakura, A. Tsai, and K. Shibata, “Observation of quasimagnetic structures in rare-earth-based icosahedral quasicrystals.,” *Phys. Rev. Lett.*, vol. 81, pp. 2364–2367, 1998. [34](#)
- [85] H. Takakura, T. Sato, and A. Tsai, “Single crystal growth of the icosahedral Zn-Mg-Ho quasicrystal.,” *Jpn. J. Appl. Phys.*, vol. 37, p. 1663, 1998. [34](#)
- [86] T. Fujiwara, “Electronic structure in the Al-Mn alloy crystalline analog of quasicrystals,” *Phys. Rev. B*, vol. 40, pp. 942–946, 1989. [34](#)
- [87] T. Fujiwara and T. Yokokawa, “Universal pseudogap at Fermi energy in quasicrystals,” *Phys. Rev. Lett.*, vol. 666, pp. 333–336, 1991. [34](#)
- [88] R. V. Moody, *The Mathematics of Long-Range Aperiodic Order*. Springer Netherlands, 1997. [34](#)
- [89] I. Haller, M. Hatzakis, and R. Srinivasan, “High-resolution positive resists for electron-beam exposure,” *IBM J. Res. Dev.*, vol. 12, p. 251, 1968. [37](#)
- [90] M. Hatzakis, “Electron resists for microcircuit and mask production,” *J. Electrochem Soc.: Electrochemical Technology*, vol. 116, p. 1033, 1969. [37](#)
- [91] H. Y. Ku and L. C. Scala, “Polymeric electron beam resists,” *J. Electrochem. Soc.: Solid State Science*, vol. 116, p. 980, 1969. [37](#)

## REFERENCES

---

- [92] G. Binnig, C. F. Quate, and C. Gerber, “Atomic force microscope,” *Phys. Rev. Lett.*, vol. 56, pp. 930–933, 1986. 38, 40
- [93] R. Gomez, *Magnetic Imaging and its applications to materials*. Experimental Methods in the Physical Sciences, Academic Press, 2001. 40
- [94] A. San Paulo and R. Gracia, “Unifying theory of tapping-mode atomic-force microscopy,” *Phys. Rev. B*, vol. 66, p. 041406(R), 2002. 40
- [95] T. Albrecht, P. Grütter, D. Horne, and D. Rugar, “Frequency modulation detection using high- $Q$  cantilevers for enhanced force microscopy sensitivity,” *J. Appl. Phys.*, vol. 69, pp. 668–673, 1991. 40
- [96] D. Sarid, *Scanning Force Microscopy With Applications to Electric, Magnetic and Atomic Forces*. Oxford Series in Optical and Imaging Sciences, Oxford University Press, 1991. 41
- [97] P. Grütter, E. Meyer, H. Heinzelmann, L. Rosenthaler, H.-R. Hidber, and H.-J. Güntherodt, “Application of atomic force microscopy to magnetic materials,” *J. Vac. Sci. Technol. A*, vol. 6, pp. 279–282, 1988. 41
- [98] J. Mamin, D. Rugar, J. Stern, R. Fontana, Jr., and P. Kasiraj, “Magnetic force microscopy of thin permalloy films,” *Appl. Phys. Lett.*, vol. 55, pp. 318–320, 1989. 41, 42
- [99] T. Göddenhenrich, U. Hartmann, and C. Heidon, “Generation and imaging of domains with the magnetic force microscope,” *Ultramicroscopy*, vol. 42–44, pp. 256–261, 1992. 42
- [100] “The object oriented micromagnetic framework (oommf) project at ITL/NIST.” <http://math.nist.gov/oommf/>, 2005. 44, 45
- [101] I. Gilbert, C. Nisoli, G. W. Chern, S. Zhang, L. O’Brien, B. Fore, and P. Schiffer, “Emergent ice rule and magnetic charge screening from vertex frustration in artificial spin ice,” *Nature Phys.*, vol. 10, pp. 670–675, 2014. 57



## REFERENCES

---

- [102] J. Porro, A. Pinto, A. Berger, and P. Vavassori, “Exploring thermally induced states in square artificial spin-ice arrays,” *New J. Phys.*, vol. 15, p. 055012, 2013. [80](#), [90](#), [92](#)
- [103] J. A. Osborn, “Demagnetizing factors of the general ellipsoid,” *Phys. Rev.*, vol. 67, 1945. [87](#)
- [104] P. Kramer and R. Neri, “On periodic and non-periodic space fillings of  $e^m$  obtained by projection,” *Acta Cryst. A*, vol. 40, pp. 580–587, 1984. [97](#)
- [105] M. Duneau and A. Katz, “Quasiperiodic patterns,” *Phys. Rev. Lett.*, vol. 54, p. 25, 1985. [97](#)
- [106] V. Elser, “The diffraction pattern of projected structures,” *Acta Cryst. A*, vol. 42, pp. 36–43, 1986. [97](#)
- [107] K. N. Ishihara, “Penrose pattern and related structures,” *Acta Cryst. A*, vol. 44, pp. 508–516, 1988. [97](#)
- [108] A. Szallas, *Heisenberg Antiferromagnetic model on 2D quasiperiodic tilings*. PhD thesis, Orsay, Laboratoire de Physique des Solides, 2008. [98](#)
- [109] E. J. W. Whittaker and R. M. Whittaker, “Some generalized penrose patterns from projections of n-dimensional lattices,” *Acta Cryst. A*, vol. 44, pp. 105–112, 1988. [101](#)